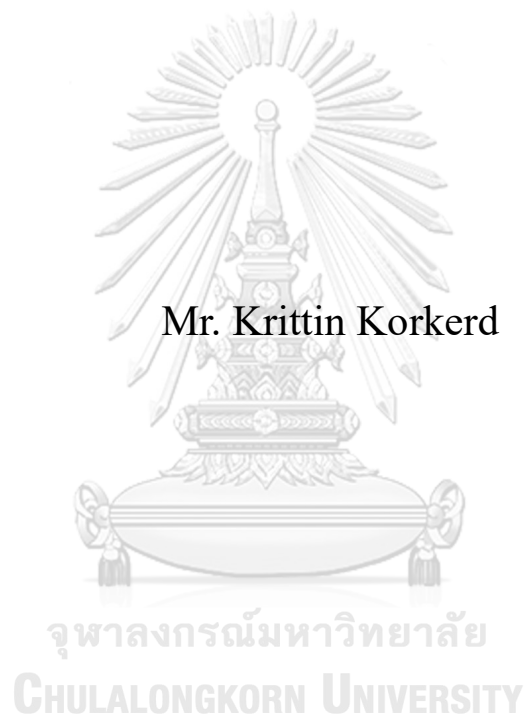


IMPROVEMENT OF HYDRODYNAMICS AND HEAT
TRANSFER IN BIOMASS FLUIDIZED BED COMBUSTOR
WITH IMMERSED TUBES USING CFD-DEM



A Dissertation Submitted in Partial Fulfillment of the Requirements
for the Degree of Doctor of Philosophy in Chemical Technology
Department of Chemical Technology
FACULTY OF SCIENCE
Chulalongkorn University
Academic Year 2022
Copyright of Chulalongkorn University

การปรับปรุงอุทกพลศาสตร์และการถ่ายโอนความร้อนในเตาเผาชีวมวลแบบฟลูอิดไคซ์เบดที่มีท่อ
จมด้วย CFD-DEM



วิทยานิพนธ์นี้เป็นส่วนหนึ่งของการศึกษาตามหลักสูตรปริญญาวิทยาศาสตรดุษฎีบัณฑิต
สาขาวิชาเคมีเทคนิค ภาควิชาเคมีเทคนิค
คณะวิทยาศาสตร์ จุฬาลงกรณ์มหาวิทยาลัย
ปีการศึกษา 2565
ลิขสิทธิ์ของจุฬาลงกรณ์มหาวิทยาลัย

Thesis Title	IMPROVEMENT OF HYDRODYNAMICS AND HEAT TRANSFER IN BIOMASS FLUIDIZED BED COMBUSTOR WITH IMMERSED TUBES USING CFD-DEM
By	Mr. Krittin Korkerd
Field of Study	Chemical Technology
Thesis Advisor	Associate Professor BENJAPON CHALERMSINSUWAN, Ph.D.
Thesis Co Advisor	Professor PORNPOTE PIUMSOMBOON, Ph.D. Zongyan Zhou, Ph.D.

Accepted by the FACULTY OF SCIENCE, Chulalongkorn University in
Partial Fulfillment of the Requirement for the Doctor of Philosophy

..... Dean of the FACULTY OF
SCIENCE
(Professor POLKIT SANGVANICH, Ph.D.)

DISSERTATION COMMITTEE

..... Chairman
(Boonrod Sajjakulnukit, Ph.D.)

..... Thesis Advisor
(Associate Professor BENJAPON
CHALERMSINSUWAN, Ph.D.)

..... Thesis Co-Advisor
(Professor PORNPOTE PIUMSOMBOON, Ph.D.)

..... Thesis Co-Advisor
(Zongyan Zhou, Ph.D.)

..... Examiner
(Professor THARAPONG VITIDSANT, Ph.D.)

..... Examiner
(Professor SUTTICHA ASSABUMRUNGRAT, Ph.D.)

..... Examiner
(Associate Professor PRAPAN KUCHONTHARA,
Ph.D.)

กฤติน ก่อเกิด : การปรับปรุงอุทกพลศาสตร์และการถ่ายโอนความร้อนในเตาเผาชีวมวลแบบฟลูอิดไรซ์เบดที่มีท่อจมด้วย CFD-DEM. (IMPROVEMENT OF HYDRODYNAMICS AND HEAT TRANSFER IN BIOMASS FLUIDIZED BED COMBUSTOR WITH IMMERSSED TUBES USING CFD-DEM) อ.ที่ปรึกษาหลัก : รศ. ดร.เบญจพล เฉลิมสินสุวรรณ, อ.ที่ปรึกษาร่วม : ศ.พรพจน์ เปี่ยมสมบูรณ์,ดร.จงเหียน โจว

พลศาสตร์ของไหลเชิงคำนวณควบคู่ไปกับวิธีการคำนวณอนุภาคแบบไม่ต่อเนื่อง (CFD-DEM) นิยมใช้ในการศึกษาอุทกพลศาสตร์และการถ่ายโอนความร้อนในกระบวนการฟลูอิดไรซ์ชัน การศึกษานี้มุ่งเน้นไปที่การปรับปรุงอุทกพลศาสตร์และการถ่ายโอนความร้อนในเตาเผาชีวมวลฟลูอิดไรซ์เบดที่มีท่อจม ในการศึกษาได้มีการใช้ชีวมวลผสมเพื่อศึกษาผลของประเภทของชีวมวล ปริมาณที่ใช้และสัดส่วนผสมของชีวมวล เพื่อเสนอหลักเกณฑ์การเลือกใช้เชื้อเพลิงชีวมวลที่เหมาะสมสำหรับระบบ พารามิเตอร์การออกแบบที่เกี่ยวข้องกับท่อจม ประกอบด้วย มุมระหว่างท่อ เส้นผ่านศูนย์กลางท่อ และระยะห่างระหว่างท่อ ได้ถูกนำมาพิจารณา แบบจำลองที่ขับเคลื่อนด้วยข้อมูลได้พัฒนาขึ้นจากผลการจำลองจากแบบจำลอง CFD-DEM เพื่อทำนายพารามิเตอร์ของระบบ แบบจำลองนี้มีศักยภาพในการนำไปประยุกต์ใช้ในการดำเนินการเชิงวิศวกรรมในระหว่างการดำเนินการจริงโดยไม่ต้องใช้การจำลองด้วย CFD-DEM

แบบจำลอง CFD-DEM ได้ถูกพัฒนาขึ้นสำหรับการใช้งานชีวมวลที่มีรูปทรงระบอบอก และอนุภาคทรายที่มีรูปทรงกลม ด้วยการใช้แบบจำลองแรงดันที่เหมาะสม ผลการวิจัยพบว่า การใช้ชีวมวลผสมระหว่างไม้ซิป และเชื้อไม้ที่มีอัตราส่วนการผสมของไม้ซิปต่อเชื้อไม้ 1 ต่อ 3 มีสัดส่วนชีวมวลร้อยละ 5 และ ใช้สัดส่วนระหว่างขนาดเส้นผ่านศูนย์กลางเทียบเท่าเฉลี่ยของชีวมวลต่อขนาดเส้นผ่านศูนย์กลางเทียบเท่าของทรายเท่ากับ 4.44 ให้ผลทางอุทกพลศาสตร์ที่ดีที่สุดในการศึกษานี้ โดยมีหลักเกณฑ์การเลือกใช้ชีวมวล คือ เลือกใช้ชีวมวลรูปทรงระบอบอก ที่มีขนาดเส้นผ่านศูนย์กลางเทียบเท่ามากกว่าทราย อีกทั้งควรใช้สัดส่วนไม้ซิปน้อยกว่าเชื้อไม้ นอกจากนี้ จากการวิเคราะห์การออกแบบแฟกทอเรียล 2^k พบว่า มุมระหว่างท่อ และเส้นผ่านศูนย์กลางท่อเป็นตัวแปรที่มีอิทธิพลมากที่สุดในพฤติกรรมภายในระบบ อีกทั้งการพัฒนาแบบจำลองโครงข่ายประสาทเทียม (ANN) โดยใช้ชุดข้อมูลจากการจำลองสามารถทำนายดัชนีการผสม สัดส่วนเชิงปริมาตรของแข็งและอุณหภูมิของแข็งภายในระบบได้อย่างแม่นยำ การศึกษานี้ช่วยเพิ่มความเข้าใจเกี่ยวกับอุทกพลศาสตร์และการถ่ายโอนความร้อนภายในระบบและให้ข้อมูลสำหรับการเพิ่มประสิทธิภาพการออกแบบและการดำเนินการกระบวนการที่เกี่ยวข้องกับการใช้งานชีวมวลผสมและทราย

จุฬาลงกรณ์มหาวิทยาลัย
CHULALONGKORN UNIVERSITY

สาขาวิชา เคมีเทคนิค
ปีการศึกษา 2565

ลายมือชื่อนิสิต
ลายมือชื่อ อ.ที่ปรึกษาหลัก
ลายมือชื่อ อ.ที่ปรึกษาร่วม
ลายมือชื่อ อ.ที่ปรึกษาร่วม

6371014523 : MAJOR CHEMICAL TECHNOLOGY

KEYWORD: Biomass Fluidized Bed Combustor, CFD-DEM, Immersed Tubes

Krittin Korkerd : IMPROVEMENT OF HYDRODYNAMICS AND HEAT TRANSFER IN BIOMASS FLUIDIZED BED COMBUSTOR WITH IMMERSSED TUBES USING CFD-DEM. Advisor: Assoc. Prof. BENJAPON CHALERMSINSUWAN, Ph.D. Co-advisor: Prof. PORNPOTE PIUMSOMBOON, Ph.D., Zongyan Zhou, Ph.D.

Computational Fluid Dynamics coupled with Discrete Element Method (CFD-DEM) has been extensively utilized for studying hydrodynamics and heat transfer in fluidization processes. This study specifically focuses on improving hydrodynamics and heat transfer in a biomass fluidized bed combustor with immersed tubes. The investigation involves the use of mixed biomass, exploring the effects of biomass types, biomass loading, and blending ratios to propose criteria for selecting suitable biomass fuel for the system. Design parameters related to the immersed tubes, such as the angle between tubes, tube diameters, and distance between tubes, were also considered. A data-driven model was developed based on the CFD-DEM results to predict system parameters. This model offers potential applications in real-time practical engineering without the need for CFD-DEM simulation.

The CFD-DEM model was developed for cylindrical biomass and spherical silica sand particles, incorporating an appropriate drag force model. The results showed that the use of mixed biomass with a blending ratio of 1:3 of wood chips to coarse bagasse, with a 5% biomass loading using a ratio of the average equivalent diameter of the biomasses to the equivalent diameter of silica sand of 4.44, was identified as suitable conditions in a general case to obtain the most efficient hydrodynamic results in this study. The criteria for selecting biomass are cylindrical biomass with a greater equivalent diameter than silica sand. Additionally, the proportion of wood chips should be less than that of bagasse. Furthermore, through a 2^k factorial design analysis, it was determined that the angle between tubes and tube diameter had the most significant influence on the system behaviors. Moreover, the development of Artificial Neural Network (ANN) models was successful using the simulation dataset, enabling accurate predictions of the mixing index, solid volume fraction, and solid temperature within the system. This study enhances the understanding of hydrodynamics and heat transfer within systems and provides valuable insights for optimizing the design and operation of applications involving mixed biomass and silica sand.

Field of Study: Chemical Technology
Academic Year: 2022

Student's Signature
Advisor's Signature
Co-advisor's Signature
Co-advisor's Signature

ACKNOWLEDGEMENTS

I would like to express my sincere gratitude and appreciation to all those who have contributed to the completion of this research project.

First and foremost, I am deeply thankful to my supervisor, Associate Professor Dr. Benjapon Chalermsoonsuwan, who has been with me from the beginning of my journey. I am grateful for the invaluable opportunity, guidance, and continuous support he has provided throughout this research endeavor, helping me fulfill my dream.

I am also thankful to Professor Dr. Pornpote Piumsomboon and Dr. Zongyan Zhou, my co-advisors, for their insightful feedback and constructive suggestions. Their contributions have been instrumental in shaping the quality of this research.

I would like to extend my deepest gratitude to Associate Professor Dr. Ruiping Zou, Professor Dr. Aibing Yu, and the research team "SIMPAS" at Monash University. The unforgettable experiences with them made me feel at home during my first overseas life. SIMPAS will forever hold a special place in my heart as my Australian home.

Heartfelt thanks go to my friends and colleagues in the Cybernetics Lab for their generous contributions of time and assistance. Specifically, I want to mention Dr. Chaiwat Soanuch for his invaluable help in everything and for our enduring friendship.

I would like to acknowledge the scholarships provided by the Second Century Fund (C2F) for the Funding for High-Efficiency Ph.D. Candidates and the Conducting Research Abroad scholarship.

I express my thanks to the Department of Chemical Technology, Faculty of Science, Chulalongkorn University, for giving me the opportunity to undertake this Ph.D. course. I am also grateful to the Department of Chemical and Biological Engineering, Faculty of Engineering, Monash University, for providing the services and resources.

I would also like to express my deepest gratitude to my family for their unwavering support and encouragement throughout this journey. Their love and understanding have been a constant source of motivation for me.

Lastly, I want to thank myself for the efforts, perseverance, and refusal to give up on anything in pursuit of my dreams and the creation of my own legacy for the world to know.

Krittin Korkerd

TABLE OF CONTENTS

	Page
ABSTRACT (THAI)	iii
ABSTRACT (ENGLISH).....	iv
ACKNOWLEDGEMENTS.....	v
TABLE OF CONTENTS	vi
LIST OF TABLES	ix
LIST OF FIGURES	x
CHAPTER 1 INTRODUCTION.....	1
1.1. Background.....	1
1.2. Objectives	5
1.3. Scope of dissertation.....	5
1.4. Structure of dissertation.....	6
CHAPTER 2 THEORY AND LITERATURE REVIEWS.....	7
2.1. Biomass.....	7
2.1.1. Biomass as a source of renewable energy	7
2.1.2. Biomass characteristics and properties.....	8
2.1.3. Categories of Biomass.....	10
2.1.4. Energy generation from biomass.....	12
2.1.4.1. Direct combustion	12
2.1.4.2. Thermochemical conversion	14
2.1.5. The drawbacks of biomass for energy production	15
2.2. Fluidization.....	16
2.2.1 Flow regime in fluidization	17
2.2.2. Biomass fluidized bed combustion.....	19
2.2.3. Effect of immersed surfaces in fluidized bed	21
2.3. Computational fluid dynamics-Discrete element method approach.....	23

2.3.1. Computational fluid dynamics	23
2.3.2. Discrete element method	24
2.3.3. CFD-DEM coupling	31
2.4. Artificial neural network	34
2.5. Literature review	38
CHAPTER 3 CFD-DEM MODELING OF BINARY MIXTURES OF BIOMASS AND SILICA SAND IN A BUBBLING FLUIDIZED BED	46
3.1. Geometry, initial and boundary conditions	47
3.2. Numerical model	48
3.3. Results and discussions	51
3.3.1. Model validation	51
3.3.2. Time independency test	53
3.3.3. Mixing in binary particle systems	54
3.4. Conclusion	56
CHAPTER 4 NUMERICAL SIMULATION OF MIXED BIOMASS AND SILICA SAND PARTICLES IN A BUBBLING FLUIDIZED BED COMBUSTOR 58	
4.1. Geometry, initial and boundary conditions	59
4.2. Numerical model	68
4.3. Results and discussions	69
4.3.1. Flow pattern and mixing characteristics of single biomass mixture	69
4.3.2. Flow pattern and mixing characteristics of mixed biomass mixture	76
4.3.3. Effect of silica sand size	81
4.3.4. Heat transfer behavior	87
4.3.5. Force analysis	90
4.3.6. Limitations related to actual operation	93
4.4. Conclusion	94
CHAPTER 5 EFFECT OF DESIGN PARAMETERS ON THE HYDRODYNAMICS AND HEAT TRANSFER IN A BUBBLING FLUIDIZED BED COMBUSTOR WITH IMMERSERD TUBES	97

5.1. Statistical Design of Experiment	98
5.2. Geometry, initial and boundary conditions.....	100
5.3. Numerical model	102
5.4. Results and discussions.....	102
5.4.1. Parameter study	102
5.4.2. Effect of angle between tubes.....	119
5.4.3. Effect of tube diameter	124
5.4.4. Effect of distance between tubes	128
5.4.5. Heat transfer coefficient analysis	131
5.4.6. Advantages and limitations related to actual operation.....	133
5.5. Conclusion	136
CHAPTER 6 DATA-DRIVEN MODEL FOR PREDICTING MIXING BEHAVIOR AND TEMPERATURE IN A BUBBLING FLUIDIZED BED COMBUSTOR WITH IMMERSED TUBES.....	139
6.1. Dataset buildup from CFD-DEM simulations for model development.....	141
6.2. Response Surface Methodology model	143
6.3. Artificial Neural Network model	144
6.4. Results and discussions.....	146
6.4.1. RSM model performance	146
6.4.2. ANN model performance	149
6.4.3. Prediction of Mixing Index	154
6.4.4. Prediction of solid volume fraction.....	156
6.4.5. Prediction of solid temperature	158
6.5. Conclusion	160
CHAPTER 7 CONCLUSION	161
APPENDIX.....	166
REFERENCES	168
VITA	186

LIST OF TABLES

	Page
Table 3.1 Designed experiments.	50
Table 3.2 Parameter properties used in the model.	50
Table 3.3 Factor effect estimates for response: Average mixing index.....	56
Table 4.1 Physical properties and operational parameters employed in this study.....	65
Table 4.2 Simulation conditions of each study case.	67
Table 4.3 Component of bagasse sizes in each type.	67
Table 5.1 2 ^k Factorial experimental design for designing parameters of bubbling fluidized bed combustor with immersed tubes.	100
Table 5.2 Results for the responses of fluidized bed with immersed tubes simulation.	103
Table 5.3 ANOVA results for the responses.....	103
Table 6.1 Input and output variables of neural networks.....	142
Table 6.2 Deviation prediction results for each response using RSM models.....	148
Table 6.3 Obtained results of neural networks prediction.	154
Table A.1 The weight and bias coefficients of the optimum neural network model for mixing index prediction.	166
Table A.2 The weight and bias coefficients of the optimum neural network model for solid volume fraction prediction.	166
Table A.3 The weight and bias coefficients of the optimum neural network model for solid temperature prediction.	167

LIST OF FIGURES

	Page
Figure 2.1 Flow regime of gas-solid fluidization [76].	43
Figure 2.2 Analysis of contact forces during the collision of discrete particles considering the overlapping between particles [50].	43
Figure 2.3 Normal force–overlap response for the hysteretic linear spring model [52].	44
Figure 2.4 Conductive heat transfer between two colliding particles [52].	44
Figure 2.5 Flow chart of the CFD-DEM coupling approach.	45
Figure 3.1 Schematic geometry of the fluidized bed.	49
Figure 3.2 Initial packed bed with biomass and silica sand particles.	49
Figure 3.3 Comparison of the pressure drop between the experimental [67] and simulation results.	52
Figure 3.4 Comparison of the flow behavior between the experimental [67] and simulation results.	52
Figure 3.5 Mixing index with time (Case 4).	53
Figure 3.6 The average mixing index with different particle sizes and loadings.	55
Figure 4.1 Dimensions of the fluidized bed combustor used in this study.	63
Figure 4.2 Computational grid for the fluidized bed combustor.	64
Figure 4.3 Initial packed bed of mixed biomass and silica sand (Case 9).	64
Figure 4.4 Flow patterns for the mixture of silica sand and (a) wood chip, (b) coarse bagasse, (c) fine bagasse and (d) all bagasse.	72
Figure 4.5 Time-averaged solid volume fraction of particles along the bed height for the mixture of silica sand and (a) wood chip, (b) coarse bagasse, (c) fine bagasse and (d) and all bagasse.	75
Figure 4.6 (a) Mixing index with time and (b) comparison of the time-averaged mixing indexes with the change of biomass loading for different mixtures.	75
Figure 4.7 Flow patterns for the mixture of silica sand and mixed biomass with 5% loading and different blending ratios between wood chip and coarse bagasse of (a) 1:1, (b) 3:1, (c) 1:3 and (d) 1:3 using silica sand size of 1 mm.	77

Figure 4.8 Time-averaged solid volume fraction of particles along the bed height for the mixed biomass with 5% loading in the different blending ratios between wood chip and coarse bagasse of (a) 1:1, (b) 3:1 and (c) 1:3.	80
Figure 4.9 (a) Mixing index changes with time and (b) comparison of the time-averaged mixing indexes with the variation of biomass loading for different blending ratios of mixed biomass.	80
Figure 4.10 Comparison of time-averaged solid volume fraction of particles along the bed height for the mixed biomass (WC1:BG3) with 5% loading and different silica sand sizes.	84
Figure 4.11 Time-averaged solid volume fraction in the horizontal direction at different heights of 0.07 and 0.1 m for the mixed biomass (WC1:BG3) with 5% loading and different silica sand sizes.	85
Figure 4.12 Comparison of mixing index variation with time for the mixture of (a) wood chip, (b) coarse bagasse, (c) mixed biomass (WC1:BG3) with 5% loading and silica sand with different sizes and (d) comparison of the time-averaged mixing indexes with the different mixtures and silica sand sizes.	86
Figure 4.13 The evolution of the average particle temperature, (c), (d) probability distribution of particle temperature, and (e), (f) the evolution of the average convective heat transfer rate for different particles in case of mixed biomass (WC1:BG3) with 5% loading and different silica sand sizes.	89
Figure 4.14 Probability distribution of (a), (b) normalized normal contact forces (c), (d) normalized drag forces and (e), (f) normalized pressure gradient forces on individual particles in case of mixed biomass (WC1:BG3) with 5% loading and different silica sand sizes.	92
Figure 5.1 Schematic drawing of the bubbling fluidized bed combustor with a (a) in-line and (b) staggered immersed tubes configurations.	101
Figure 5.2 Results of the response of average mixing index for each experimental design case.	106
Figure 5.3 Results of the response of average solid volume fraction at different heights for each experimental design case.	108

Figure 5.4 Results of the response of average solid temperature at different heights for each experimental design case.	109
Figure 5.5 Main effect plot of the average mixing index.	110
Figure 5.6 Main effect plot of the average solid volume fraction at the height of 0.065 m.	112
Figure 5.7 Main effect plot of the average solid volume fraction at the height of 0.1 m.	113
Figure 5.8 Main effect plot of the average solid volume fraction at the height of 0.14 m.	114
Figure 5.9 Main effect plot of the average solid temperature at the height of 0.065 m.	115
Figure 5.10 Main effect plot of the average solid temperature at the height of 0.1 m.	116
Figure 5.11 Main effect plot of the average solid temperature at the height of 0.14 m.	118
Figure 5.12 Qualitative comparison of the flow patterns in the system with different tube configurations, including (a) no-tube, (b) in-line, and (c) staggered.	121
Figure 5.13 Profile comparison of the time-averaged solid volume fraction in the systems with different tube configurations.	123
Figure 5.14 Time evolutionary profiles of the mixing index in the systems with different tube configurations.	123
Figure 5.15 Contour plot of solid temperature at different times in the system with different tube configurations, including (a) no-tube, (b) in-line, and (c) staggered. .	124
Figure 5.16 Profile comparison of the time-averaged solid volume fraction in the systems with different tube diameters.	126
Figure 5.17 Time evolutionary profiles of the mixing index in the systems with different tube diameters.	127
Figure 5.18 Contour plot of solid temperature at different times in the system with different tube diameters of (a) 10.3 and (b) 17.1 mm.	127
Figure 5.19 Profile comparison of the time-averaged solid volume fraction in the systems with different distance between tubes.	129
Figure 5.20 Time evolutionary profiles of the mixing index in the systems with different distance between tubes.	130

Figure 5.21 Contour plot of solid temperature at different times in the system with different distance between tubes of (a) 36.05 and (b) 41.2 mm.....	130
Figure 5.22 the spatial distribution of the time-averaged (26-30 s) surface-to-bed heat transfer coefficient, specifically focusing on convective heat transfer mechanisms around the immersed tube at a height of 0.1 m.	132
Figure 6.1 Architecture of the developed neural network.....	146
Figure 6.2 Example of the surface response plot for the relationship between the angle between tubes (A) and tube diameter (B) with the average solid volume fraction at a height of 0.065 m.	148
Figure 6.3 Evolution of training, validation, and test MSEs where output is (a) mixing index, (b) solid volume fraction, and (c) solid temperature.	150
Figure 6.4 Correlation coefficients of the input variables and output is (a) mixing index, (b) solid volume fraction, and (c) solid temperature.....	152
Figure 6.5 Comparisons of the mixing index between the obtained CFD-DEM results and ANN model prediction.....	155
Figure 6.6 Comparison of the CFD-DEM results with those calculated prediction by neural network for the mixing index.....	155
Figure 6.7 Comparisons of the axial solid volume fraction between the obtained CFD-DEM results and ANN model prediction for (a) in-line and (b) staggered immersed tubes configurations.	157
Figure 6.8 Comparison of the CFD-DEM results with those calculated prediction by neural network for the axial solid volume fraction.....	157
Figure 6.9 Comparisons of the axial solid temperature between the obtained CFD-DEM results and ANN model prediction for (a) in-line and (b) staggered immersed tubes configurations.	159
Figure 6.10 Comparison of the CFD-DEM results with those calculated prediction by neural network for the axial solid temperature.	159

CHAPTER 1

INTRODUCTION

1.1. Background

Bioeconomy is a concept that aims to utilize renewable biological resources sustainably to produce food, energy, and industrial goods while reducing the impact on the environment. It comprises a wide range of industries, including agriculture, forestry, fisheries, biotechnology, and energy. One of its main objectives is to reduce dependence on non-renewable resources like fossil fuels. Biofuels made from agricultural crops or algae provide an alternative to petroleum-based fuels. The utilization of advanced technologies, including biotechnology, information technology, and nanotechnology, is essential for achieving the goals of the bioeconomy, such as the generation of biomass for electricity production. As a result, the bioeconomy represents a transition towards a sustainable economic model that values natural resources and ecosystems, providing solutions to several global challenges, including food and energy security as well as climate change [1, 2].

Fluidized bed combustion technology has emerged as a promising biomass combustion technology to produce thermal power for electricity generation. This technology offers several advantages, such as effective gas-solid contacting, high heat transfer, and excellent emissions control. However, the physical properties of non-spherical biomass particles strongly influence hydrodynamics and heat transfer during fluidization, leading to undesirable fluidization behavior. The physical characteristics of biomass particles, including density, sphericity, and aspect ratio, need to be thoroughly investigated to understand their impact on fluidization [3, 4]. Studies have shown that adding a fluidization medium, such as spherical silica sand, can improve

the hydrodynamics characteristics of biomass particles [5]. However, the mixing behavior of biomass and inert particles can be complicated due to the significant differences in their properties. Moreover, the seasonal and regional availability of different types of biomasses can limit their use as fuel in the combustion process. Using a single type of biomass with low calorific value also results in low thermal efficiency. Therefore, mixed biomass fuels are commonly used to achieve high thermal efficiency [6]. Nevertheless, the different geometric characteristics and properties of various types of biomasses in the mixed biomass fuel can affect hydrodynamics behavior and heat transfer during fluidization. Additional study is required to better understand the impact of the geometric characteristics and operational conditions on the mixing behavior and heat transfer of mixed biomass and inert particles mixture in the fluidization process.

Heat transfer plays a crucial role in biomass combustion performance, as it is influenced by both physical and chemical processes. In a fluidized bed combustor, a large quantity of hot inert particles is fluidized by gas to form intense gas-solid multiphase flows, while biomass particles are continuously fed into the bed. When biomass particles come into contact with the bed, they quickly immerse with the hot inert particles to obtain heat for drying, devolatilizing, and burning. Poor dispersion of biomass particles can lead to significant fuel maldistribution, the accumulation of volatile matter and char in certain areas, and the formation of local reducing zones, which can affect combustion efficiency and reactor performance. As a result, understanding the detailed distribution of biomass particles is critical for improving biomass combustion performance and optimizing the design of the fluidized bed combustor [7].

Immersed tubes are commonly introduced into fluidized beds systems such as power plants and heat treatment industries, to enhance heat transfer and conversion rates, control bed temperature, and promote particle mixing. The tubes provide a large heat transfer area and alter gas-solid motion due to the breakage of gas bubbles flowing around the tubes, resulting in more efficient heat transfer [8]. To achieve optimal designs for fluidized bed combustors with immersed tubes, it is essential to investigate the local heat transfer phenomena occurring between particles and tubes. This investigation involves analyzing the heat transfer coefficient (HTC) to evaluate the efficiency of heat transfer, identify specific regions for potential improvement, and enhance the overall thermal performance of the system. Additionally, the arrangement of immersed tubes, such as in-line or staggered, has a significant impact on bubble dynamics, solid flow behavior, and heat exchange rates. These factors can be correlated with microscopic information such as local porosity and contact number between particles and immersed tubes. Proper design considerations aimed at improving fluidized bed combustors with immersed tubes and their configurations can lead to changes in hydrodynamics, fluid flow characteristics, solid particle contact with the fluid, solid residence time, and heat exchange rates [9].

Numerical simulation is more effective than experimental methods in obtaining detailed information about microscopic flow characteristics of particles during fluidization. Computational fluid dynamics coupled with discrete element method (CFD-DEM) is one of these simulation methods and can provide micro-scale information needed to understand fluidization in a fluidized bed. The CFD approach uses numerical analysis to solve and analyze fluid flow phenomena based on governing equations such as conservation of momentum, mass, and energy, while the

DEM approach can numerically simulate dynamic behaviors of particles treated as a discrete phase. To better comprehend and evaluate the fluidization and heat transfer phenomena of a biomass system, the CFD-DEM numerical simulation will be employed to examine the fluidization and heat transfer of the mixtures of biomass and inert particles in the developed fluidized bed combustor with immersed tubes.

CFD-DEM has been used in recent studies to investigate the impact of different tube arrangements on immersed tubes. However, there are limited studies on the use of mixed biomass and inert particle mixture in fluidized bed combustors with immersed tubes. Thus, it is necessary to explore the hydrodynamics and heat transfer between the immersed tubes and the fluid and solid particles within the system. It is also important to investigate the effects of different geometric characteristics of biomass and the appropriate proportions of mixed biomass fuel to determine the optimal size, loading and blending ratio that can achieve strong mixing intensity and efficient high heat transfer. Therefore, this research will investigate the hydrodynamics and heat transfer of the mixture of biomass and silica sand in the fluidized bed combustor with immersed tubes, using CFD-DEM simulation. Additionally, the effects of various sizes, arrangements, and pitch lengths of immersed tubes will be examined to determine the appropriate design for using the mixed biomass system in the fluidized bed combustor with immersed tubes. This study will also investigate how the size and proportion of mixed biomass affects hydrodynamics and heat transfer, in order to identify the optimal criteria for using biomass fuel in the combustion process. Finally, the simulation data obtained will be used to develop a data-driven model that can serve as an initial framework for measuring parameters such as temperature distribution and solid volume fraction in real industrial processes.

The study is expected to make significant theoretical advancements and have practical implications for biomass fluidized bed combustion.

1.2. Objectives

- 1.2.1. To design a biomass fluidized bed combustor with immersed tubes for improving hydrodynamics and heat transfer using CFD-DEM simulation.
- 1.2.2. To propose criteria for selecting suitable biomass fuel in a biomass fluidized bed combustor with immersed tubes using CFD-DEM simulation.
- 1.2.3. To develop a data-driven model for predicting system parameters during the real-time biomass fluidized bed combustor operation.

1.3. Scope of dissertation

- 1.3.1. Develop selection criteria for suitable mixed biomass particles, considering particle size distribution, for utilization as fuel in a biomass fluidized bed combustor. The criteria encompass varying aspect ratios, loadings, and blending ratios of mixed biomass in the biomass and sand particle mixture.
- 1.3.2. Design a fluidized bed combustor with immersed tubes for a biomass system, aiming to enhance the system's hydrodynamics, and heat transfer. This can be achieved by exploring variations in the angle between the tubes, tube diameter, and distance between tubes.
- 1.3.3. Develop data-driven models to predict parameters along the height of the biomass fluidized bed combustor with immersed tubes, including average mixing index, average radial solid volume fraction, and average radial temperature.

1.4. Structure of dissertation

The dissertation is structured into seven chapters and the outline of each chapter is given below:

Chapter 1 introduces the background, problem statement, purpose, and scope of the present research.

Chapter 2 provides a theoretical description of fluidization, the CFD-DEM coupling approach, the artificial neural network model, and a literature survey of experimental and simulation investigations of flow and heat transfer of non-spherical particle in fluidized bed systems.

Chapter 3 develops a CFD-DEM model using a suitable drag force model for cylindrical biomass particles and spherical silica sand particles.

Chapter 4 investigates the impact of different biomass types, loadings, and blending ratios on the hydrodynamics, heat transfer, and microscopic characteristics of mixed biomass particles and silica sand in a bubbling fluidized bed.

Chapter 5 examines the significance of design parameters of a fluidized bed combustor with immersed tubes using a 2^k factorial design of experiment.

Chapter 6 develops response surface methodology (RSM) and artificial neural network (ANN) models to predict system parameters during real-time operation without the need for CFD-DEM simulation.

Chapter 7 presents the overall conclusions drawn from the research conducted, highlights the main findings and implications, and suggests potential further studies in the same research direction.

CHAPTER 2

THEORY AND LITERATURE REVIEWS

2.1. Biomass

2.1.1. Biomass as a source of renewable energy

Biomass is an alternative and sustainable energy source that has numerous applications, such as generating heat and electricity via direct combustion, producing liquid fuel or chemicals through pyrolysis, and creating syngas through gasification. Biomass offers several benefits, including its eco-friendliness, worldwide availability, affordability in agricultural economies, and absence of net carbon dioxide emissions [10]. There is a growing interest in using biomass resources as a source of energy, particularly in the conversion of energy crops for the production of transportation fuels, direct combustion for heat generation, or co-firing with fossil fuels for power production. Biomass has a unique advantage over other renewable energy sources. It can be easily stored and has a widespread available across different geographic locations [11]. Energy derived from biomass and its byproducts is becoming a larger component of the current energy mix. Biomass materials can be transformed into liquids, solids, or gaseous fuels using various conversion processes that enhance their energy content. By using physical, chemical, or biological methods, biomass materials can be converted into fuels with better physicochemical properties, making them more compact, easy to store, and transferable. This conversion technology enables the transformation of carbonaceous solid materials that are unwieldy, low in energy density, and challenging to handle into fuels with improved energy characteristics, enhancing their economic viability [12].

2.1.2. Biomass characteristics and properties

Biomass materials exhibit a variety of characteristics that impact their effectiveness as fuel and the possible bioenergy pathways that can be employed.

1) Particle size/Dimensions

Biomass, similar to coal, is a heterogeneous material that poses challenges in achieving uniform particle sizes using conventional methods. Woody biomass, agricultural residues, and energy crops are examples of biomass resources that often exhibit a wide range of particle sizes, even after undergoing standard milling or size reduction techniques. Despite the difficulties in achieving uniformity in biomass particle size, combustion and processing plants are typically designed to efficiently handle materials with specific sizes and dimensions. Heating and processing systems incorporate mechanisms for material handling and transfer from storage to processing areas. As a result, the particle size and dimensions of biomass materials play a crucial role in ensuring the smooth operation of these processes [13].

2) Bulk density

Bulk density refers to the mass of a material divided by its volume. It is a measurement that quantifies how much mass is contained within a given unit of volume. The moisture content of a material and the processing methods employed are also crucial factors in determining its bulk density. For instance, wood pellets have a higher bulk density of approximately 660 kg/m³ compared to wood chips, which typically have a bulk density of around 250 kg/m³ [14].

3) Calorific value

Calorific value (CV) is the amount of heat energy released per unit of mass or volume of a fuel when it is burned completely. The calorific value of a fuel is determined by its chemical composition, including the amounts of carbon, hydrogen, oxygen, and other elements present in the fuel [15].

Gross calorific value (GCV), also known as Higher Heating Value (HHV), is a measure of the total energy content released when a fuel is completely burned. It represents the maximum amount of heat energy obtainable from a fuel, including the latent heat of vaporization of any water vapor produced during combustion.

Net Calorific Value (NCV), also known as Lower Heating Value (LHV), is a measure of the energy content of a fuel that considers the heat energy released during combustion while excluding the latent heat of vaporization of any water vapor produced.

4) Moisture content

Moisture content (MC) refers to the amount of water present in biomass material, either on a wet or dry basis. Both of these bases are used in the biomass industry, but suppliers generally use the wet basis calculation method because it offers a clearer indication of the material's water content [16].

5) Energy density

The energy density of a fuel is a crucial characteristic that indicates the amount of energy contained. It is determined by multiplying the calorific value of the fuel by its bulk density. The energy density value is essential for estimating the volumetric fuel

consumption rates of specific fuels, which is important when calculating the volume of resources required to meet a particular demand [14].

6) Chemical composition

The chemical composition of biomass varies depending on its specific type and source. However, in general, biomass predominantly comprises organic compounds containing carbon (C), hydrogen (H), and oxygen (O), which are its main constituents. The chemical composition of biomass significantly affects its properties and the combustion products it produces. The proportion of carbon and hydrogen in the biomass composition plays a crucial role in determining its calorific value, which ultimately determines its suitability for energy generation [14].

2.1.3. Categories of Biomass

Biomass encompasses a wide range of plant and animal materials, including wood from forests, crops, seaweed, agricultural and forestry residues, as well as organic waste from industries, humans, and animals [17]. In terms of bioenergy production globally, the primary sources include wood and wood wastes (64%), municipal solid wastes (24%), agricultural residues (5%), and landfill gases produced from organic waste decomposition (5%) [14]. However, the utilization of biomass for biofuel production, bio-chemicals, and direct energy generation is not limited to these sources alone. There is a diverse range of biomass materials used in the industry for electricity generation. This study provides a brief overview of some examples of biomass commonly employed in the electricity generation sector.

1) Woodchip

Woodchips, derived from forests or wood processing operations, offer numerous advantages as a biomass fuel for electricity generation through combustion. They find extensively used in different types of biomass boilers such as stoker, fluidized bed, and pellet boilers. The favorable combustion properties of woodchips stem from their high energy content and relatively low moisture content, resulting in efficient energy release and minimizing the need for additional drying procedures. With their high carbon content, woodchips are well-suited for combustion and heat generation. Furthermore, their widespread availability in various regions allows for sourcing from sustainably managed forests and wood processing industries. This ensures a reliable and environmentally friendly supply of biomass for electricity generation. By utilizing woodchips as biomass fuel, not only are forest resources effectively managed, but also the principles of the circular economy are upheld through the utilization of wood waste and residues [18, 19].

2) Sugarcane bagasse

Sugarcane bagasse is widely utilized as a biomass fuel for electricity generation through combustion. It offers numerous advantages as a fuel source. Bagasse, the fibrous residue left after extracting juice from sugarcane, can be effectively burned in various types of boilers such as spreader stoker, suspension-fired, and fluidized bed boilers. It exhibits favorable combustion properties due to its high cellulose content, resulting in efficient burning and energy release. With low moisture content, bagasse has an enhanced calorific value and requires minimal additional drying processes. The combustion of bagasse generates heat, which can be harnessed to produce electricity using steam turbines. Using the bagasse for electricity generation brings multiple

benefits. It promotes the use of renewable and sustainable energy sources, and reduces dependence on fossil fuels. Bagasse combustion contributes to the mitigation of greenhouse gas emissions since it is considered carbon-neutral, thanks to the CO₂ absorbed during sugarcane growth. Furthermore, utilizing bagasse as a fuel helps to utilize a byproduct that would otherwise go to waste or require disposal [20, 21].

Overall, woodchips and sugarcane bagasse are appealing biomass fuel options for electricity generation through combustion. Its availability, favorable combustion characteristics, and environmental advantages make it a promising choice for sustainable energy production, particularly in regions with sugarcane industries.

2.1.4. Energy generation from biomass

The processes by which biomass resources and feedstocks are utilized for energy generation and converted into alternative products are crucial to the bioenergy sector. In this sub-section, primary conversion pathways including direct combustion and thermochemical will be described.

2.1.4.1. Direct combustion

The direct combustion conversion pathway involves the complete combustion of biomass to generate heat and/or electricity, making it the most common utilization of biomass. This pathway also includes the co-firing of biomass with coal in existing and new coal-fired power plants [22].

1) Co-firing Biomass with Coal

Co-firing refers to the simultaneous combustion of biomass and coal to generate power. Since biomass is considered carbon neutral, co-firing biomass with coal can

reduce the total carbon emissions per unit of energy produced compared to using coal alone. The composition of coal and biomass differs, resulting in different emissions when co-fired. Research has demonstrated that co-firing biomass with coal can reduce NO_x and SO_x emissions compared to conventional coal plants. Additionally, co-firing can potentially lower fuel costs, reduce waste, and minimize soil and water pollution, depending on the properties of the biomass material used. Overall, co-firing can have positive environmental and economic impacts on power generation [22].

2) Different fuels for various combustion systems

2.1) Packed bed systems

Biomass feedstocks can be utilized in their original form or with minimal pre-processing. Typically, they have particle sizes ranging from 5 to 100 mm [11].

2.2) Fluidized bed systems

Biomass feedstocks are commonly pelletized or chipped into particles ranging from 2 to 5 mm to meet the fluidization requirements. However, larger particles can also be used, but they may require more energy during the processing phases [11].

2.3) Suspended systems

In this system, biomass feedstocks need to be finely ground to a particle size ranging from 10 μ m to 1000 μ m, to ensure complete combustion within a short residence time of a few seconds in the combustion chamber [11].

2.4) Direct firing, power stations and co-firing

Power stations typically require biomass fuels to be pulverized to a size comparable to that of coal to achieve the desired high combustion intensities. This involves grinding biomass particles to a size smaller than 1 mm or co-firing biomass with coal [11].

2.1.4.2. Thermochemical conversion

1) Pyrolysis

Pyrolysis is a thermochemical process in which biomass or other organic materials are heated in the absence of oxygen to break them down into smaller molecules. During pyrolysis, biomass is subjected to high temperatures, typically between 300 to 800 °C, causing it to decompose into valuable solid and liquid products. These products can include biochar (solid carbonaceous residue) and bio-oil (liquid) with the potential for energy recovery [23].

2) Gasification

Biomass gasification involves a high-temperature process known as extreme pyrolysis conversion, which aims to maximize gas production. This process generates syngas comprising Carbon Monoxide, Hydrogen, Methane, Carbon Dioxide, and Nitrogen. The resulting biogas exhibits remarkable versatility compared to the initial solid biomass. It can be utilized for various purposes, such as combustion to generate heat and/or steam for electricity production, as well as being employed in additional bio-refining processes. In addition, biomass gasification systems belong to the latest generation of biomass energy conversion technologies that are employed to improve the efficiency and decrease the investment expenses associated with bio-electricity production [24].

3) Fischer Tropsch Synthesis

The Fischer-Tropsch synthesis is highly valued for its ability to convert various carbon sources into liquid fuels, serving as an alternative to petroleum-based products. The primary objective of the Fischer-Tropsch synthesis is to produce long-

chain hydrocarbons from a mixture of carbon monoxide and hydrogen gases. This process is considered a crucial technology for generating synthetic fuels from renewable resources such as biomass and biogas, as well as for converting stranded natural gas or coal into usable liquid fuels. When the Fischer-Tropsch synthesis is conducted at lower temperatures, it yields a synthetic crude oil with a significant portion of heavy waxy hydrocarbons. In contrast, operating at higher temperatures results in the production of lighter synthetic crude oil and olefins, which are hydrocarbons with double bonds. Overall, the Fischer-Tropsch synthesis plays a vital role in enabling the production of synthetic fuels from diverse carbon sources, contributing to the development of a more sustainable and renewable energy landscape [25].

2.1.5. The drawbacks of biomass for energy production

Although biomass offers numerous advantages as a fuel source, there are also challenges associated with its utilization in energy pathways. In all combustion processes, there is a potential for the release of airborne pollutants. Additionally, the extensive cultivation of energy crops on deforested land or land that could otherwise be used for food production is a significant concern [11, 26]. Furthermore, many industrial processes generate biomass wastes and residues that hold potential for the bioenergy sector. Common industrial wood-based materials include untreated woods, treated woods, wood composites, and laminates. These materials may contain contaminants such as heavy metals, arsenic, and halogens, which can result in the production of hazardous or toxic by-products, as well as bottom ash, fly ash, and emissions in the form of flue gas. The fundamental technologies used for converting and generating energy from virgin woods are generally applicable to treated wood as

well. However, regulatory and environmental restrictions often necessitate the pretreatment of these materials to remove contaminants before they can be processed by the energy sector.

2.2. Fluidization

Fluidization is a phenomenon that occurs when solid particles are transformed into a fluid-like state by introducing a gas or liquid through it. In a fluidized state, the solid particles become suspended and exhibit fluid-like properties, such as the ability to flow and circulate. The key characteristic of fluidization is the balance between the upward flow of fluid and the downward force of gravity acting on the solid particles. When the upward fluid velocity exceeds a certain threshold known as the minimum fluidization velocity (U_{mf}), the particles start to rise and become suspended within the fluid. At this point, the bed of particles takes on a fluid-like behavior. Fluidization offers several advantages in industrial processes. It enhances mixing and heat transfer rates, allows for efficient contact between solid particles and a fluid, enables uniform distribution of gas or liquid throughout the system, and facilitates solid-gas or solid-liquid reactions. The behavior of fluidized systems is influenced by factors such as the properties of the solid particles (size, shape, density), fluid properties (velocity, viscosity), and the overall system design. Understanding the principles of fluidization is crucial for optimizing industrial processes that involve solid-fluid interactions. Fluidized beds are commonly used in processes such as combustion, catalytic cracking, drying, and particle coating [27].

2.2.1 Flow regime in fluidization

In fluidization, the flow regime refers to the pattern or behavior of the fluid and solid particles within the system. Different flow regimes can be observed depending on the superficial gas velocity (U_g) and the characteristics of the solid particles [28].

Fixed bed refers to a regime in fluidization when the U_g is low, and the solid particles are densely packed and stationary. The particles are in contact with each other, forming a stable bed. In this regime, the fluid flows through the void spaces between the particles, but there is no significant particle movement [29]. It is generally known that the maximum packing capacity of solid particles is about 0.63 [30]. Heat and mass transfer in this regime are typically limited due to the reduced mobility of the particles. The fixed bed is commonly used in industrial processes such as filtration, adsorption, and catalytic reactions, where the stationary bed of solid particles acts as a filter or catalyst bed. The fixed bed regime comes to an end when the U_g is equal to the U_{mf} , at which point the upward fluid force becomes greater than the weight of the solid particles.

Bubbling fluidized bed regime occurs at U_g is increased to minimum bubbling velocity (U_{mb}). In this regime, bubbles of gas or liquid start to form and rise within the bed of solid particles. As the bubbles rise, they carry solid particles with them, creating a bubbling motion within the bed. Additionally, the particles collide with each other and with the bubbles, resulting in bubble formation and characteristic bubbling behavior [31]. The bubbling fluidized bed regime offers advantages in various industrial processes. It promotes better mixing and heat transfer due to the increased particle movement and interaction. In addition, it allows for better contact

between solid particles and fluid, enhancing the efficiency of chemical reactions and mass transfer processes.

Turbulent fluidized bed refers to a fluidized bed system where the fluid flow within the bed exhibits turbulent characteristics. The fluid flow is characterized by irregular fluctuations, eddies, and mixing patterns. The particles within the bed experience more intense movement and collisions, leading to enhanced mixing and heat transfer rates. The turbulent fluidized bed regime can provide improved solid-gas contacting, which is beneficial for various chemical reactions and industrial processes [32]. Turbulent fluidized beds have applications in processes such as gas-solid reactions, combustion, drying, and particle mixing, where intense mixing and enhanced contact between solid particles and fluid are desired for efficient process performance.

Fast fluidization fluidized bed is characterized by high fluid velocities, intense particle mixing, and enhanced contact, making it well-suited for processes that demand efficient solid-gas interactions and rapid transport phenomena. In this regime, the bed of solid particles exhibits vigorous mixing and movement, while the fluid flow becomes turbulent due to high gas velocities. However, one concern when using this regime is the formation of a core annulus, which can be monitored by observing a low solid fraction (< 5% of the riser volume) at the middle of the riser compared to a high solid volume fraction at the wall regions (approximately 20% or higher as compared to the riser volume). This uneven distribution of solid particles can result in poor mixing properties in the riser [33].

Pneumatic transport takes place when the U_g is increased through the fast fluidization regime. In this regime, there is no accumulation of solid particles at the

bottom of the riser, which typically has a higher density and experiences significant pressure fluctuations. The minimum pneumatic velocity (U_{mp}) represents the critical value in this regime. It ensures that all solid particles are effectively dispersed within the gas phase and transported through the riser [34]. Pneumatic transport finds common applications in tasks such as conveying powders to storage or processing units, transferring materials between different stages of a production process, or transporting solid particles for reactions or treatments.

2.2.2. Biomass fluidized bed combustion

A biomass fluidized bed combustor is a system that generates electricity using biomass as fuel. The process involves feeding biomass, such as wood chips, agricultural residues, or energy crops, into the fluidized bed combustor, where it undergoes combustion. The fluidized bed facilitates good mixing and contact between the biomass fuel and the combustion air, resulting in efficient and complete combustion. The high temperature in the bed causes combustible gases and volatile compounds to be released from the biomass, which react with oxygen to produce heat. This heat is then transferred to a heat exchanger, which generates steam that drives a turbine connected to a generator, producing electricity. Opting for a biomass fluidized bed combustor rather than coal for electricity generation provides numerous advantages. Here are several benefits of biomass fluidized bed combustion in comparison to coal [3, 35] :

1) Renewable and Sustainable

Biomass is derived from organic sources, making it a renewable energy resource. Unlike coal, which is a finite fossil fuel, biomass can be continuously replenished through sustainable practices in forestry and agriculture.

2) Lower sulfur dioxide emissions

Biomass typically contains lower sulfur content than coal. Consequently, biomass combustion results in significantly reduced emissions of sulfur dioxide (SO₂), which contributes to acid rain and air pollution.

3) Reduced nitrogen oxide emissions

Biomass fluidized bed combustors are effective in reducing nitrogen oxide (NO_x) emissions. Compared to coal combustion, the turbulent combustion environment and efficient mixing in fluidized beds can help minimize the formation of NO_x.

4) Local economic benefits

The use of biomass for combustion can contribute to local economic development by utilizing locally sourced biomass feedstock. This creates opportunities for biomass producers, suppliers, and supporting industries, leading to the stimulation of local economies.

5) Waste management and resource valorization

Through biomass fluidized bed combustion, agricultural residues, forest waste, and other biomass byproducts can be effectively utilized, reducing the reliance on landfill disposal or open burning. By converting these waste materials into energy, biomass fluidized bed combustors contribute to waste management and the valorization of resources.

6) Potential for co-firing

Biomass fluidized bed combustors can be designed to enable co-firing with coal, providing a transitional approach towards renewable energy while utilizing existing coal infrastructure. Co-firing biomass with coal reduces greenhouse gas emissions and introduces a renewable energy component into the energy mix.

To ensure optimal performance and minimize environmental impact, it is crucial to consider factors such as biomass feedstock quality, sustainable sourcing, efficient combustion practices, and proper emissions control technologies in biomass fluidized bed combustion. Nevertheless, biomass fluidized bed combustion generally provides significant environmental and socio-economic benefits compared to coal combustion.

2.2.3. Effect of immersed surfaces in fluidized bed

The presence of an immersed surface in fluidization can have various effects on the behavior and performance of the fluidized bed system. Here are some of the key effects [36-38]:

1) Flow characteristics

The presence of an immersed surface can influence the flow distribution within the fluidized bed. It can cause changes in the fluid dynamics, leading to variations in fluid velocity and pressure distribution. This can impact the overall performance and behavior of the fluidized bed system.

2) Heat transfer enhancement

The presence of immersed surfaces, such as heat exchanger tubes or heating elements, in fluidized beds can greatly enhance heat transfer. The direct contact between the immersed surface and the fluidized particles facilitates efficient heat transfer through conduction and convection. This is particularly advantageous in processes that involve heat exchange or thermal treatments, as it enables faster and more effective heating or cooling of the particles.

3) Mass transfer improvement

Immersed surfaces in fluidized beds can also enhance mass transfer processes. For instance, in chemical reactions or absorption processes, the presence of immersed surfaces increases the contact area between the solid particles and the fluid, resulting in improved mass transfer rates. This is vital for achieving efficient reaction kinetics and optimizing the performance of mass transfer operations.

4) Bed stability and particle agglomeration prevention

Immersed surfaces can assist in maintaining bed stability and preventing particle agglomeration in fluidized beds. By providing additional contact points and surfaces for particle attachment, the immersed surfaces can distribute the particle load more uniformly, reducing the likelihood of localized agglomeration and promoting consistent fluidization throughout the bed. This is essential for ensuring efficient solid-gas interactions and avoiding issues such as channeling or hot spots in the bed, which can negatively impact process performance.

Overall, the presence of immersed surfaces in fluidized beds has significant implications for heat and mass transfer, bed stability, particle dynamics, and process performance. Proper design and optimization of the immersed surfaces are necessary to harness these effects and maximize the efficiency and effectiveness of fluidized bed systems.

2.3. Computational fluid dynamics-Discrete element method approach

This section provides a comprehensive explanation of the CFD-DEM approach, which involves the equations for both a discrete solid (such as non-spherical particles) and the continuum phase (gas). It includes information on the collision model, drag model, and heat transfer model. The specific equations can be found in the subsequent subsections.

2.3.1. Computational fluid dynamics

Computational Fluid Dynamics (CFD) is a branch within fluid mechanics that focuses on using numerical methods and algorithms to simulate and analyze the behavior of fluid flow. This involves solving the governing equations of fluid motion, such as the Navier-Stokes equations, to predict and comprehend properties such as flow patterns, velocity profiles, and pressure distribution. The fluid is considered as a continuum phase, which is modeled similar to the conventional two-fluid model (TFM) [39]. The equations used for this modeling are volume-averaged Navier-Stokes equations expressed in terms of the locally averaged variables over a computational cell as follows:

$$\frac{\partial(\rho_f \varepsilon_f)}{\partial t} + \nabla \cdot (\rho_f \varepsilon_f \mathbf{u}) = 0 \quad (1)$$

$$\frac{\partial(\rho_f \varepsilon_f \mathbf{u})}{\partial t} + \nabla \cdot (\rho_f \varepsilon_f \mathbf{u} \mathbf{u}) = -\nabla P + \nabla \cdot (\varepsilon_f \boldsymbol{\tau}) + \rho_f \varepsilon_f \mathbf{g} - \mathbf{F}_{pf} \quad (2)$$

$$\frac{\partial(\rho_f \varepsilon_f c_{p,f} T_f)}{\partial t} + \nabla \cdot (\rho_f \varepsilon_f \mathbf{u} c_{p,f} T_f) = \nabla \cdot (\varepsilon_f k_f \nabla T_f) - Q_{pf} \quad (3)$$

whereas

$$\varepsilon_f = 1 - \left(\sum_{i=1}^{k_v} V_i \right) / \Delta V \quad (4)$$

where ρ_f , \mathbf{u} , P , T_f , ε_f , \mathbf{F}_{pf} and Q_{pf} are the fluid density, fluid velocity, pressure, temperature, local porosity, volumetric fluid-particle interaction force and fluid-particle energy exchanges, respectively. In addition, V_i is the volume of particle i (or part of the volume if particle is not fully in the CFD cell) and k_v is the number of particles in the computational cell of volume ΔV . The fluid viscous stress tensor $\boldsymbol{\tau}$ is written as [40]

$$\boldsymbol{\tau} = \mu_e [(\nabla \mathbf{u}) + (\nabla \mathbf{u})^{-1}] - \frac{2}{3} \mu_e (\nabla \cdot \mathbf{u}) \delta_k \quad (5)$$

where μ_e is the fluid effective viscosity determined by the widely used standard k - ε turbulence model [40, 41] and δ_k is Kronecker delta, respectively. The challenge in studying granular systems lies in the inherent complexity of solid flow dynamics, making it difficult to derive general equations. However, the accuracy of the continuous approach in generating reliable results depends on the constitutive relations employed to model interactions between the phases and the rheology of the particulate material, both of which are challenging to obtain [42]. Additionally, the continuum interpenetrating approach used in this context lacks individual particle information, which might be desired for certain analyses. Moreover, specifying a particle size distribution can significantly increase computational costs, as multiple phases need to be created to model different particle sizes.

2.3.2. Discrete element method

The Discrete Element Method (DEM) is a numerical modeling technique that was first introduced by Cundall and Strack [43]. It was primarily developed as a complementary method to the Finite Element Method, aiming to solve complex engineering and applied science problems, particularly those involving granular flow

of differently shaped particles that display sporadic conduct [44]. DEM simulations offer the advantage of providing dynamic information that is challenging to obtain through traditional experiments. This includes analyzing individual particle trajectories, transient forces acting on particles, and studying the behavior of interacting, deformable, discontinuous, or fractured elements undergoing rotations and large displacements [45, 46]. With the advancement of computational power, modern simulation software enables repeated calculations for each element of the system millions of times per second. This allows for simulations with over a million particles, making the DEM approach more practical [47]. In DEM modeling, particle-particle interactions are treated as dynamic processes and solved using explicit numerical schemes. The contact forces, rotations, momentum, and displacements of stressed particles are tracked by considering each contact between individual particles [48]. A primary assumption in DEM is that every discrete element has distinct boundaries that physically separate it from other elements in the analysis. As the elements move within the domain, the equations describing translation and rotation behaviors are applied to each element individually, considering the boundary forces between contacting elements. The deformation resulting from collisions can be decoupled from the average motion and expressed as the sum of the normal modes of the bodies. This leads to a new set of decoupled modal equations, which are then solved using an explicit central difference scheme. In addition, the final solution is obtained through modal superposition [46, 49].

Within DEM modeling, the movements of particles can be categorized into two types: translation and rotation, which are governed by Newton's second law of motion. The models for translation and rotation are expressed as follows:

$$m_i \frac{d\mathbf{v}_i}{dt} = m_i \mathbf{g} + \sum_{j=1}^k \mathbf{F}_{c,ij} + \mathbf{F}_{pf,i} \quad (6)$$

$$I_i \frac{d\boldsymbol{\omega}_i}{dt} = \sum_{j=1}^k \mathbf{M}_{t,ij} \quad (7)$$

where m_i , I_i , \mathbf{v}_i and $\boldsymbol{\omega}_i$ are the mass, moment of inertia, translational velocity and angular velocity of the particle i , respectively. The forces acting on a particle considered in this research are the gravitational force $m_i \mathbf{g}$, the total contact force $\mathbf{F}_{c,ij}$ from its k neighboring particles and/or walls, and the particle-fluid interaction force $\mathbf{F}_{pf,i}$ which mainly consists of the drag force $\mathbf{F}_{d,i}$ and the pressure gradient force $\mathbf{F}_{pg,i}$. The torques acting on the particle i due to the neighboring particles includes $\mathbf{M}_{t,ij}$ which is generated by the tangential force and causes particle i to rotate. For possible multiple interactions of particle i , the interaction forces and torques between each pair of particles are summed. The most of force and torque equations are well documented in the literatures [45, 50]. Note that the contact between particles occurs at a specific area rather than a single point, which can result in the particles slightly overlapping on the normal and tangential coordinates [45]. Particle overlapping cannot be neglected because it has a significant impact on simulation results [51]. Thus, the contact force experienced by particle i due to its contact with particle j at the contact plane can be analyzed in terms of its normal and tangential forces, which are represented by $F_{cn,ij}$ and $F_{ct,ij}$, respectively. In the case of spherical particles, the contact plane is perpendicular to the line that connects the centers of the two spheres. However, for non-spherical particles, the contact plane can be determined by considering the closest points of the two particles, the closest points of a particle and a triangle, or the two points with the maximum overlap distance in the case of a

physical contact [52]. Figure 2.2 indicates a schematic illustration of the typical contact force vectors with overlapping and torques implicated in the DEM modeling.

To model the normal contact force, the Hysteretic Linear Spring model [52] is employed, which enables simulation of plastic energy dissipation during contact without significantly increasing the simulation time. In this model, no viscous damping term is utilized, which means that energy dissipation remains unaffected by neighboring contacts since the velocities of neighboring particles are not taken into account [53]. The equations that describe this model are presented below:

$$F_{cn,i}^t = \begin{cases} \min\left(K_{nl} s_n^t, F_{cn,ij}^{t-\Delta t} + K_{nu} \Delta s_n\right), & \text{if } \Delta s_n \geq 0 \\ \max\left(F_{cn,i}^{t-\Delta t} + K_{nu} \Delta s_n, 0.001K_{nl} s_n^t\right), & \text{if } \Delta s_n < 0 \end{cases} \quad (8)$$

$$\Delta s_n = s_n^t - s_n^{t-\Delta t} \quad (9)$$

where $F_{cn,i}^t$ and $F_{cn,i}^{t-\Delta t}$ are the normal contact forces acting on the particle i at the current time t and at the previous time $t-\Delta t$ respectively, where Δt is the timestep. Δs_n is the change in the overlapping during the time step, s_n^t , $s_n^{t-\Delta t}$ are the normal overlap values at the current and at the previous time, respectively. K_{nu} and K_{nl} are the unloading and loading contact stiffnesses, respectively. Note that the unloading force is limited by the value of $0.001K_{nl} s_n^t$ to ensure that the normal force becomes zero with zero overlappings [50]. Figure 2.3 illustrates the overlapping circle (A-C) resulting from the loading and unloading response due to the normal force effect, with the shaded region indicating the dissipated energy during particle contact. The slopes of the loading and unloading lines are denoted by K_{nl} and K_{nu} , respectively. Plastic deformation occurs only during contact between particles i and j , with residual deformation disregarded thereafter. Furthermore, the user can specify the coefficient

of restitution ε that represents the energy dissipation for the interactions between particles or between particles and walls. The loading and unloading stiffness are defined as:

$$\frac{1}{K_{nl}} = \begin{cases} \frac{1}{K_{nl,i}} + \frac{1}{K_{nl,j}}, & \text{particle - particle} \\ \frac{1}{K_{nl,i}} + \frac{1}{K_{nl,w}}, & \text{particle - wall} \end{cases} \quad (10)$$

$$K_{nu} = \frac{K_{nl}}{\varepsilon^2} \quad (11)$$

whereas:

$$K_{nl,i} = E_i Z \quad (12)$$

$$K_{nl,k} = E_w Z \quad (13)$$

where E_i and E_w are Young's modulus of particle and boundary, respectively, and Z is representing the particle size or geometry.

To model the tangential contact force, the Linear Spring Coulomb Limit model is utilized, which takes into account the sliding behavior of particles during tangential contact. This model is crucial in determining the total tangential contact forces. The equation for this model is as follows [54]:

$$F_{ct,i}^t = \min \left(F_{ct,i}^{t-\Delta t} + K_{nl} \Delta s_t^t, \mu F_{cn,i}^t \right) \quad (14)$$

where $F_{ct,i}^t$ and $F_{ct,i}^{t-\Delta t}$ are the tangential contact forces at the current and previous time of the simulation, respectively, Δs_t^t is the change in the tangential overlapping during the time step, and μ is the friction coefficient which can be defined as a static μ_s if no sliding at the contact and a dynamic μ_d if sliding act at the contact, which depending on the tangential sliding contact. If the tangential force surpasses the limit

of $\mu_s F_{cn,i}^l$, it indicates the occurrence of sliding at the contact. Once the force drops below this threshold, the contact is considered non-sliding again.

The heat transfer calculation in this study considers the exchange of heat between particle i and its surroundings, which occurs through conduction with other particles and walls, as well as convection with the fluid. Based on the principle of heat balance, the governing equation for particle i can be expressed as:

$$\frac{m_i c_{p,i} dT_i}{dt} = \sum_{j=1}^k q_{i,j} + q_{conv,i} \quad (15)$$

The conductive heat transfer is calculated as follows:

$$q_{i,j} = H_c (T_i - T_j) \quad (16)$$

whereas

$$H_c = 2k_c a \quad (17)$$

$$k_c = 2 / \left(1/k_{c,i} + 1/k_{c,j} \right) \quad (18)$$

$$a = \left(3F_{cn} R^* / 4E^* \right)^{1/3} \quad (19)$$

where $q_{i,j}$ is the conductive heat transfer rate between particles i and j or walls. Here, H_c is the contact conductance proposed by Batchelor & O'Brien [55]. k_c , $k_{c,i}$ and $k_{c,j}$ are the equivalent thermal conductivity of the contact and thermal conductivities of the two contacting entities, respectively. a is the radius of the contact surface determined by Hertz theory.

The equivalent radius, R^* and effective Young's modulus, E^* are defined as [56]

$$\frac{1}{R^*} = \begin{cases} \frac{2}{Z_i} + \frac{2}{Z_j}, & \text{particle - particle} \\ \frac{2}{Z}, & \text{particle - wall} \end{cases} \quad (20)$$

$$\frac{1}{E^*} = \frac{1-\nu_i^2}{E_i} + \frac{1-\nu_j^2}{E_j} \quad (21)$$

in which Z_i and Z_j are the sizes of the contacting particles in a particle-particle collision, E_i and E_j are the Young's moduli of the two contacting particles or the particle and the wall, and ν_i and ν_j are the respective Poisson's ratios. Figure 2.4 illustrates the conductive heat transfer between two colliding particles.

The convective heat transfer is calculated as follows:

$$q_{conv,i} = h_f A_{p,i} (T_{f,i} - T_{p,i}) \quad (22)$$

whereas:

$$h_{f,i} = Nu_i k_f / d_{eq,i} \quad (23)$$

$$Nu_i = (7 - 10\varepsilon_{f,i} + 5\varepsilon_{f,i}^2) (1 + 0.7 Re_{p,i}^{0.2} Pr_{f,i}^{0.33}) + (1.33 - 2.4\varepsilon_{f,i} + 1.2\varepsilon_{f,i}^2) Re_{p,i}^{0.7} Pr_{f,i}^{0.33} \quad (24)$$

where $h_{f,i}$ is the interphase heat transfer coefficient and $A_{p,i}$ is the particle surface area.

To calculate the interphase heat transfer coefficient, the Nusselt number correlation proposed by Gunn [57] is employed.

The DEM approach becomes significantly simplified when particle-particle interactions are neglected. However, this assumption is only valid when the dispersed second phase occupies a low volume fraction, which is not typically the case in most industrial applications. Since the model does not resolve particle interactions, it is

unsuitable for scenarios where the volume fraction of the second phase cannot be ignored, such as fluidized beds. In such applications, it is necessary to consider particle-particle interactions when solving for the dispersed phase.

2.3.3. CFD-DEM coupling

The coupled CFD-DEM approach presents a promising alternative for modeling systems involving granular-fluid interactions as it enables the representation of discrete particle behavior while maintaining computational feasibility. This is achieved by solving the fluid flow at a cell level rather than explicitly considering each individual particle. By reducing the computational requirements associated with fluid calculations, this approach expands the scope of equipment and processes that can be effectively studied using numerical simulations. In the CFD-DEM method, the fluid flow is determined through the conventional continuum approach, providing essential information for calculating the fluid forces acting on individual particles. Meanwhile, the particle motion is obtained using a discrete particle method, allowing for an accurate representation of particle behavior within the system. To model granular systems, using CFD-DEM is advantageous over using only CFD because CFD-DEM does not require equations of state-motion that are challenging to obtain due to the simulation of every particle and consideration of particle-particle interactions. Unlike the limitations of low particle size concentration, CFD-DEM enables easy prescription of particle size distribution without increasing the computational cost of the CFD solver. Moreover, CFD-DEM can handle non-spherical particles and simulate adhesive-cohesive materials by modeling attractive forces between particles and walls or between particle pairs [56].

In the coupling scheme, interphase interactions are calculated separately for each discrete particle. Afterwards, the properties of the particles are interpolated to the fluid cell. The interphase momentum and energy exchanges are then determined using the equations provided below:

$$\mathbf{F}_{pf} = \frac{\sum_{i=1}^{k_v} (\mathbf{F}_{d,i} + \mathbf{F}_{pg,i})}{\Delta V} \quad (25)$$

$$Q_{pf} = \sum_{i=1}^{k_v} (q_{conv,i}) / \Delta V \quad (26)$$

The drag and pressure gradient are calculated as:

$$\mathbf{F}_{d,i} = 0.5 C_D \rho_f A_{\perp,i} |\mathbf{u}_f - \mathbf{v}_i| (\mathbf{u}_f - \mathbf{v}_i) \quad (27)$$

$$\mathbf{F}_{pg,i} = -V_i \nabla P \quad (28)$$

where C_D is the drag coefficient, $A_{\perp,i}$ is the projected particle area in the flow direction and $\mathbf{u}_f - \mathbf{v}_i$ is the relative velocity between fluid and particle.

Syamlal and O'Brien [58] developed a drag coefficient formula for dense particle flows in fluidization systems, but this conventional model tends to over-predict the drag coefficient for smaller Reynolds numbers. To calculate the drag coefficient in this study, the parameterized Syamlal & O'Brien model is adopted, which is an improved version of the original model [56]. The parameterized model adjusts two constant parameters based on the fluid properties and the expected U_{mf} of the particle, making it more accurate and overcoming the original's tendency to over-predict bed expansion [59]. The parameterized Syamlal & O'Brien drag coefficient is defined as follows [56]:

$$C_D = \frac{\alpha_f}{g^2} C_{D,s} \quad (29)$$

$$C_{D,s} = \left(0.63 + 4.8 / \sqrt{\frac{\text{Re}_p}{g}} \right)^2 \quad (30)$$

whereas:

$$\text{Re}_p = \rho_f |u_f - v_i| d_{eq,i} / \mu_f \quad (31)$$

$$g = 0.5 \left[A - 0.06 \text{Re}_p + \sqrt{0.0036 \text{Re}_p^2 + 0.12 \text{Re}_p (2B - A) + A^2} \right] \quad (32)$$

where $C_{D,s}$ is the single particle drag coefficient, α_f is the fluid volume fraction, Re_p is relative particle Reynolds number, μ_f is fluid viscosity and g is terminal velocity ratio.

In equation (32), A and B are functions of the fluid volume fraction as:

$$A = \alpha_f^{4.14} \quad (33)$$

$$B = \begin{cases} c_1 \alpha_f^{1.28}, & \alpha_f \leq 0.85 \\ \alpha_f^{d_1}, & \alpha_f > 0.85 \end{cases} \quad (34)$$

$$d_1 = 1.28 + \frac{\log_{10} c_1}{\log_{10} 0.85} \quad (35)$$

where c_1 and d_1 are parameters of the parameterized Syamlal & O'Brien model that must be defined.

The flowchart of the CFD-DEM coupling scheme in this study is presented in Figure 2.5. In summary, at each time step, the computational process begins with CFD calculating the fluid flow field and providing the necessary information to DEM. DEM then utilizes this data to determine the forces, positions, velocities, and heat transfer rates of individual particles, allowing for the evaluation of porosity, volumetric particle-fluid forces, and energies within a computational cell.

Subsequently, CFD employs this information to calculate the fluid flow field for the subsequent time step, which is then utilized to determine the particle-fluid forces acting on each individual particle. This process ultimately leads to the determination of the particle's new position and velocity for the next time step [56].

2.4. Artificial neural network

An artificial neural network (ANN) is a computational model inspired by the structure and functioning of biological neural networks, such as the human brain. It is a mathematical model that consists of interconnected processing units, which are called artificial neurons or nodes. These neurons work together to process and transmit information. The fundamental component of an artificial neural network is the artificial neuron, which takes in multiple inputs, performs a computation on them, and generates an output. To accomplish this, each input is multiplied by a weight that corresponds to it, and the weighted inputs are then summed together. The sum is subsequently passed through an activation function, which introduces non-linear behavior into the network, and the output of the neuron is the result. The artificial neurons are organized into layers within the neural network. Training an artificial neural network involves presenting it with a set of labeled input data, known as the training set, and adjusting the weights of the connections based on the errors between the predicted outputs and the desired outputs. This process is typically done using optimization algorithms, such as backpropagation, which calculates the gradients of the network's error with respect to the weights and updates them accordingly [60].

There are several types of neural networks, each designed for different purposes and to solve particular problems. Here are some commonly used types of neural networks:

1) Feedforward Neural Networks (FNNs) or Multi-Layer Perceptrons (MLPs)

The networks are a type of neural network that includes an input layer, one or more hidden layers, and an output layer. In MLPs, information flows in a unidirectional manner, moving from the input layer through the hidden layers to the output layer. Each layer is comprised of multiple neurons, and there are connections established between neurons in adjacent layers. During the training or learning process, the weights of these connections are adjusted, allowing the network to learn and recognize patterns and relationships in the input data. MLPs are widely used for tasks such as classification, regression, and pattern recognition [61].

2) Convolutional Neural Networks (CNNs)

The networks are specifically designed to handle data with a grid-like structure, such as images or videos. These networks employ convolutional layers that are adept at extracting local features from the input data, allowing them to capture spatial hierarchies. CNNs have proven to be highly effective in tasks such as object recognition and image classification, as they can automatically learn and identify patterns and features within the data. By using convolutional filters, pooling layers, and non-linear activation functions, CNNs can process and analyze visual information with remarkable accuracy and efficiency [62].

3) Recurrent Neural Networks (RNNs)

The networks are specifically designed to handle sequential data, such as time series or natural language. RNNs possess recurrent connections that enable information to

be stored and propagated across different time steps. This distinctive feature allows RNNs to capture temporal dependencies and context in the data, making them well-suited for tasks that involve sequences or dynamic patterns. By retaining a memory of past inputs, RNNs can utilize this context to make informed predictions or classifications [62].

4) Long Short-Term Memory Networks (LSTMs)

The networks are a specific type of RNN designed to overcome the issue of vanishing gradients that can occur during RNN training. LSTMs are particularly effective when working with long sequences of data, such as those encountered in speech recognition and language translation tasks. They have the capability to capture and retain long-term dependencies in the data by utilizing a memory cell and a set of gates that control the flow of information. This enables LSTMs to selectively remember or forget information over time, making them well-suited for tasks that involve processing and understanding sequential data with long-term dependencies [63].

5) Generative Adversarial Networks (GANs)

The networks are a type of neural network that is designed to generate new data that resembles training data. GANs utilize a unique architecture consisting of two networks: a generator network that produces new data and a discriminator network that evaluates the quality of the generated data. During training, the generator network attempts to produce data that can fool the discriminator network into believing it is real, while the discriminator network learns to distinguish between real and fake data. Through this adversarial process, the generator network gradually improves its ability to generate realistic data [64].

Moreover, there are several types of activation functions commonly used in neural networks, including [65]:

1) Sigmoid function

The sigmoid function is a smooth, S-shaped curve that maps the input to a value between 0 and 1. It is given by the formula, $f(x) = 1 / (1 + e^{-x})$.

2) Hyperbolic Tangent (Tanh) function

The tanh function is similar to the sigmoid function but maps the input to a value between -1 and 1. It is given by the formula, $f(x) = (e^x - e^{-x}) / (e^x + e^{-x})$.

3) Rectified Linear Unit (ReLU) function

The ReLU function returns the input if it is positive, and 0 otherwise. It is defined as $f(x) = \max(0, x)$.

4) Leaky ReLU function

The leaky ReLU is a variation of the ReLU function that introduces a small slope for negative inputs. It is defined as $f(x) = \max(ax, x)$, where a is a small positive constant.

5) Exponential Linear Unit (ELU) function

The ELU function is similar to the ReLU function for positive inputs but has a non-zero output for negative inputs. It is defined as $f(x) = x$ if $x > 0$ and $f(x) = \alpha(e^x - 1)$ if $x \leq 0$, where α is a hyperparameter that controls the negativity of the function.

However, the choice of activation function depends on the specific requirements and characteristics of the neural network architecture.

The ANN is utilized in a wide range of applications, including pattern recognition, speech and image recognition, decision-making tasks, natural language processing, and forecasting. It is particularly adept at solving problems that are too

complicated for conventional programming techniques by learning complex patterns. Additionally, it is applied to fluidized bed combustion to model and forecast behavior such as combustion efficiency, emissions, and temperature distribution. Moreover, it has been used for control purposes, such as controlling the air-to-fuel ratio and predicting bed height and pressure drop. Thus, ANNs have proven to be powerful tools for optimizing and enhancing the performance of fluidized bed combustion systems.

2.5. Literature review

Ma et al. [66] used a CFD-DEM coupling method to study the fluidization of rod-like particles with varying aspect ratios to understand the impact of particle shape and size on fluidization properties. The simulation results showed that, compared to spherical particles, rod-like particles with smaller aspect ratios exhibited high mixing and intense motion. However, due to their greater tendency to experience larger forces and absorb more energy from the fluid flow, these particles also resulted in the appearance of a significant number of bubbles and channels flow, or even slugging. This resulted in larger fluctuations in pressure drop and faster velocity of mixing. Therefore, the developed model will be used to investigate the effect of aspect ratios of rod-like particles on fluidization quality, which is a critical criterion for evaluating fluidization in practical production processes.

Ma and Zhao [67] employed a CFD-DEM model to investigate the impact of the fraction of rod-like particles on the flow and mixing behavior of binary mixtures in fluidized beds. The binary mixtures consisted of rod-like particles representing biomass particles and spherical particles representing inert bed material. The results demonstrated that the minimum fluidization velocity increased as the volume fraction

of rod-like particles increased. This indicated that the systems operated in different flow regimes while maintaining the same superficial velocity. Notably, the addition of spherical particles aided in the fluidization of rod-like particles, resulting in stronger fluidization compared to a system composed solely of monodisperse rod-like particles. Moreover, both increasing the superficial velocity and decreasing the volume fraction of rod-like particles enhanced the mixing rate in binary granular systems. These findings highlight the importance of understanding fluidization in binary mixtures for the improved utilization of biomass in fluidization processes.

Mema and Padding [68] conducted a CFD-DEM simulation to compare the mixing characteristics of spherical particles (AR-1) with elongated spherocylindrical particles having an aspect ratio of 4 (AR-4) in a fluidized bed. The results showed that AR-4 particles exhibited more vigorous mixing and shorter mixing times due to the increased turbulence in the fluidization process. Additionally, for AR-4 particles, the inclusion of hydrodynamic lift and torque led to a higher average particle velocity in the vertical direction, resulting in enhanced mixing and reduced mixing times. These findings highlight the significance of considering the effects of hydrodynamic lift and torque on the mixing properties of AR-4 particles.

Pérez et al. [69] conducted a study on the size and shape distribution of raw sugarcane bagasse, which are important factors influencing the physical properties of the material for its use in fluidized beds. Sugarcane bagasse exhibited a longer length compared to other analyzed biomasses, while the width was relatively similar. The aspect ratio varied with particle size, ranging from 2.14 to 5.5. For particles with diameters less than 0.3 mm, the aspect ratio behaved similarly to other biomasses, with a value of 2.5. Additionally, the sphericity value ranged from 0.27 to 0.558. It

was anticipated that more accurate methodologies for determining aspect ratio, sphericity, and size distribution would yield improved results in simulating binary mixtures in fluidized beds. Gaining a better understanding of the hydrodynamic characteristics of the material within the bed will facilitate enhanced fluidized bed design and operation.

Centeno-González et al. [70] employed CFD simulation to develop a model for bagasse combustion in an industrial boiler. The simulation results indicated that larger particles had a higher likelihood of complete burning on the grate, while smaller particles tended to burn within the furnace and exit the boiler as char. Hence, it was crucial to understand the initial size distribution of the biomass fuel for efficient combustion. Additionally, devolatilization played a significant role as it assisted in predicting the thermal field. The overall efficiency derived from the analysis of particle combustion could be utilized to compare the impacts of different designs and operational parameters on boiler performance, based on the simulation outcomes.

Oppong [71] described the heat transfer mechanisms in a fluidized bed, as well as the performance parameters that influence heat transfer and fluidized bed performance. CFD-DEM had been shown to be very effective in modeling and predicting heat transfers and characteristic behavior. The bed heat transfer phenomena and overall performance were influenced by several parameters including particle size, bed temperature, suspension density and superficial gas velocity. Furthermore, the bed heat transfer and hydrodynamics behavior also varied depending on bed geometry and design. A thorough understanding of the combustion process and heat transfer modes then provides the achievement of high thermal efficiency operation.

Hau and Lim [72] conducted a CFD simulation to examine the influence of particle size and immersed tube temperature on bubbling and heat transfer behavior in a fluidized bed. The results revealed that when large gas bubbles encountered the immersed tubes, they split into two smaller bubbles. Moreover, an increase in particle size led to the formation of larger gas bubbles within the system. Consequently, more gas pockets formed around the tubes, resulting in a reduced heat transfer coefficient. Additionally, as the tube temperature increased, the heat transfer process became more sensitive to the formation of gas pockets around the immersed tube. The findings suggest that the design and optimization of a fluidized bed with a bank of immersed tubes can be employed in integrating a fluidized bed reactor heat-exchanger system.

Hou et al. [73] employed CFD-DEM to investigate the impact of material properties and geometrical settings on flow and heat transfer characteristics in a fluidized bed. The study found that convective heat transfer dominated in the case of large non-cohesive particles, while conductive heat transfer was more significant for small cohesive particles. Material properties and gas velocity influenced the uniformity of particle velocity and temperature distribution within the bed. The arrangement of a tube array, including in-line and staggered configurations, played a crucial role in altering flow behavior and heat exchange rates. The heat exchange rate exhibited complex variations when the pitch length and angle were modified. The contact number served as a key indicator for determining conductive heat exchange rates, whereas local porosity had a close relationship with convective heat transfer. This information can prove valuable in the design and optimization of tube arrays for efficient heat transfer in fluidized beds.

Xue et al. [74] used CFD-DEM to explore the influence of solid properties on heat transfer characteristics in a fluidized bed. The study highlighted the significance of the violent convective mechanism at the bottom of the bed in heating the bed material. Additionally, the entrainment of rising bubbles and solid mixing played vital roles in achieving better temperature uniformity throughout the heating process. The internal circulation of solids was found to be strengthened under the same superficial velocity but slightly weakened under the same fluidization number, due to reductions in particle density and size. Moreover, an increase in solid capacity enhanced solid mixing and a more uniform bed temperature, thereby confirming the significant impact of gas temperature on flow behavior. Consequently, comprehending the key hydrodynamics and thermal behavior of fluidized beds is essential for ensuring effective operation of this equipment.

Bisognin et al. [75] employed a combination of CFD and design of experiment techniques to examine the influence of various variables on the tube-to-bed heat transfer coefficient in a gas-solid fluidized bed heat exchanger. A 2^{5-1} fractional factorial design was utilized to investigate five variables. The results demonstrated that particle size exerted the most significant impact on the heat transfer coefficient. Additionally, the geometrical parameters, such as the immersed tube bundle, tube diameter, and distance between tubes, also played a significant role in the heat transfer coefficient due to their effect on solid pattern circulation within the bed. On the other hand, gas velocity exhibited the least influence on the heat transfer coefficient, while particle thermal conductivity had a negligible effect. Consequently, when designing a fluidized bed, the selection of an appropriate heat transfer material should prioritize particles with smaller diameters.

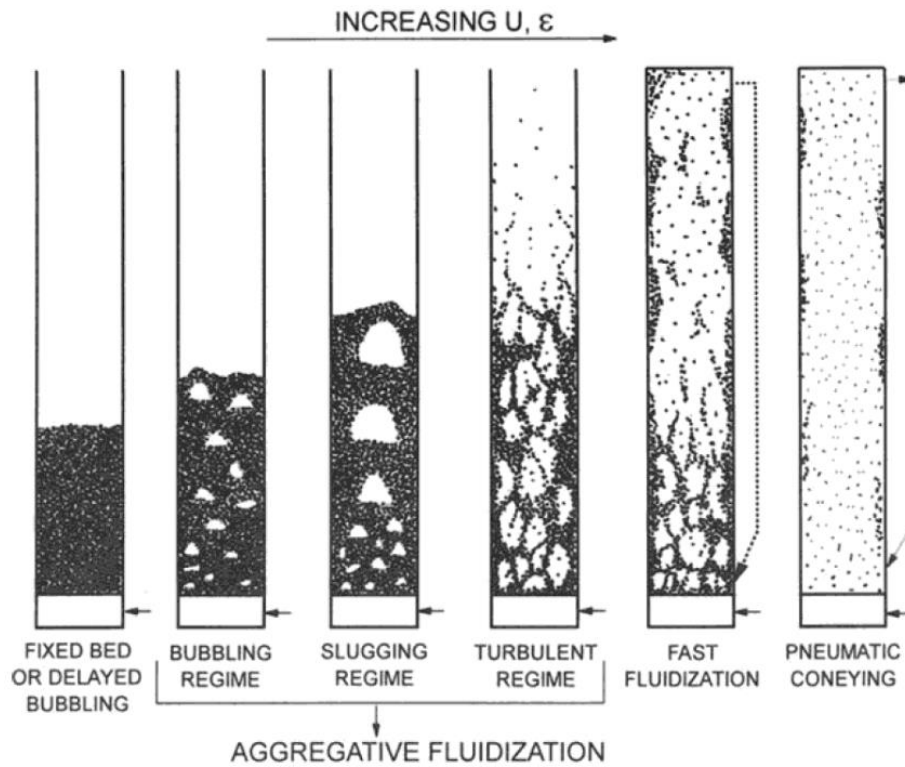


Figure 2.1 Flow regime of gas-solid fluidization [76].

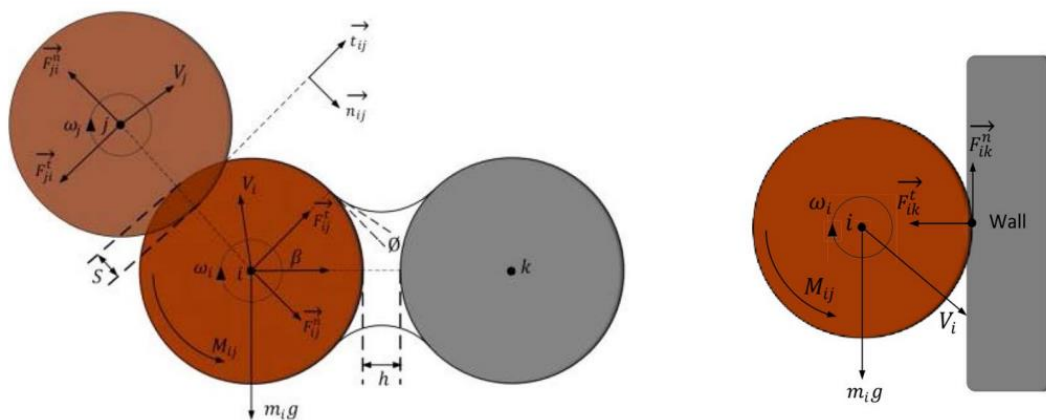


Figure 2.2 Analysis of contact forces during the collision of discrete particles considering the overlapping between particles [50].

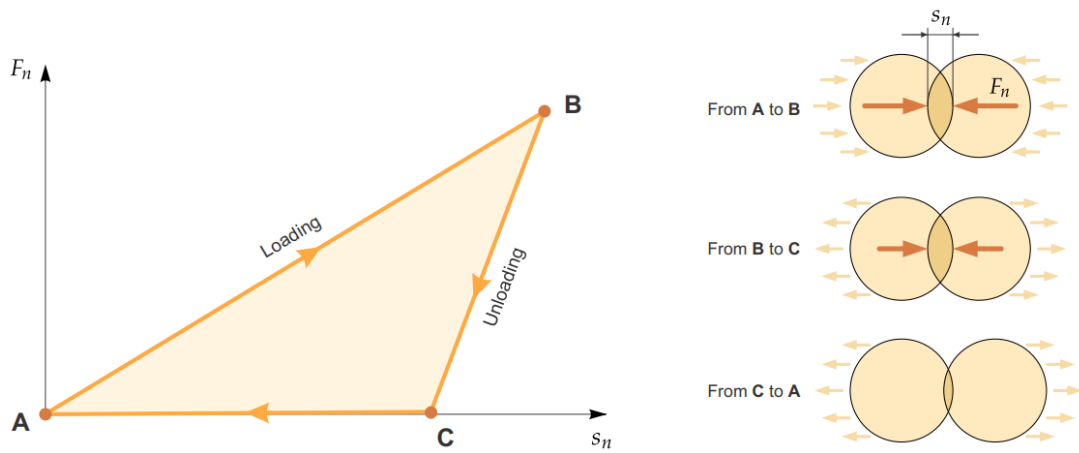


Figure 2.3 Normal force–overlap response for the hysteretic linear spring model [52].

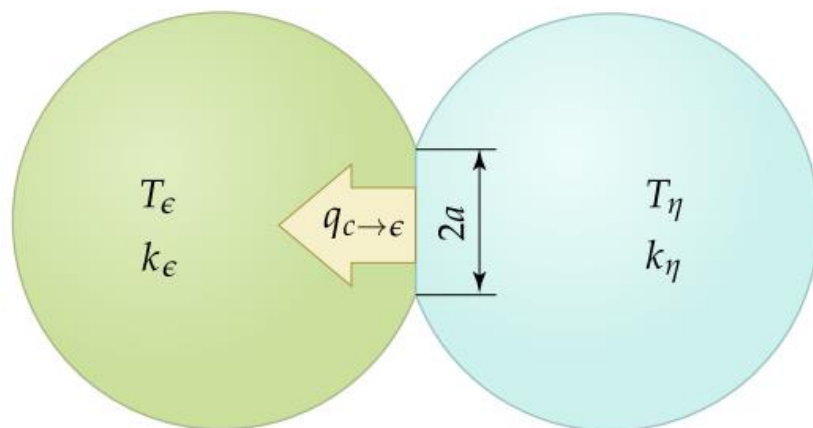
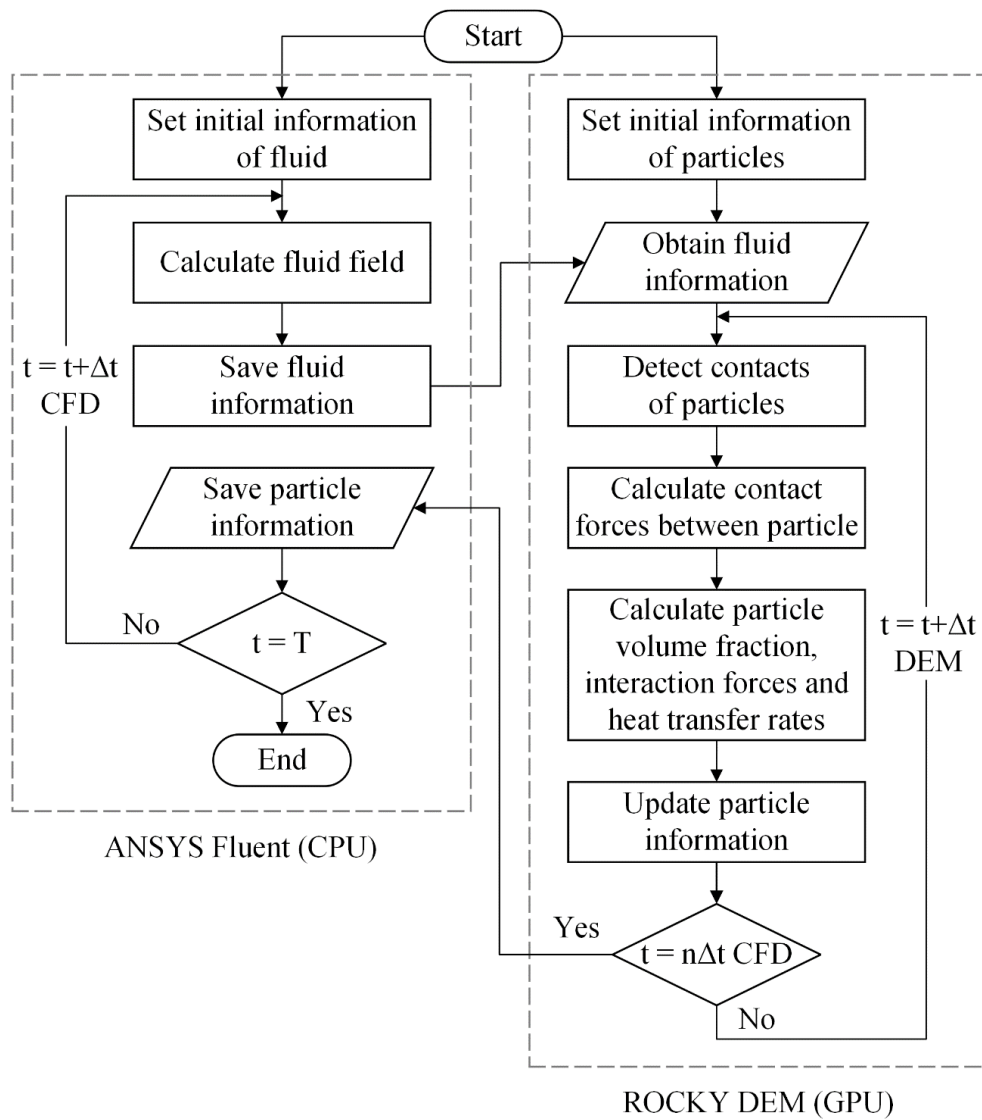


Figure 2.4 Conductive heat transfer between two colliding particles [52].



CHULALONGKORN UNIVERSITY
Figure 2.5 Flow chart of the CFD-DEM coupling approach.

CHAPTER 3

CFD-DEM MODELING OF BINARY MIXTURES OF BIOMASS AND SILICA SAND IN A BUBBLING FLUIDIZED BED

The bubbling fluidized bed combustor is a highly promising technology for biomass combustion due to its effective mixing process, efficient heat and mass transfer, and precise temperature control [77]. Typically, inert particles like spherical silica sand are added to the biomass particles in order to enhance the fluidization process, as biomass particles usually have irregular shapes [5]. While the use of inert particles improves the hydrodynamic properties of biomass particles, the mixing behavior of binary mixtures consisting of biomass and inert particles is complicated due to the significant differences in properties between the two particle types. To understand the complex hydrodynamics of mixing particles in a fluidized bed, the CFD-DEM simulation is employed. However, previous research in this area has only examined the impact of individual factors using a one-factor-at-a-time (OFAT) approach. In order to simultaneously investigate all factors, a more suitable experimental design method, such as the 2^k factorial design, is suggested. This design approach has been commonly utilized for studying complicated gas-solid systems like fluidized bed systems [78, 79].

In this chapter, the aim is to assess the mixing behavior of binary mixtures that comprised biomass and silica sand particles, representing cylindrical and spherical particles, respectively, in a fluidized bed using CFD-DEM simulation. A model was developed by utilizing an appropriate drag force model for cylindrical biomass particles and spherical silica sand particles. Additionally, the combined effects of particle size and biomass loading on the mixing behavior were examined through the

implementation of a 2^k factorial experimental design. The findings obtained from this investigation will enhance our understanding of the mixing behavior in binary particle systems and provide guidance for designing and operating other binary particle systems within fluidized beds.

3.1. Geometry, initial and boundary conditions

Figure 3.1 illustrates the 3D fluidized bed under investigation, with dimensions of 0.2 m (width), 0.03 m (depth), and 1 m (height). The CFD cell size, independent of Ma and Zhao's grid size, is set to $0.02 \times 0.02 \times 0.03$ m ($\Delta x \times \Delta y \times \Delta z$) [67]. The inlet at the bottom of the fluidized bed is set as a uniform gas velocity inlet boundary condition. At the top of the bed, a pressure outlet with atmospheric pressure is applied. For the gas phase, a no-slip boundary condition is implemented along the wall. The primary focus of this study is to investigate the impact of particle sizes and biomass particle loadings on the mixing behavior within the fluidized bed reactor. Specifically, the study considers factors including silica sand diameter (Factor A), biomass diameter (Factor B), and biomass loading (Factor C). To isolate the effect of biomass diameter on the mixing behavior, the length of the cylindrical biomass is kept fixed. The Lacey mixing index is used to evaluate the mixing behavior within the system. Table 3.1 presents the particle size and loading conditions for each case, with biomass particles being placed on top of silica sand particles in their initial packing and a total particle mass of 500 g in all cases, as shown in Figure 3.2. Furthermore, Table 3.2 summarizes the key parameters used in the simulations, which also include the properties of the silica sand and biomass particles.

3.2. Numerical model

A two-way coupling of CFD and DEM methods is employed to simulate the bubbling fluidized bed. The CFD software used for the analysis of fluid flow systems is Ansys Fluent (version 2020 R2). Additionally, the behavior of solid particles in the DEM simulation is predicted using Rocky DEM (version 4.4.2). The models setup for the particle phase involves the utilization of a linear spring-dashpot (LSD) model to calculate the contact force at particle collision points. To simulate tangential force, a Coulomb limit model is employed. In terms of the fluid phase, the Navier-Stokes equations are used to describe the continuous flow of the fluid. Various drag models have been proposed in previous studies for the coupling interphase model, considering factors like particle shape (such as spherical and non-spherical) and particle concentration (for both dilute and dense flows) [56]. However, the application of these models for non-spherical particles could lead to significant inaccuracies [77]. Therefore, the parameterized Syamlal and O'Brien model is adopted to calculate the interphase interaction between the fluid and solid particle phases. The constant parameters are adjusted for the model, differing for each particle type, depending on the fluid properties and the expected U_{mf} of the particles when applying them to spherical and rod-like particles. The phase-coupled SIMPLE algorithm is employed for pressure-velocity coupling, and the time steps for CFD and DEM are set at 2×10^{-5} and 8×10^{-7} seconds, respectively. In each case, the system is simulated until it reaches a quasi-steady-state condition.

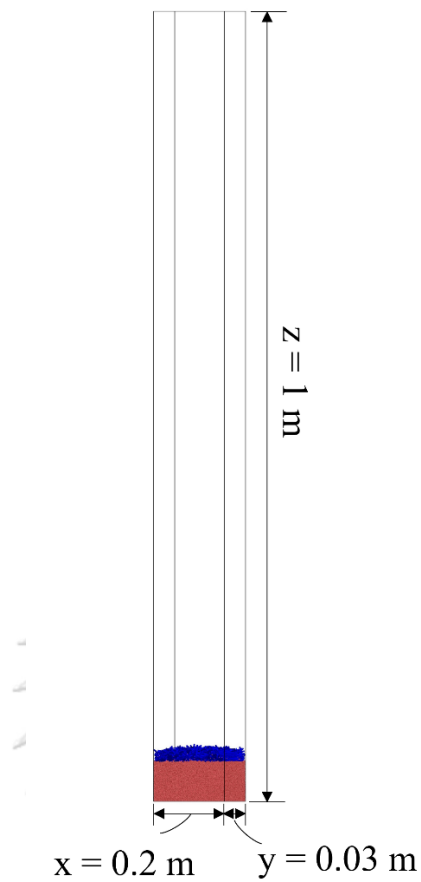


Figure 3.1 Schematic geometry of the fluidized bed.

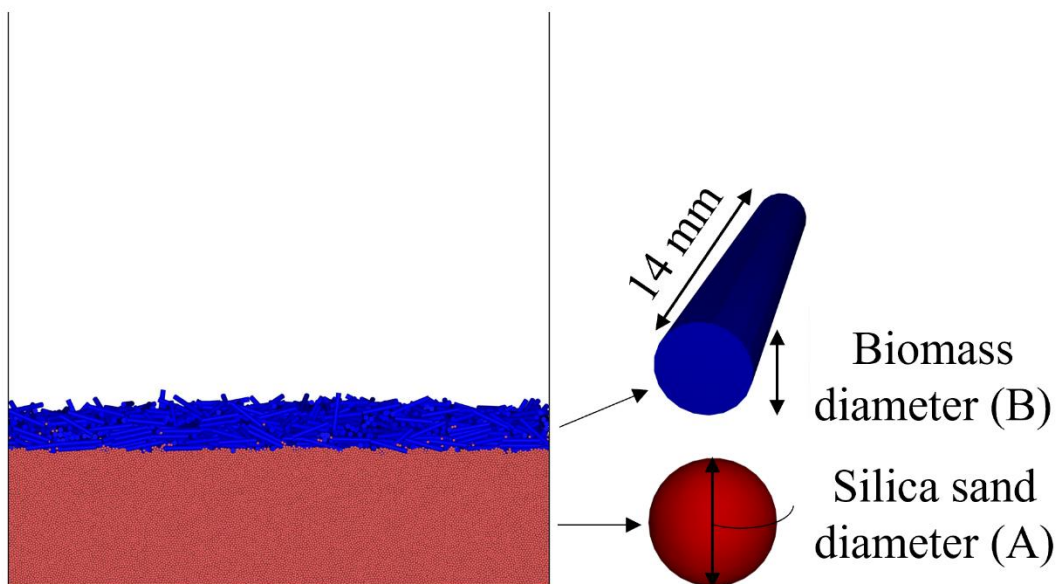


Figure 3.2 Initial packed bed with biomass and silica sand particles.

Table 3.1 Designed experiments.

Case	Silica sand diameter (mm) (A)	Biomass diameter (mm) (B)	Biomass loading (%) (C)
1	1	1.9	2.5
2	1	1.9	7.5
3	1	5.9	2.5
4	1	5.9	7.5
5	1.6	1.9	2.5
6	1.6	1.9	7.5
7	1.6	5.9	2.5
8	1.6	5.9	7.5

Table 3.2 Parameter properties used in the model.

Parameters	Value
<i>Air</i>	
Density (kg/m ³)	1.21
Viscosity (Pa·s)	1.83 × 10 ⁻⁵
Inlet velocity (m/s)	1.4
<i>Biomass</i>	
Density (kg/m ³)	764
Poisson's ratio (-)	0.3
Young's modulus (GPa)	0.1
Friction coefficient (-)	0.3
Restitution coefficient (-)	0.8
<i>Silica sand</i>	
Density (kg/m ³)	2,500
Poisson's ratio (-)	0.3
Young's modulus (GPa)	0.04
Friction coefficient	0.3
Restitution coefficient (-)	0.8

3.3. Results and discussions

3.3.1. Model validation

Figure 3.3 compares the simulation and experimental results of pressure drops at different gas superficial velocities. The results indicate that the simulation results are in good agreement with the experimental findings. At low gas velocities, the pressure drops increase gradually with an increase in gas velocity. Once the gas velocity exceeded U_{mf} , the pressure drop does not increase further and showed minimal fluctuation. The U_{mf} of biomass particles is found to be greater than that of silica sand particles, indicating that a higher superficial velocity is required to initiate fluidization when using cylindrical particles. Furthermore, a higher superficial velocity is required to break the interlocks within the particles. This phenomenon can be attributed to the voidage fraction in the static bed, which is higher for cylindrical particles than for spherical particles, thus requiring more drag force on cylindrical particles [66, 67]. Figure 3.4 illustrates the typical particle flow patterns captured in both simulations and experiments, and the results are qualitatively consistent. Although the experimental design in Table 3.1 differs from the validation cases considered in this study, the parameters specified in Table 3.2 are still used for validation purposes. These comparisons demonstrate that the current CFD-DEM model can generate reliable data for further analysis.

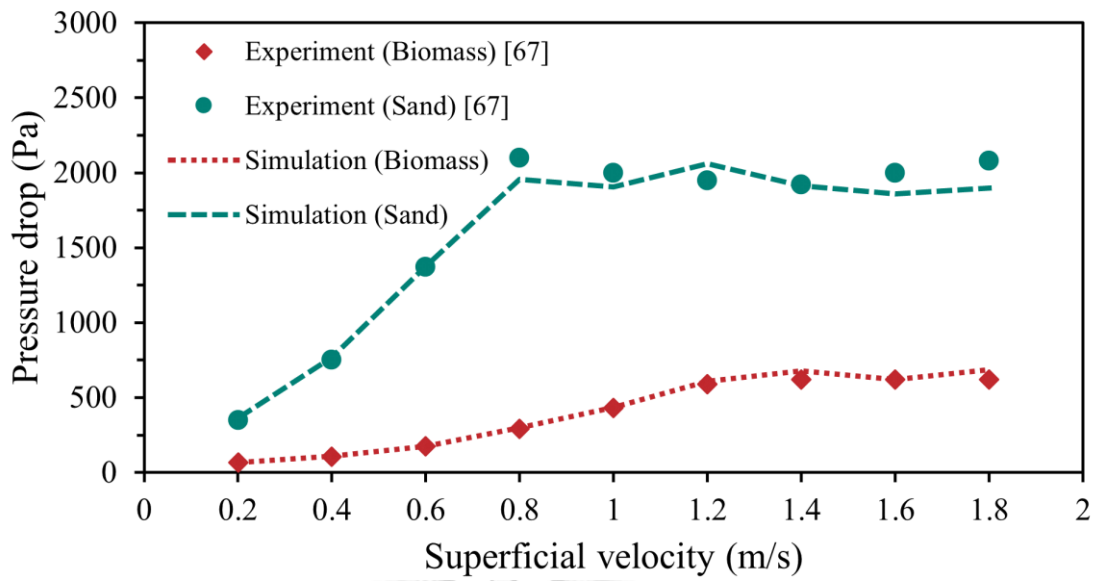


Figure 3.3 Comparison of the pressure drop between the experimental [67] and simulation results.

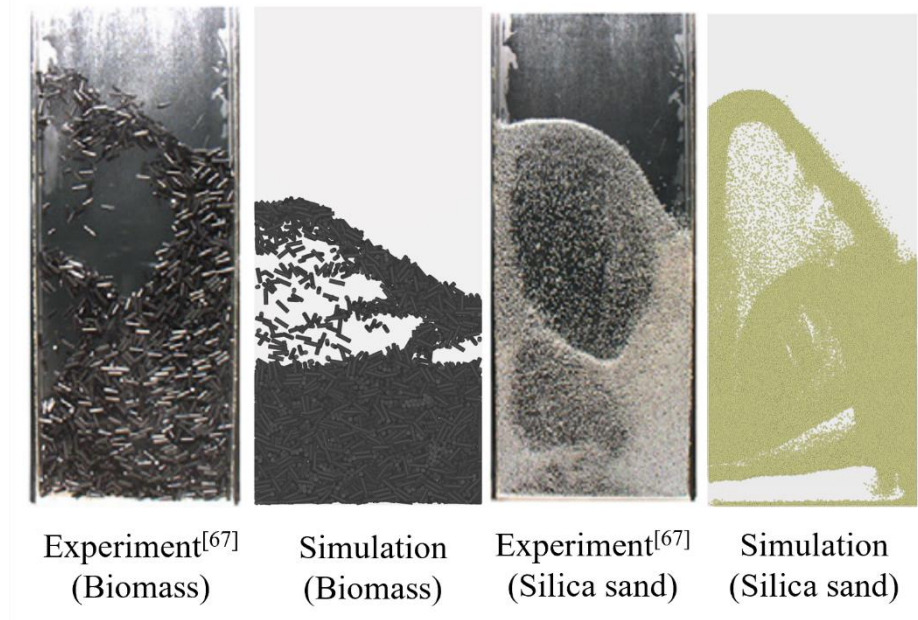


Figure 3.4 Comparison of the flow behavior between the experimental [67] and simulation results.

3.3.2. Time independency test

The time independence of the simulation is determined by examining the time at which the system attains a quasi-steady-state condition. The Lacey mixing index, which ranges from 0 to 1, is used to measure the mixing quality during the initial 5 seconds of simulation, as shown in Figure 3.5. When the system is completely separated, the mixing index is 0, whereas it is 1 when the mixture is perfectly mixed. The mixing index can approach a value close to 1, suggesting that the two particles are well mixed [80]. In this study, the example of mixing index for Case 4, which is shown in the figure, fluctuates around a certain value, implying that the system reaches a quasi-steady-state condition after 2 seconds of simulation. Consequently, the results from the last 3 seconds of each case are averaged for comparison and analysis in the following sections.

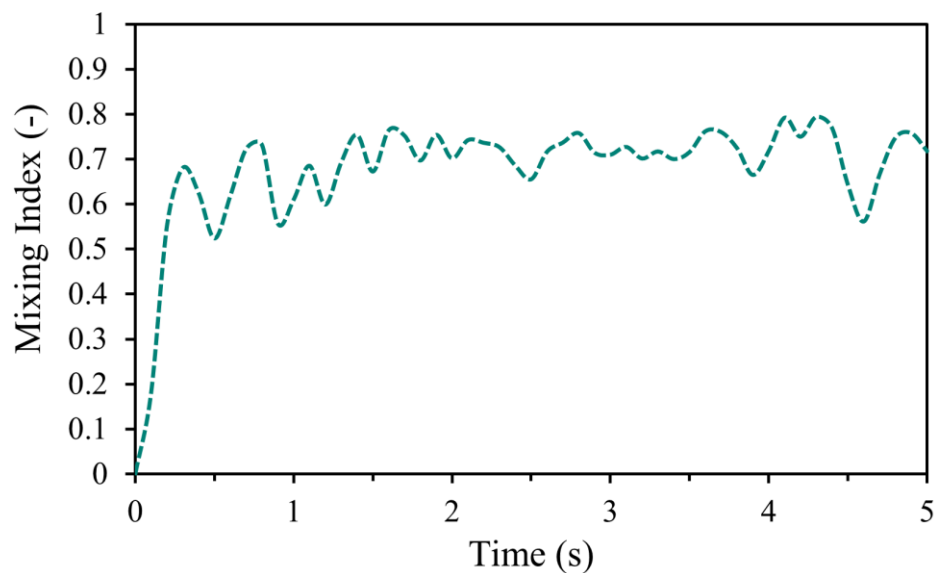


Figure 3.5 Mixing index with time (Case 4).

3.3.3. Mixing in binary particle systems

Figure 3.6 shows the average mixing index of the fluidized bed for different particle sizes and loadings in each case, as per Table 3.1. The results reveal that Case 2, which comprised a silica sand diameter of 1 mm, a biomass diameter of 1.9 mm, and a biomass loading of 7.5%, achieves the highest average mixing index at around 0.9. When compared with cases having the same biomass diameter and loading, the average mixing index for 1 mm silica sand particle is higher than that for 1.6 mm silica sand particle. Moreover, in cases having a silica sand diameter of 1 mm (Cases 1-4), the mixing index increases with an increase in biomass loading and decreased with an increase in biomass diameter. However, in cases having a silica sand diameter of 1.6 mm (Cases 5-8), the mixing index decreases with an increase in both biomass diameter and loading. These observations highlight the importance of selecting the size of inert particles based on their mixing behavior in fluidization systems. Additionally, the comparisons between Cases 5, 7, and Cases 6, 8 confirm the findings of Wang et al. [81], suggesting that even a slight difference in particle size between silica sand and biomass particles can lead to improved mixing. Furthermore, the average mixing index of the 1.9 mm biomass particle is higher than that of the 5.9 mm biomass particle, emphasizing the significance of selecting the appropriate size of biomass particles. Wang et al. showed that the size difference of biomass particles could impact the mixing index, with smaller particles exhibiting higher mixing indices. Thus, it is crucial to select the size of biomass particles through sieving to ensure proper system hydrodynamics. Moreover, different biomass particle loadings result in varying volumes of silica sand particles and lead to a slightly different trend in mixing behavior.

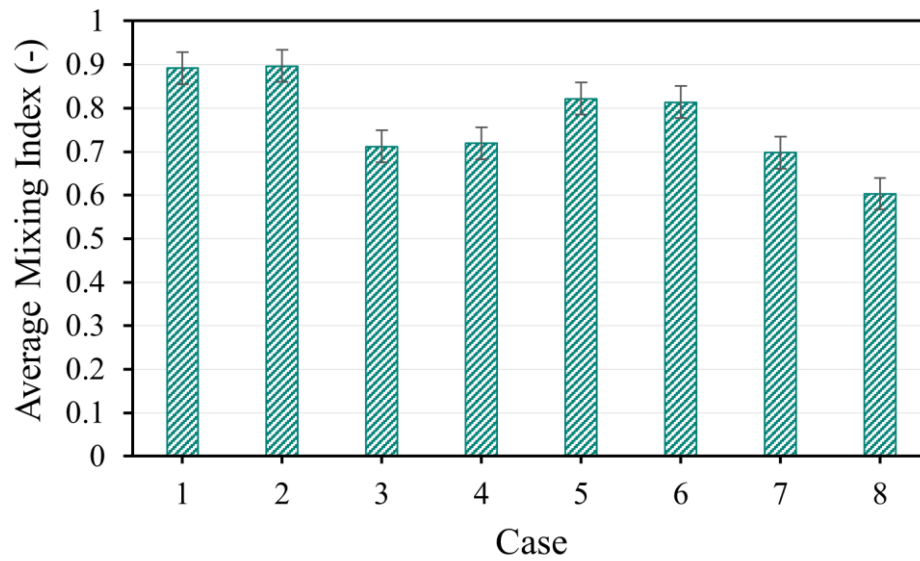


Figure 3.6 The average mixing index with different particle sizes and loadings.

The effect estimates of the factors on the average mixing index as the response variable are summarized in Table 3.3. The biomass diameter (B) has the most significant effect on the mixing behavior, followed by the silica sand diameter (A), whereas the biomass loading (C) has the least significant effect. Moreover, the contribution of the interactions between the parameters is approximately two percent, indicating their low significant effect. These results support the earlier explanation that the biomass diameter has the most prominent influence on the mixing behavior of the binary mixture system. Additionally, the comparison of cases with different particle loading emphasizes the importance of incorporating inert particles to enhance the hydrodynamic properties of biomass particles, including their mixing behavior in binary mixture systems.

Table 3.3 Factor effect estimates for response: Average mixing index.

Parameters	SS	DF	MS	% Contribution
A	0.01	1	0.01	13.39
B	0.06	1	0.06	80.32
C	0.001	1	0.001	1.34
AB	0.0001	1	0.0001	0.13
AC	0.0016	1	0.0016	2.14
BC	0.0009	1	0.0009	1.2
ABC	0.001	1	0.001	1.34
Total	0.0747	7		100

3.4. Conclusion

In this chapter, the CFD-DEM model is developed using a two-way coupling approach for cylindrical biomass and spherical silica sand particles, with an appropriate drag force model utilizing the parameterized Syamlal & O'Brien drag force model. The 2^k factorial experimental design is employed to investigate the effect of silica sand and biomass particle sizes, as well as biomass loading, on mixing behavior in terms of the average mixing index, as evaluated by the Lacey mixing index. The main factor affecting the average mixing index is found to be the biomass diameter, while the silica sand diameter also has a significant impact. The biomass loading and interaction of parameters have only a slight effect on the average mixing index. The use of smaller silica sand and biomass diameters results in a higher

average mixing index, even with an increase in biomass loading. Therefore, smaller biomass sizes might be considered for use in the fluidization of binary mixture systems. This study of different biomass sizes could be used as a guide in selecting the appropriate biomass size for obtaining the desired system hydrodynamics in real operations. In addition, silica sand as an inert bed material could be added to aid in the fluidization of non-spherical biomass particles. In future studies, the integration of a thermal model into the developed CFD-DEM model could enable the investigation of heat transfer within the system, potentially applicable to the bubbling fluidized bed combustor operation.



CHAPTER 4

NUMERICAL SIMULATION OF MIXED BIOMASS AND SILICA SAND PARTICLES IN A BUBBLING FLUIDIZED BED COMBUSTOR

The fluidization behavior of the biomass and silica sand mixture is complex due to the substantial differences in physical properties such as density, size, and shape between these two components. These differences give rise to complexities in the mixing behavior and heat transfer among the particles involved [82]. Moreover, the size and shape of the biomass further contribute to the hydrodynamic behaviors of the system, such as the minimum velocity required for fluidization [83, 84], expanded bed fluctuation, mixing, and segregation [85-87]. Considering the shape and size distribution of biomass is important for comprehending the potential phenomena in real systems. It is crucial not to make assumptions or overlook these factors, as doing so can result in a lack of understanding and significant errors. In addition, mixtures containing different components frequently display a vertical nonuniform distribution. This occurs because biomass, being generally larger and less dense than silica sand, tends to migrate towards the bed's surface, leading to segregation from the silica sand. Furthermore, adding of excessive amounts of biomass into the system can compromise the quality of fluidization [87, 88]. Therefore, it is essential to investigate the impact of the optimal biomass loading in the mixture on the mixing behavior and heat transfer within the bubbling fluidized bed combustor. These factors are closely related to the design, operation, and optimization of the fluidized bed combustor.

Previous research has indicated the complexity of fluidizing non-spherical particles, as particle shape plays a significant role in the hydrodynamic characteristics

and heat transfer within fluidized beds. However, there has been limited investigation into the fluidization behavior of mixed biomass, particularly when considering two different biomass types with varying particle size distributions, and how different blending ratios and loadings affect the mixing behavior and heat transfer. Consequently, this chapter aims to evaluate the impact of utilizing different biomass types, loadings, and blending ratios on the mixing behavior and heat transfer within the bubbling fluidized bed combustor. The selected biomass particles are cylindrical in shape with different aspect ratios, while the silica sand particles are spherical. The study thoroughly examines the solid flow patterns, mixing efficiency, heat transfer rate, as well as the contact forces between particles and the fluid.

4.1. Geometry, initial and boundary conditions

In this chapter, a laboratory-scale bubbling fluidized bed combustor is simulated, with dimensions of 0.2 m in width, 0.03 m in depth, and 1 m in height, as illustrated in Figure 4.1. The simulation utilizes 3D Computational Fluid Dynamics (CFD) and 3D Discrete Element Method (DEM), which have been successfully employed in previous studies [67, 89]. The CFD grid is set up with dimensions of 15, 1, and 50 in the x, y, and z directions. This grid size, as depicted in Figure 4.2, is deemed suitable and has been used in previous research [67, 89]. It is larger than the size of sand particles, which constitute the majority of particles in the system, and also fulfill the algorithm requirements of the CFD-DEM method [90]. The depth of the bubbling fluidized bed is approximately twice the length of BG1 particle. This ratio is chosen to ensure computational efficiency of the CFD-DEM simulation. The

efficiency is constrained by the need to track each particle and accurately resolve inter-particle collisions [91].

During the initial packing, a mixture of silica sand and biomass particles is used, with a total particle mass of 400 g and an initial temperature of 30 °C. The silica sand particles are randomly generated at the bottom of the fluidized bed, with the mass varying based on the biomass loading in each case studied. These particles then freely fall and pack to achieve a predetermined initial bed height. Following this, biomass particles are introduced by falling from a specific height under gravity. Each cylindrical biomass particle has random velocities and orientations, determined using the poured packing method [92]. It is important to note that the wood chip particles are positioned on top of all the particles, followed by bagasse particles of various sizes (BG1-BG4). These biomass particles are located on the silica sand, as shown in Figure 4.3, depicting the example of using wood chip, BG1 and BG2 with silica sand. The settling process continues until the velocities of all particles approach zero. Air is introduced into the fluidized bed through a bottom inlet at a uniform velocity of 1.8 m/s and a temperature of 488 °C. This temperature value represents the average air temperature at steady state after biomass combustion, as determined in a study investigating the combustion characteristics of various biomasses in a bubbling fluidized bed combustor [93]. However, with the addition of the temperature model in the system, the U_{mf} of the particles, as shown in Figure 3.3, may change, leading to the possibility that the air velocity in the system is not necessarily equal to 1.8 m/s. The decrease in air velocity flow through the system with increasing temperature can be attributed to the change in U_{mf} . As the temperature rises, the gas molecules undergo thermal expansion, resulting in a decrease in gas density. Since U_{mf} is inversely

proportional to gas density, the decrease in density leads to a decrease in U_{mf} [94]. Consequently, a lower air velocity is required to maintain fluidization at higher temperatures. However, for the purpose of investigating the effect of different operational parameters solely on the particles, the inlet boundary conditions are set to be the same as those used in Chapter 3. The outlet pressure is set at 101,325 Pa, and the walls of the system are assigned a no-slip boundary condition and considered adiabatic. Regarding collisions between particles and the side walls, the walls are treated as particles with an infinite diameter. Table 4.1 provides an overview of the physical properties and operational parameters employed in this study.

The particles use in this chapter consisted of spherical silica sand, wood chips, and sugarcane bagasse, with their characteristics summarized in Table 4.1. The dimensions of wood chips were obtained from Integrated Research Center Company Limited (IRC), a company that uses fine wood chips as the primary fuel source in fluidized bed boilers for electricity generation in Thailand. The wood chips have a rectangular shape with average dimensions of 20 x 20 mm² in length and width, and a thickness of 5 mm. However, in the fluidized bed combustion process, wood chips are commonly used in the form of wood pellets, which are produced by compressing wood chips. Wood pellets offer several advantages for combustion, including consistent size, higher energy density, and improved handling and storage capabilities. Their uniform shape and size make them well-suited for efficient combustion and reliable performance in fluidized bed combustion systems [95]. Furthermore, the individual shape of the wood particles was observed, and it was found that approximately half of the samples exhibited a cylindrical shape [96]. Consequently, in this study, the wood chips are chosen to have a cylindrical shape, except for the

properties of Young's Modulus and Poisson's ratio, which provided by IRC. Cylindrical wood chips have the same volume as rectangular wood chips, with a cylindrical length equal to the thickness of the rectangular chips. Thus, the wood chips in this study have a diameter of 4.37 mm and a length of 5 mm. Bagasse is chosen as an alternative biomass to be mixed with wood chips in order to address the issues of biomass shortage during certain seasons and low thermal efficiency when using a single type of biomass [97]. Information regarding the size and shape of bagasse particles is obtained from previous literature that focused on studying the geometrical characteristics of bagasse as a fuel in fluidized beds [69]. The large bagasse particles, characterized by a high height-width ratio and diameter, are modeled as cylinders. Thus, both types of biomasses (wood chips and bagasse) are represented as cylindrical particles in this study. Furthermore, to investigate the influence of particle size distribution on fluidization behavior, the bagasse particles are categorized into four groups: BG1, BG2, BG3, and BG4, each with varying diameters and lengths, expressed in terms of aspect ratio. These sizes are determined through granulometric analysis [69]. Additionally, for the silica sand particles, two different sizes (1 mm and 1.6 mm) are used to examine the impact of inert particle size on fluidization behavior. It is important to note that the physical and thermal properties of the particles listed in Table 4.1 are obtained from previous literatures [67, 69, 98-101].

In order to examine the impact of different ratios and loadings of mixed biomasses on mixing behavior and heat transfer, the study conducts 17 cases with varying biomass types, loadings, and blending ratios of wood chips and bagasse, as outlined in Table 4.2. The bagasse is categorized into coarse, fine, and all bagasse sizes based on granulometric analysis, allowing for an investigation into the effect of

particle size distribution, specifically the aspect ratio [69]. Table 4.3 provides the specific details of the bagasse sizes in each type. After evaluating the results of using a single type of biomass, the remaining cases involve mixed biomasses comprising wood chips and bagasse, with varying biomass loadings and blending ratios. Based on the analysis of optimal mixing behavior, one of the three bagasse types (coarse, fine, and all size) would be selected to mix with wood chips. In all the case studies, which included both biomass and silica sand, the total particle mass is kept constant at 400 g. The quantity of each component is determined based on the biomass loading and blending ratio, as indicated in Tables 4.2 and 4.3.

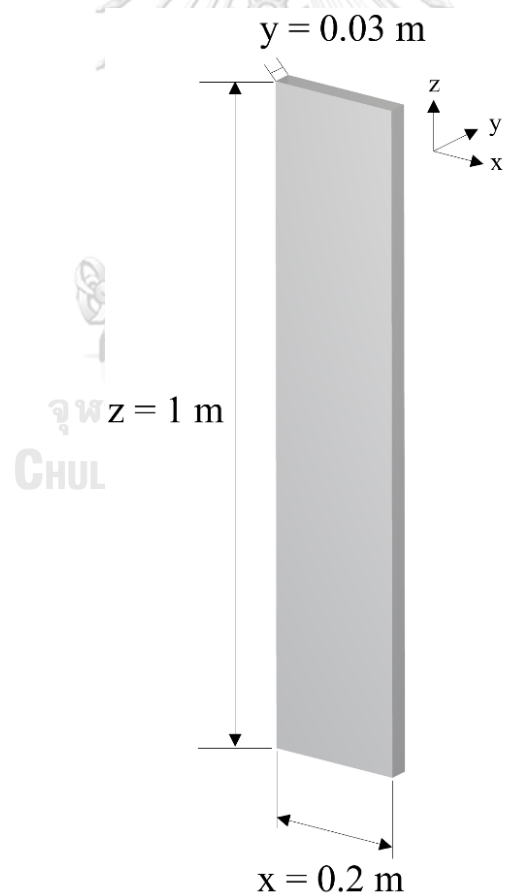


Figure 4.1 Dimensions of the fluidized bed combustor used in this study.

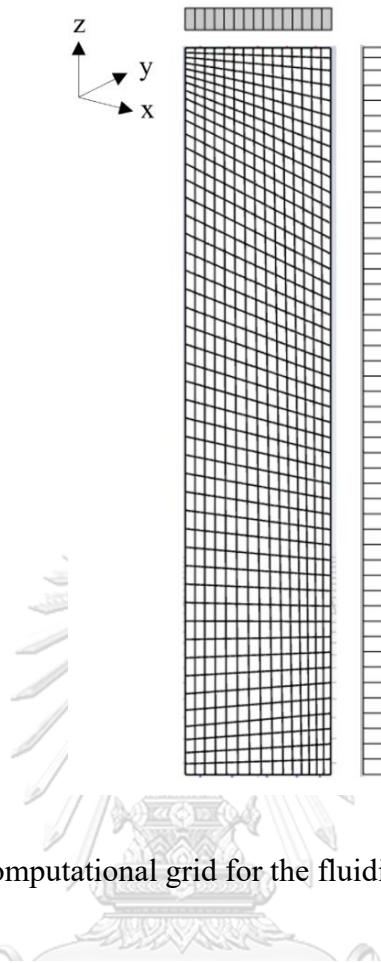


Figure 4.2 Computational grid for the fluidized bed combustor.

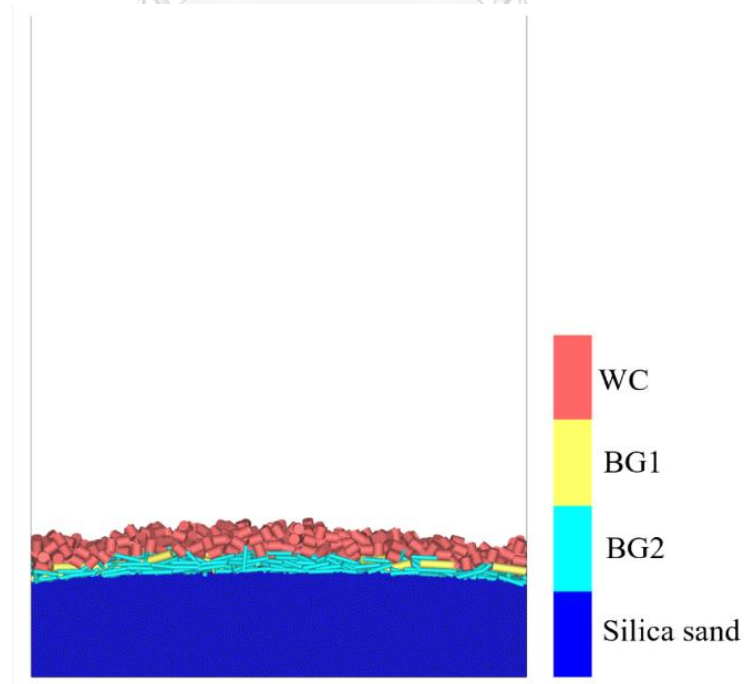


Figure 4.3 Initial packed bed of mixed biomass and silica sand (Case 9).

Table 4.1 Physical properties and operational parameters employed in this study.







<i>Particle phase</i>						
						
Particle	Wood chip (WC)	Bagasse 1 (BG1)	Bagasse 2 (BG2)	Bagasse 3 (BG3)	Bagasse 4 (BG4)	Silica Sand
Diameter (d), mm	4.37	3.555	1.77	0.885	0.507	1, 1.6
Length (L), mm	5	13.5	10.33	7.81	3.52	-
Aspect ratio (L/d), -	1.1	3.8	5.84	8.8	6.9	-
Equivalent diameter (d_{eq}), mm	4.57	5.55	3.19	1.83	0.97	1, 1.6
Density (ρ_p), kg/m ³	307.7	478.6	483.3	520	555	2,650
Young's Modulus (E), GPa	0.003	1	1	1	1	2
Poisson's ratio (ν), -	0.37	0.37	0.37	0.37	0.37	3
Thermal conductivity (k_p), W/(m·K)	0.0646	0.1	0.1	0.1	0.1	0.84
Specific heat ($c_{p,p}$), J/(kg·K)	840	1.76	1.76	1.76	1.76	860

Table 4.1 Continue

Initial particle temperature (T_p), °C	30
Initial particle loading, kg	0.4
Restitution coefficient:	
Biomass-Biomass (ϵ_{b-b}), –	0.5
Biomass-Sand (ϵ_{b-s}), –	0.9
Sand-Sand (ϵ_{s-s}), –	0.9
Biomass-Wall (ϵ_{b-w}), –	0.5
Sand-Wall (ϵ_{s-w}), –	0.9
Static and Dynamic friction coefficient:	
Biomass-Biomass ($\mu_s, \mu_d, b-b$), –	0.4
Biomass-Sand ($\mu_s, \mu_d, b-s$), –	0.3
Sand-Sand ($\mu_s, \mu_d, s-s$), –	0.3
Biomass-Wall ($\mu_s, \mu_d, b-w$), –	0.4
Sand-Wall ($\mu_s, \mu_d, s-w$), –	0.3
Time step (Δt), s	2×10^{-5}
<i>Fluid phase</i>	
Density (ρ_f), kg/m ³	0.464
Viscosity (μ_f), kg/(m·s)	3.53×10^{-5}
Thermal conductivity (k_f), W/(m·K)	0.055
Specific heat ($c_{p,f}$), J/(kg·K)	1090.12
Inlet velocity (u_f), m/s	1.8
Inlet temperature (T_f), °C	488
Size of CFD cells	
Δx , m	0.0133
Δy , m	0.03
Δz , m	0.02
Time step, (Δt), s	1×10^{-4} s

Table 4.2 Simulation conditions of each study case.

Case no.	Biomass type	Biomass loading (% by weight)	Blending ratio (Wood chip: Bagasse)
1	Wood chip	5	-
2	Wood chip	2.5	-
3	Wood chip	7.5	-
4	Coarse bagasse (BG1+BG2)	5	-
5	Fine bagasse (BG3+BG4)	5	-
6	All bagasse (BG1+BG2+BG3+BG4)	5	-
7	All bagasse (BG1+BG2+BG3+BG4)	2.5	-
8	All bagasse (BG1+BG2+BG3+BG4)	7.5	-
9	Mixed biomass	5	1:1
10	Mixed biomass	5	3:1
11	Mixed biomass	5	1:3
12	Mixed biomass	2.5	1:1
13	Mixed biomass	2.5	3:1
14	Mixed biomass	2.5	1:3
15	Mixed biomass	7.5	1:1
16	Mixed biomass	7.5	3:1
17	Mixed biomass	7.5	1:3

Table 4.3 Component of bagasse sizes in each type.

Particle	Perez et al. [69]	Coarse bagasse	Fine bagasse	All bagasse
	Mass (%)	Mass (%)	Mass (%)	Mass (%)
BG1	7.7	40.53	-	15.75
BG2	11.3	59.47	-	23.11
BG3	9.5	-	31.77	19.43
BG4	20.4	-	68.23	41.72
Total	48.9	100	100	100

4.2. Numerical model

The numerical models for the two-way coupling approach of CFD-DEM are described in section 2.3. In summary, at each time step, the CFD simulation calculates the fluid flow field and provides the relevant information. The DEM simulation then utilizes this information to determine the forces, positions, velocities, and heat transfer rates of individual particles, enabling the evaluation of porosity, volumetric particle-fluid forces, and energies within a computational cell. The CFD simulation subsequently incorporates these details to calculate the fluid flow field for the next time step. This information is then utilized to determine the particle-fluid forces acting on individual particles, resulting in the determination of new positions and velocities of the solids for the subsequent time step [56]. The time step for the CFD simulation is set to 1×10^{-4} s, while for the DEM simulation, it is set to 2×10^{-5} s. The total simulation time for each case is 30 s. It is observed that the mixing index of silica sand and biomass reaches a relatively steady state after 5 s, and the time-averaged results are obtained based on data collected between 5 and 30 s. To quantify the mixing quality of a mixture, the mixing index is used. The validity of the present CFD-DEM model is confirmed by comparing its results with experimental data obtained from the study conducted by Ma and Zhao [67], studied as discussed in section 3.3.1.

Various techniques have been suggested in literature to quantify the degree of mixing in fluidized beds [102]. In this study, the Lacey mixing index [103] is employed due to its ability to evaluate the mixing quality of particles with different sizes without the need to include the size parameter in the equations [104]. The Lacey mixing index is expressed as follows:

$$M = (S_0^2 - S^2) / (S_0^2 - S_R^2) \quad (36)$$

$$S_0^2 = p \times q, \quad S_R^2 = \frac{(p \times q)}{N}, \quad \frac{1}{n-1} \sum_{i=1}^n (p_i - p)^2 \quad (37)$$

where S^2 is the actual variance, S_0^2 and S_R^2 are the variances of the completely segregated and well-mixed states, respectively. Here, p and q are the volume fractions of spheres and biomasses in a mixture, p_i is volume fraction of sphere in each cell, N is the average number of particles in each cell, and n is the number of cells.

4.3. Results and discussions

4.3.1. Flow pattern and mixing characteristics of single biomass mixture

Figure 4.4 illustrates the patterns of particle flow for binary mixtures consisting of silica sand and a single biomass type over time. When gas enters the bed from the bottom, bed expansion and the formation of large-size bubbles occur due to the introduced gas flow, carrying a significant number of particles upward. In all cases of biomass types, it can be observed that biomass particles predominantly distribute in the surface region of the bed, behaving more like the flotsam. On the other hand, silica sand segregates and locates at the bottom of the bed [100, 105]. The formation of large bubbles in the middle of the bed leads to the separation between silica sand and biomass particles, which is unfavorable for achieving uniform biomass distribution. Over time, the segregation between the two components becomes more noticeably, except for the case of coarse bagasse (Figure 4.4(b)). In Figure 4.4(a), wood chip particles primarily distribute on the top surface of the silica sand, with limited penetration of silica sand into the wood chip. This results in a partially mixed region at the surface. In Figure 4.4(b), the two particle types exhibit a tendency to

mix, with some BG2 particles moving downward towards the middle region. The particles in the middle region are entrained by bubbles and rise until the bubbles burst. Furthermore, due to the influence of bubble behavior, the particle concentration near the wall is significantly higher compared to the middle region. Subsequently, the particles tend to relocate to the middle region and are carried upward by the bubbles. These characteristic behaviors of bubbles and particles contribute to an improvement in the mixing property [91]. Besides, some silica sand particles can penetrate the BG1 and BG2 particles, resulting in a higher degree of mixing compared to other cases. According to Figure 4.4(c), it can be observed that the fine bagasse particles, including BG3 and BG4, expand significantly, while silica sand predominantly occupies the bottom region. Due to the low operational gas velocity, silica sand particles are unable to move upward towards the fine bagasse region and mix with it. Moreover, due to the large drag force acting on the particles, the fine bagasse particles become attached and tend to move upward together towards the freeboard. Consequently, a distinct interface forms between the two layers, effectively segregating the two particle types and leading to nonuniform temperature distribution and localized vapor production [106]. Lastly, in Figure 4.4(d), similar to the observations in Figures 4.4(a) and (b), some coarse bagasse particles exhibit a tendency to mix with silica sand in the middle region due to the influence of bubble behaviors. However, all fine bagasse particles expand significantly and do not partially mix with the coarse bagasse and silica sand particles. As a result, when using fine biomass particles, a higher gas velocity is required to break the strong inter-particle force between the fine particles and to drag the silica sand towards the fine biomass [83]. Comparatively, the strong restriction of solid motion in the bottom

region leads to better mixing performance in the middle region of the binary mixture system within the bubbling fluidized bed.

However, despite the observations mentioned earlier, a good mixing state between small and large cylindrical biomass particles, and silica sand is not achieved. To provide a clearer understanding of the results presented in Figure 4.4, the equivalent spherical diameter is provided in Table 4.1 to compare the differences in particle sizes between cylindrical and spherical particles. The equivalent diameter is calculated using $d_{eq} = (L \times d^2)^{1/3}$, where L represents the cylindrical length and d represents the cylindrical diameter [107]. It can be observed that when there are small differences in the equivalent sizes of biomass and silica sand, the good mixing qualities are not observed, as shown in Figure 4.4(c). These observations are in contrast to the findings suggesting that with a narrower particle size distribution exhibit better mixing behavior [108]. However, it should be noted that the use of cylindrical biomass particles in the current study may lead to different results. Additionally, despite BG1 having a larger equivalent size than wood chip in Figures 4.4(a) and (b), the use of coarse bagasse improves the mixing quality. This indicates that BG2 contributes to the mixing of BG1 and silica sand, leading to better mixing behavior and emphasizing the significance of particle size distribution in the system. On the other hand, the inclusion of coarse bagasse size does not notably enhance the mixing behavior when using all bagasse, as illustrated in Figure 4.4(d).

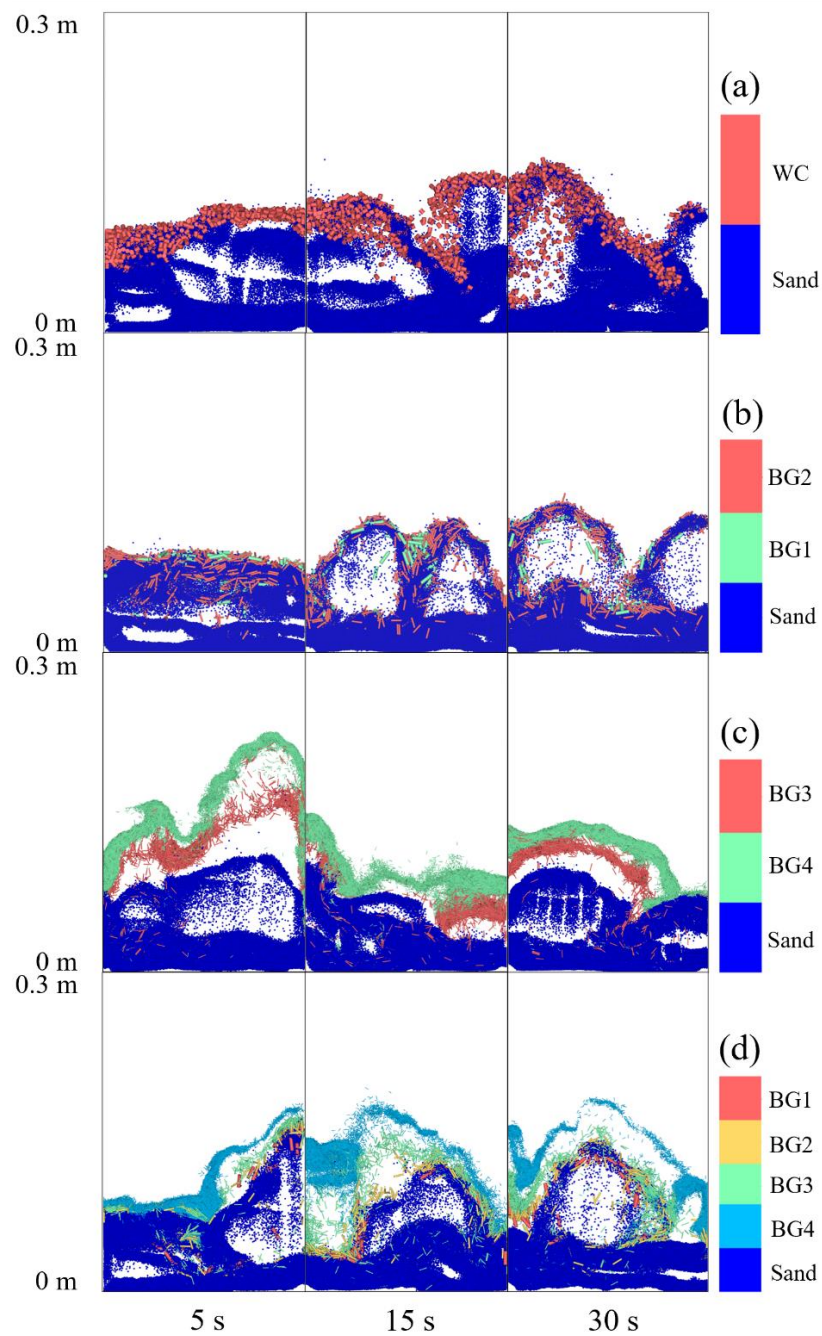


Figure 4.4 Flow patterns for the mixture of silica sand and (a) wood chip, (b) coarse bagasse, (c) fine bagasse and (d) all bagasse.

The mixing behavior of binary mixtures consisting of silica sand and a single biomass is further analyzed by examining the plots and contours depicting the time-averaged axial distribution of the volume fraction of particles, as shown in Figure 4.5.

The findings from the solid configuration snapshot in Figure 4.4 support the observation that biomass particles tend to accumulate at the top of the bed, while silica sand particles predominantly occupy the bottom region. This trend is consistent with the volume fraction plots presented in all the figures. In Figure 4.5(a), it can be observed that wood chip particles exhibit higher fractions on the top surface of the silica sand, indicating partial mixing. Figure 4.5(b) confirms that silica sand and coarse bagasse have high fractions at similar heights, indicating a higher degree of mixing compared to the other cases. Conversely, Figures 4.5(c) and (d) reveal that at heights where the biomass fractions are predominantly high, the fractions of silica sand are relatively low. According to Table 4.3, some BG1 and BG2 particles mix with silica sand, but their mass content is considerably lower compared to BG3 and BG4. Consequently, the use of fine bagasse in this study often leads to segregation rather than achieving a desirable mixing state.

In order to investigate the impact of particle size distribution on the flow pattern of binary mixtures, Figure 4.6(a) presents a comparison of the mixing index variations over time. The coarse bagasse case exhibits the highest mixing index among the different bagasse cases, as confirmed with the results from Figures 4.4 and 4.5. The mixing index value ranges from 0 to 1, where 1 indicates complete random mixing between the two particle types, and 0 signifies complete separation, according to the Lacey method. A mixing index value above 0.8 indicates a well-mixed system [81]. However, based on the results in Figure 4.6(a), a mixing index value of 0.6 indicates poor mixing between coarse bagasse and silica sand, despite achieving a stable mixing state. Comparing the fine and all bagasse cases, the mixing index of all bagasse case is slightly higher than that of the fine bagasse case, primarily due to the

inclusion of some coarse bagasse particles that mix with silica sand. This corresponds to the significant particle size difference between the biomass and silica sand particles. Nevertheless, considering the mixing index, coarse bagasse is selected to be mixed with wood chip in the subsequent study cases involving mixed biomasses mixtures. Therefore, in this study, employing biomass and silica sand particles with considerably different equivalent sizes and particle size distribution leads to improved mixing behavior, which is conducive to achieving optimal operation in binary systems of single biomass and silica sand. Moreover, when examining the impact of different biomass loadings on the mixing index in Figure 4.6(b), it is evident that increasing the biomass loading leads to a slight increase in the mixing index for both wood chip and all bagasse sizes. The increase in biomass loading results in a higher number of cylindrical particles, leading to a higher void fraction during initial packing. After fluidization, silica sand can easily penetrate the space between biomass particles, thereby promoting a slight improvement in mixing. Additionally, as the biomass loading increases, the frequency of bubbles rises in the center of the bed. A higher bubble frequency indicates a greater number of bubbles ascending through the bed with a more uniform distribution of smaller bubbles, thereby enhancing solids mixing due to sufficiently high bubbling velocities [5, 109]. However, if the system contains a significant proportion of cylindrical particles compared to spherical particles, the mixing process may be inhibited, resulting in a lower mixing index. This is particularly relevant for low gas velocities close to $1.5 U_{mf}$ [110]. Consequently, when operating a fluidized bed involving biomass, it is crucial to carefully consider the appropriate biomass loading to ensure proper fluidization behavior within the system.

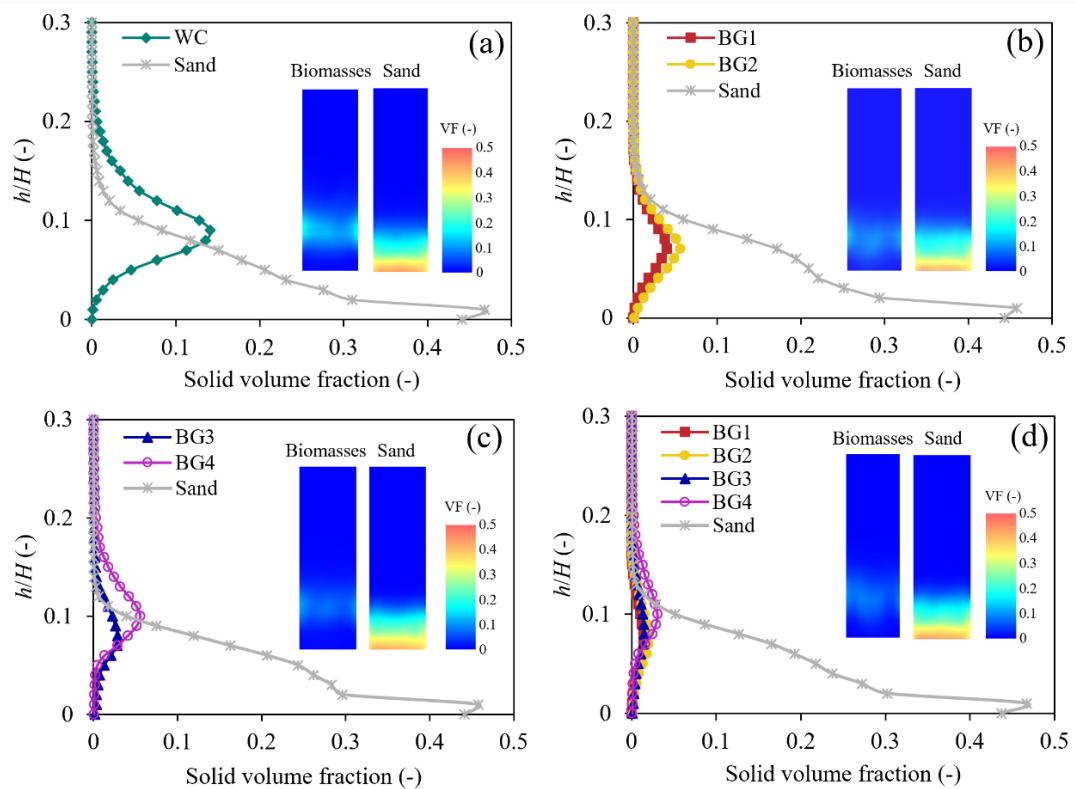


Figure 4.5 Time-averaged solid volume fraction of particles along the bed height for the mixture of silica sand and (a) wood chip, (b) coarse bagasse, (c) fine bagasse and (d) all bagasse.

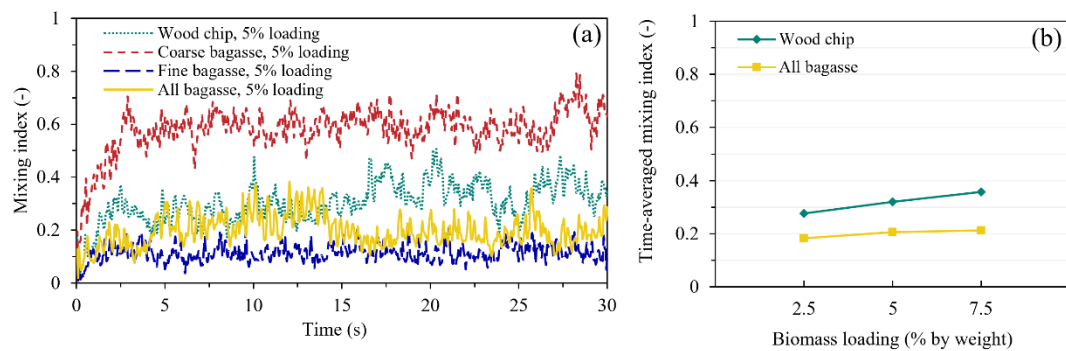


Figure 4.6 (a) Mixing index with time and (b) comparison of the time-averaged mixing indexes with the change of biomass loading for different mixtures.

4.3.2. Flow pattern and mixing characteristics of mixed biomass mixture

Figures 4.7(a)-(c) illustrate the particle flow patterns over time for binary mixtures of silica sand and mixed biomass. Similar to the behavior observed in single biomass mixtures, silica sand could penetrate BG1 and BG2 particles but not wood chips, leading to the mixing of biomass with silica sand at the surface across all blending ratios. Although the influence of bubbles initially causes particles to be carried upwards, but the formation of large bubbles at the bottom of the bed results in the separation of silica sand and biomass particles, with the particles accumulating at the surface as the system reaches a dynamic equilibrium of mixing. However, due to differences in aspect ratio and equivalent diameter, some BG1 and BG2 particles can penetrate the wood chips, assisting the mixing of different biomass types with varying aspect ratios, highlighting the importance of particle size distribution. Nonetheless, the mixing of wood chips and silica sand is only partially mixed, and having an excessive amount of wood chips in comparison to coarse bagasse can lead to the accumulation of biomass particles on the surface of the silica sand, as depicted in Figures 4.7(a) and (b). Therefore, a blending ratio of 1:3 (wood chip to coarse bagasse) appears to exhibit better mixing compared to other ratios, as shown in Figure 4.7(c).

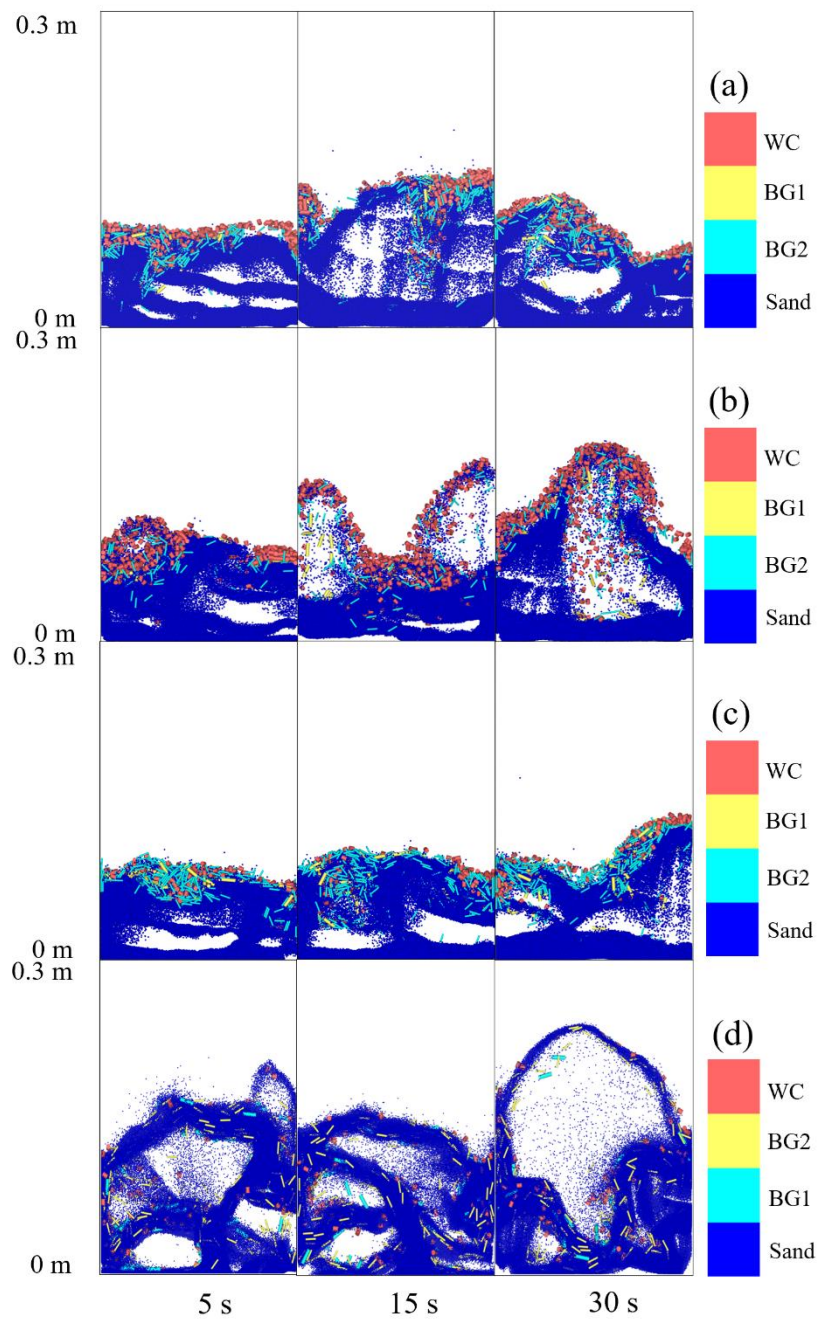


Figure 4.7 Flow patterns for the mixture of silica sand and mixed biomass with 5% loading and different blending ratios between wood chip and coarse bagasse of (a) 1:1, (b) 3:1, (c) 1:3 and (d) 1:3 using silica sand size of 1 mm.

The solid volume fraction along the bed height depicted in Figure 4.8 provides further confirmation that the biomass blending ratio has an influence on the flow behavior. In Figures 4.8(a) and (b), it can be observed that the fractions of silica sand are significantly lower at the height where the majority of biomass fractions, particularly wood chip, are distributed. In these cases, biomass particles tend to have higher fractions on the top surface of the silica sand, resulting in partial mixing. In contrast, Figure 4.8(c) shows that the fractions of wood chip and coarse bagasse are nearly equal and exhibit a similar distribution profile. This suggests that some coarse bagasse particles are able to penetrate the wood chip, assisting the mixing of different biomass types and emphasizing the significance of particle size distribution. However, regardless of the blending ratio, there is still some segregation of silica sand, which remains predominantly located at the bottom of the bed. This indicates that certain operational parameters may need to be adjusted in order to improve the behavior and achieve better mixing.

Figure 4.9(a) compares the variations in the mixing index over time and determines whether the biomass blending ratio affects the flow pattern of binary mixtures. The results show that the mixing indexes do not exhibit significant differences; however, at stable mixing, the blending ratio of 1:3 of wood chip to coarse bagasse appears to have a higher mixing index. When compared to the case of coarse bagasse in a single biomass mixture, the mixing index of the mixed biomass mixture is lower. Conversely, when compared to wood chip, the mixing index of the mixed biomass mixture is higher than that of the single biomass mixture. This observation suggests that introducing alternative biomass such as coarse bagasse can help address the flow behavior issues associated with primary biomass like wood

chips. However, the mixing index value of around 0.5 at stable mixing indicates that the mixing of the mixed biomass and silica sand is poor under these conditions. Additionally, Figure 4.9(b) examines the effect of different biomass loadings on the mixing index. It is evident that the mixing indexes do not change significantly as the biomass loading increases. Considering that the biomass mass content in real fluidized bed operation typically ranges from 1% to 5% [5], a loading of 5% from the 1:3 wood chip to coarse bagasse ratio is determined to be an appropriate condition. However, the slight increase in the mixing index from 2.5% to 7.5% in the case of the wood chip and coarse bagasse ratios of 1:1 and 3:1 could be attributed to an increase in the number of cylindrical biomass particles, resulting in a higher void fraction. This, in turn, allows silica sand to penetrate the spaces between the biomass particles, leading to a slight improvement in mixing. Furthermore, a larger number of bubbles can rise through the bed with a more uniform distribution of small bubbles, which enhances mixing. Therefore, the effective condition identified in this study is the use of a mixed biomass mixture comprising wood chip and coarse bagasse with a blending ratio of 1:3 and a loading of 5%.

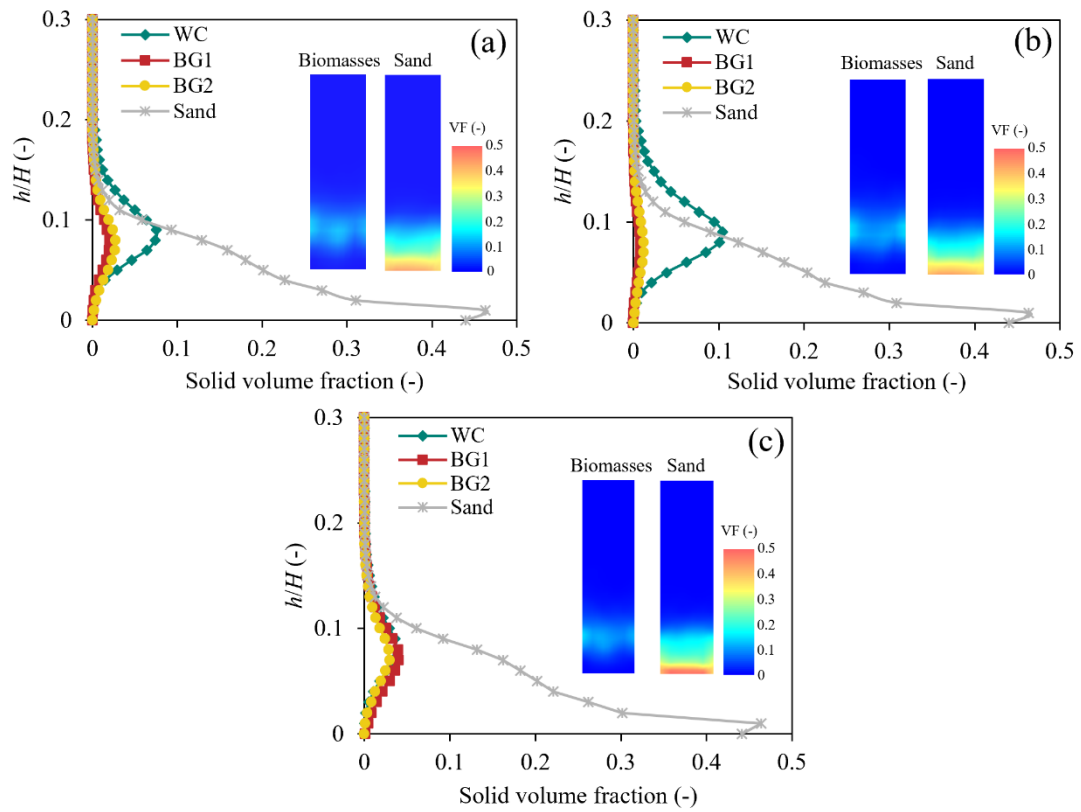


Figure 4.8 Time-averaged solid volume fraction of particles along the bed height for the mixed biomass with 5% loading in the different blending ratios between wood chip and coarse bagasse of (a) 1:1, (b) 3:1 and (c) 1:3.

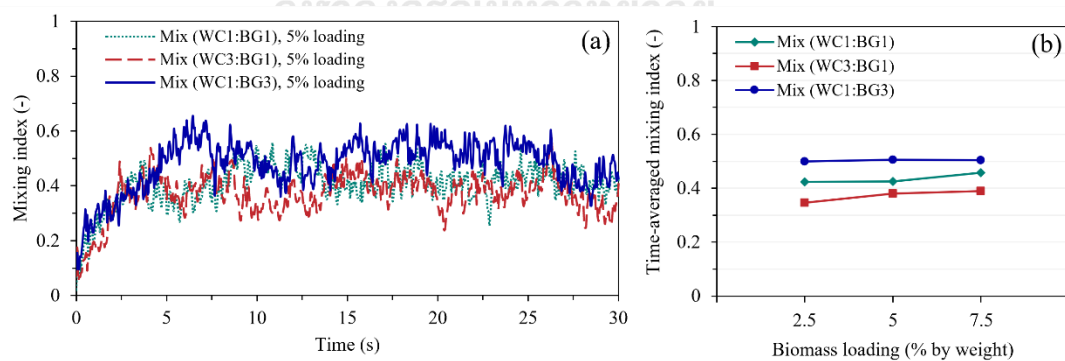


Figure 4.9 (a) Mixing index changes with time and (b) comparison of the time-averaged mixing indexes with the variation of biomass loading for different blending ratios of mixed biomass.

4.3.3. Effect of silica sand size

When examining the flow pattern in Figures 4.7(a)-(c), it becomes evident that the mixed biomasses tend to distribute predominantly at the top of the bed, leading to segregation from the silica sand. This segregation occurs because the silica sand particles are unable to penetrate and mix with the biomasses. Additionally, the distribution of silica sand does not create turbulent movement of the biomass particles. To explore the effect of inert particle size on the fluidization behavior, the size of silica sand particles varied from 1.6 mm to 1 mm. This investigation is carried out using the effective condition identified earlier, which involves a mixed biomass mixture of wood chip and coarse bagasse with a blending ratio of 1:3 and a loading of 5%. As shown in Fig. 4.7(d), the bed height is observed to increase due to the rapid expansion of the mixture particles. Simultaneously, the smaller silica sand particles exhibit turbulent movement and can penetrate the mixed biomasses due to the formation of a void structure at the interface between silica sand and the biomass mixture. As the bubbles rise and eventually burst at the surface, the biomasses are thrown towards both sides of the left and right walls. After a period of bubble disturbance, which includes formation and collapse, and the influence of solid back-mixing along the wall region, the mixture is considered to reach a stable mixing state after approximately 5 seconds. Moreover, reducing the size of the silica sand particles promotes particle-to-particle contact, resulting in increased overall fluidization intensity and a higher degree of bed expansion. This leads to a more uniform axial distribution of the biomasses in the upper region of the bed [100]. It is also worth noting that the mixing quality appears to improve when there is a larger difference in

equivalent size between the biomass and silica sand, as opposed to using larger silica sand particles with a size of 1.6 mm.

The particle volume fraction along the bed height in Figure 4.10 confirms that the distribution of biomasses varies with changes in silica sand sizes. When using smaller silica sand, the volume fraction profiles of biomass particles appear flatter compared to those using larger silica sand. This indicates that the biomasses tend to distribute more vertically to mix with the silica sand, which also shows a more vertical distribution rather than accumulating at the bottom of the bed. Additionally, the contour plot suggests that the biomasses distribute more evenly on both sides of the walls, which aligns with the flow behavior depicted in Figure 4.7(d). Furthermore, the particle volume fraction in the horizontal direction is examined at different heights of 0.07 and 0.1 m in Figure 4.11. According to the flow behavior, the smaller silica sand is denser at the height of 0.1 m, whereas the larger silica sand is denser at the height of 0.07 m. However, for the considered heights, the biomasses using smaller silica sand are less dense compared to those with larger silica sand.

In addition, the variation of the mixing index with time confirms the improved mixing behavior resulting from the change in silica sand size, as depicted in Figure 4.12. The mixing indexes with smaller sand size are notably higher than those with larger silica sand, both in the case of single biomass and mixed biomass mixtures. The average mixing index of the mixed biomass increases to 0.7, which is lower than the case of coarse bagasse that reaches 0.8. Nevertheless, by introducing alternative biomass and reducing the size of inert particles, the mixing behavior can be enhanced compared to using a single primary biomass alone. This results in a higher average mixing index for the mixed biomass compared to using wood chip alone. Therefore,

based on the comparison of the case studies, the appropriate condition for the biomass mixture is a blending ratio of 1:3 of wood chip to coarse bagasse with a 5% biomass loading using 1 mm silica sand. Moreover, the primary significant factor in selecting biomass size for fluidized bed systems is the difference in equivalent particle diameters.

To generalize the findings regarding the appropriate biomass mixture conditions for use in other systems, it is beneficial to express the size of silica sand in terms of a dimensionless parameter. Specifically, the ratio of the average equivalent diameter of the biomasses to the equivalent diameter of the silica sand provides a meaningful comparison. Based on the outcomes of the study under the investigated operational conditions of an air velocity of 1.8 m/s and an air temperature of 488 °C, the suitable condition for the biomass mixture in a general case would be a blending ratio of 1:3 of wood chip to coarse bagasse with a 5% biomass loading using a ratio of the average equivalent diameter of the biomasses to the equivalent diameter of silica sand of 4.44.

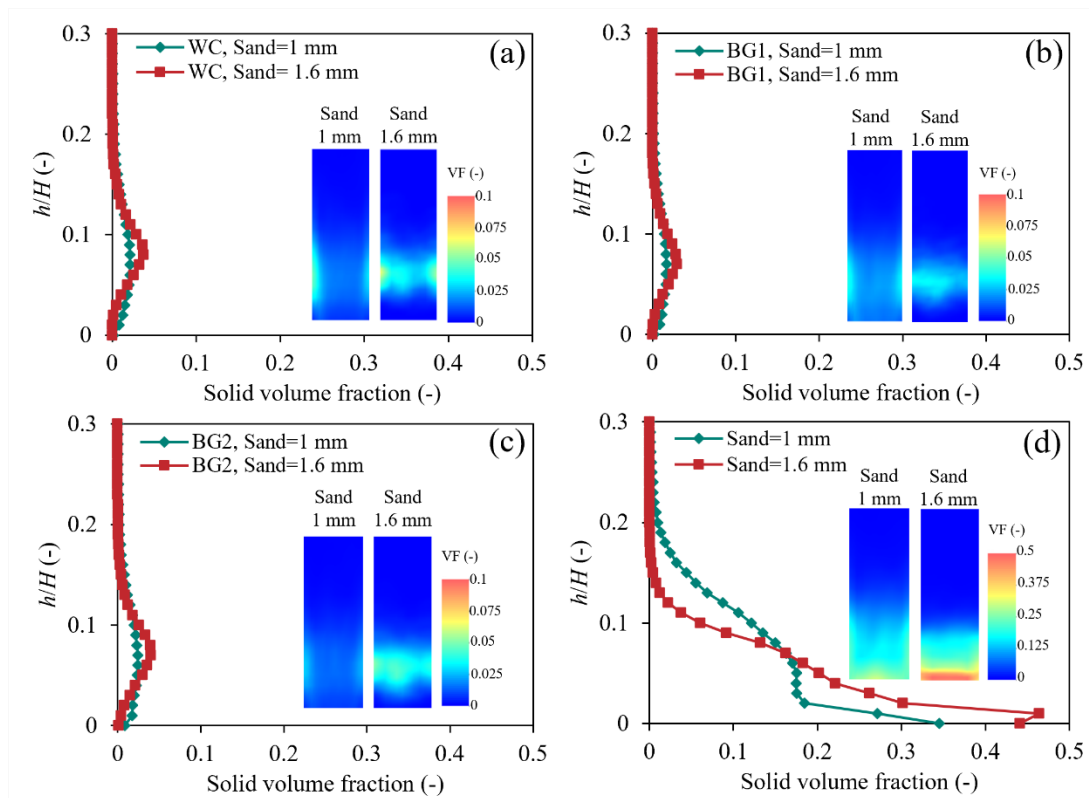


Figure 4.10 Comparison of time-averaged solid volume fraction of particles along the bed height for the mixed biomass (WC1:BG3) with 5% loading and different silica sand sizes.

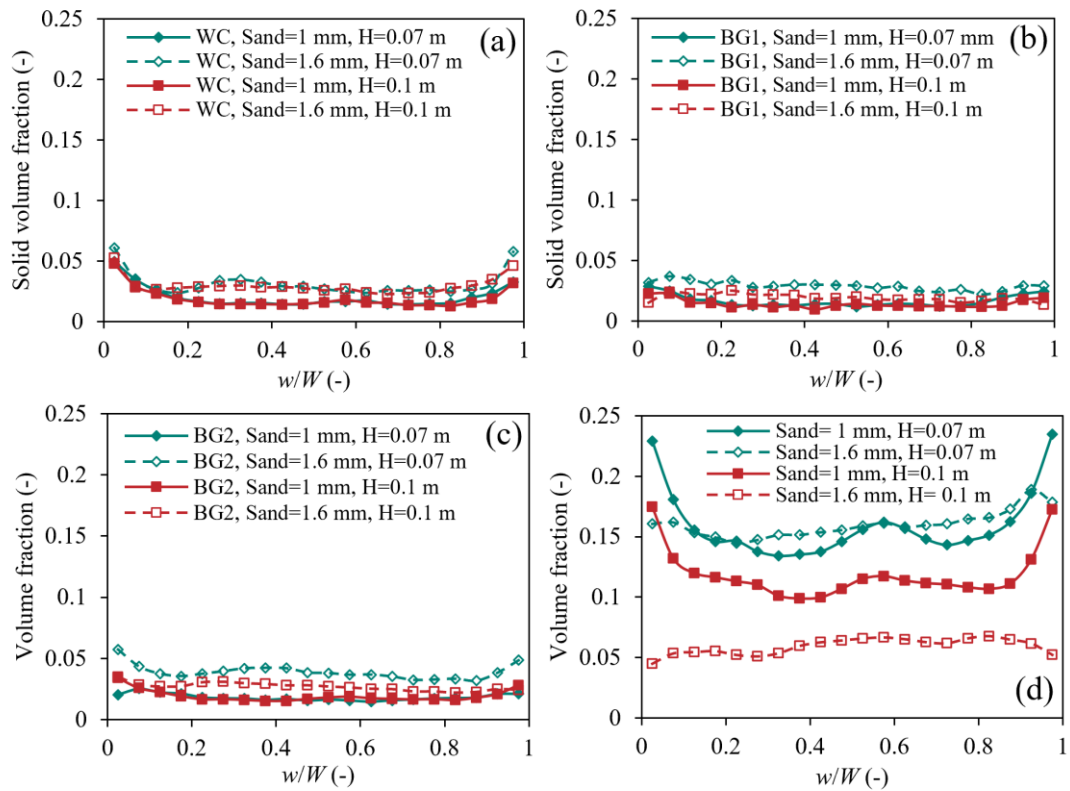


Figure 4.11 Time-averaged solid volume fraction in the horizontal direction at different heights of 0.07 and 0.1 m for the mixed biomass (WC1:BG3) with 5% loading and different silica sand sizes.

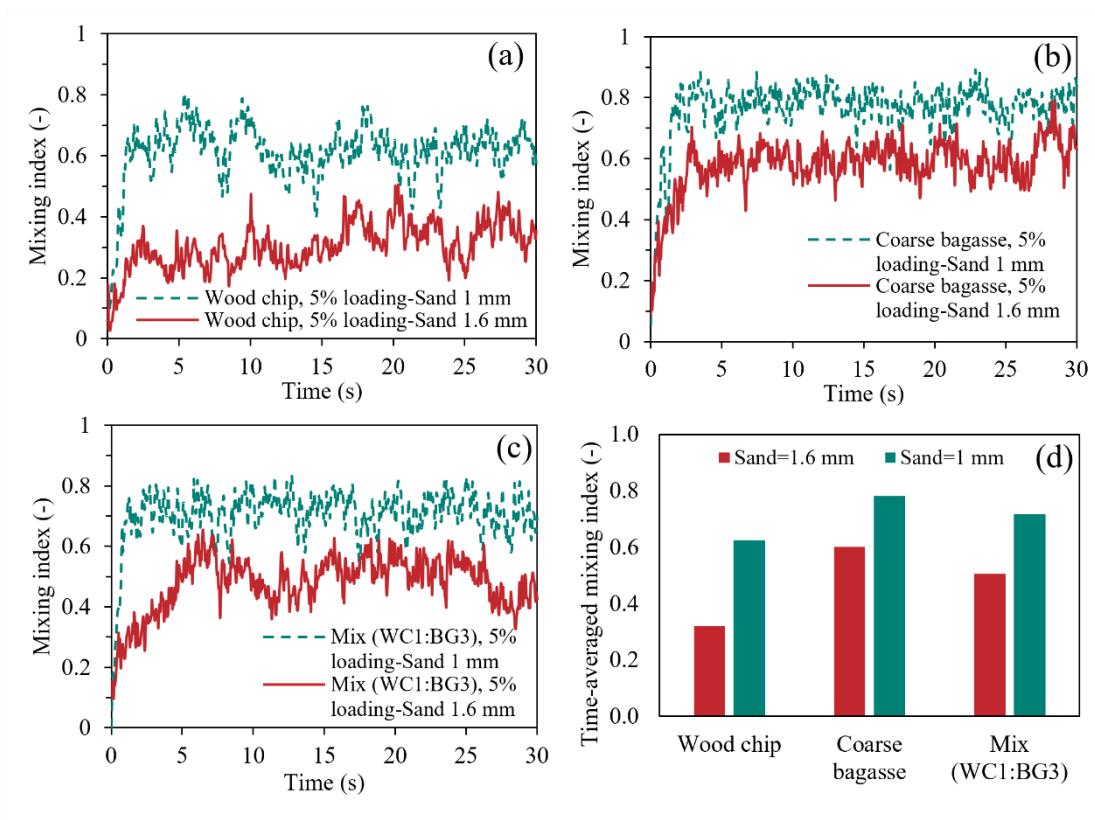


Figure 4.12 Comparison of mixing index variation with time for the mixture of (a) wood chip, (b) coarse bagasse, (c) mixed biomass (WC1:BG3) with 5% loading and silica sand with different sizes and (d) comparison of the time-averaged mixing indexes with the different mixtures and silica sand sizes.

4.3.4. Heat transfer behavior

Figures 4.13(a) and (b) show the changes in average particle temperature over time for different sizes of silica sand in the mixed biomass mixture. It can be observed that the particle temperature slightly increases over time, and there is little variation between wood chip and silica sand when using different silica sand sizes. However, the average temperature of wood chip and silica sand is lower when smaller silica sand is employed. The probability function of particle temperature was also examined for different silica sand sizes, as shown in Figures 4.13(c) and (d). At the particle scale, it is evident that the particle temperature is generally higher when using 1.6 mm silica sand, except for some BG1 and BG2 particles that exhibit higher temperatures. The bed height expansion is greater with 1 mm silica sand, resulting in higher bed voidage. In contrast, 1.6 mm silica sand tends to be concentrated near the bottom of the bed. The high convective heat transfer rate at the bottom of the bed may explain why the 1.6 mm silica sand exhibits higher temperatures [111]. Furthermore, the use of 1 mm silica sand brings about an expanded bed and modifies the intensity of fluidization, potentially leading to enhanced convective heat transfer among the silica sand, biomasses, and air. This change in behavior also leads to improved distribution of the biomasses and higher temperatures for some BG1 and BG2 particles, although not for wood chips. Since there is a small amount of wood chips on the surface, they are less influenced by the highly convective heat transfer occurring at the bottom of the bed. However, when examining the temperature at the individual particle scale, there is only a slight temperature difference, as the average temperatures of the wood chips remain nearly identical, as demonstrated in Figures 4.13(a) and (b). To validate the examination of temperature differences at the individual particle level, the average

convective heat transfer rate over time is presented in Figures 4.13(e) and (f) for various silica sand sizes. In the bubbling fluidized bed, conductive heat transfer occurs during particle collisions. However, since these collisions are random and discontinuous, conductive heat transfer cannot take place simultaneously on all particles within the system, making it the least significant heat transfer mode among all [91, 111-113]. Consequently, under the current simulation conditions, convective heat transfer predominantly governs the heat transfer process on biomass particles. Therefore, heat is transferred from silica sand to biomass through both particle-particle conductive heat transfer and convective heat transfer, resulting in temperature variations within individual particles. The convective heat transfer of larger silica sand is greater than that of smaller silica sand, highlighting the importance of selecting the appropriate size for inert particles. Although the convective heat transfer of biomass particles does not exhibit significant differences with respect to silica sand size, the particle temperatures vary, as depicted in Figures 4.13(c) and (d), with certain BG1 and BG2 particles exhibiting higher temperatures and wood chips exhibiting lower temperatures. Consequently, if the mixing behavior of biomass and silica sand is enhanced through the use of smaller silica sand size, the heat transfer behavior of the mixed biomass may be altered.

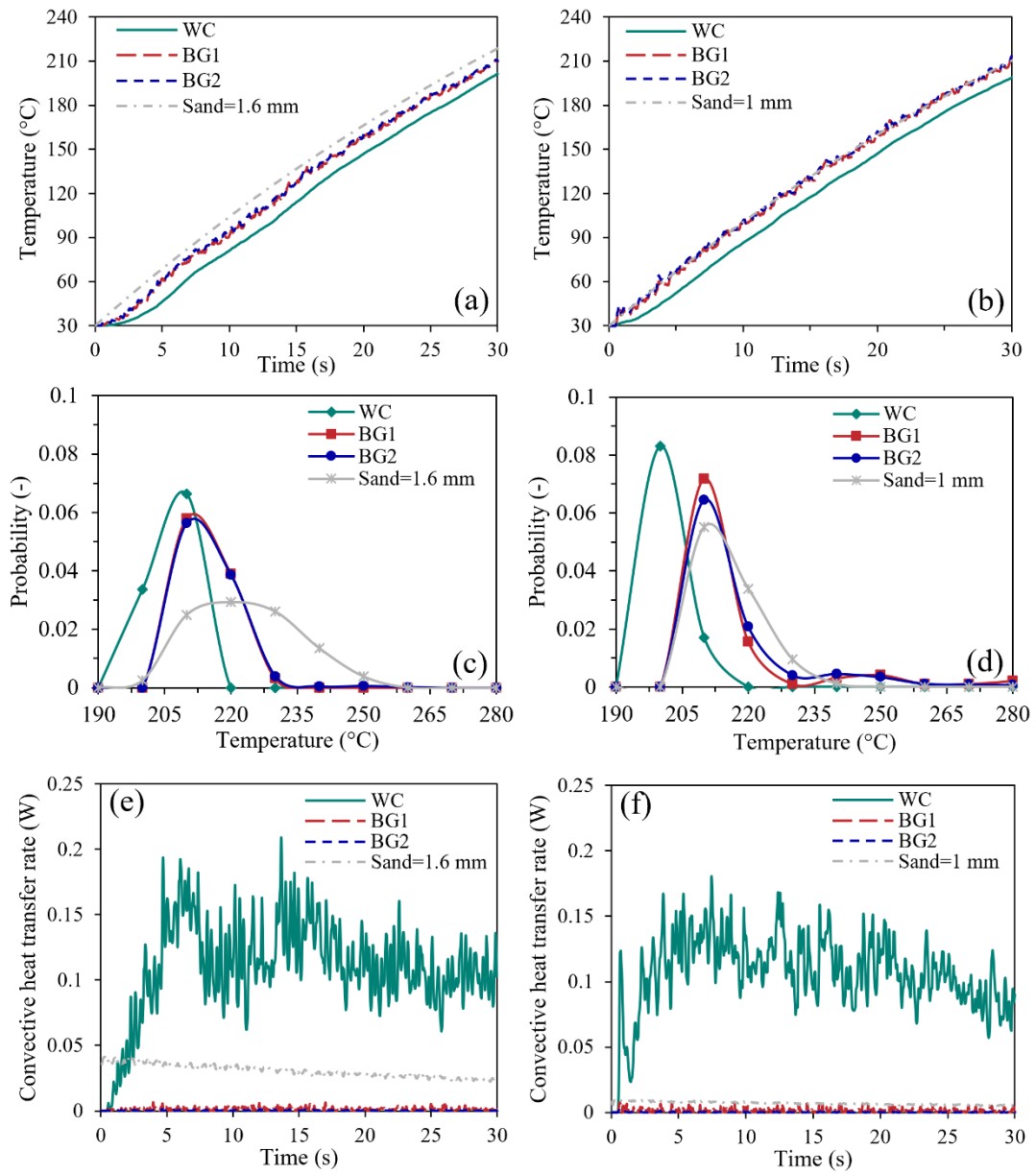


Figure 4.13 The evolution of the average particle temperature, (c), (d) probability distribution of particle temperature, and (e), (f) the evolution of the average convective heat transfer rate for different particles in case of mixed biomass (WC1:BG3) with 5% loading and different silica sand sizes.

4.3.5. Force analysis

The analysis of interaction forces plays a crucial role in gaining a deeper understanding of the underlying mechanisms involved. The behavior of particles within a fluidized bed is influenced by various interactions, including particle-particle, particle-wall, and particle-fluid interactions, in addition to gravitational forces. The inter-particle forces considered in this study include normal contact forces, drag forces, and pressure gradient forces, as illustrated in Figure 4.14. It is important to note that the force ratios were normalized by dividing them with the particle gravity, mg . In Figures 4.14(a) and (b), the peaks of the frequency curves for contact forces shift towards the right and become broader when smaller silica sand is used. This observation is connected to the higher fluidization intensity found in the study, which leads to a more uniform distribution of the biomass particles. Furthermore, despite having a smaller equivalent diameter, BG2 experiences the highest contact force among the biomass particles. This means that there are more chances of colliding with other particles, as well as demonstrating the significance of considering the particle size distribution of bagasse particles. As depicted in Figures 4.14(c) and (d), silica sand exhibits the highest drag force, which drags particles in an upward motion with greater intensity. When smaller silica sand is used, the frequency curves for the drag force of the biomass particles shift towards the left, while the curve for silica sand shifts towards the right. Generally, the local porosity and cross-sectional area significantly affect the drag force, with denser regions experiencing higher drag forces compared to looser regions due to differences in porosity and permeability. Moreover, as the porosity increases, the dominant factor influencing the aspect ratio's effect on drag force shifts to the cross-sectional area, which is closely related to particle

orientation. This distinction emphasizes the difference between using non-spherical particles, such as cylindrical biomass, and spherical silica sand, which does not exhibit any specific orientation [114].

Additionally, as illustrated in Figures 4.14(e) and (f), particle shape plays a significant role in the frequency distribution of pressure gradient forces. The pressure gradient force acting on spherical silica sand exhibits a more uniform distribution compared to biomass particles. When examining the frequency curves for biomass particles, they become wider with lower peaks, indicating that biomass experiences a broader range of pressure gradient forces compared to spherical silica sand. The slight differences in peak height or width of the curves are observed when comparing wood chip and BG1, which have larger sizes than BG2, specifically when smaller sand sizes are used. This analysis is based on the peaks of the contact force frequency curves, which suggest that wood chip and BG1 have a lower probability of colliding with other particles compared to BG2. Consequently, the fluid has a greater influence, leading to higher pressure gradients. However, there is no notable difference in the curve for silica sand when the system changes to using a smaller size. Note that the pressure gradient force acting on silica sand is less than one, indicating that the positive particle-particle interaction force from cylindrical biomass particles is necessary to suspend spherical silica sand within the bed [41].

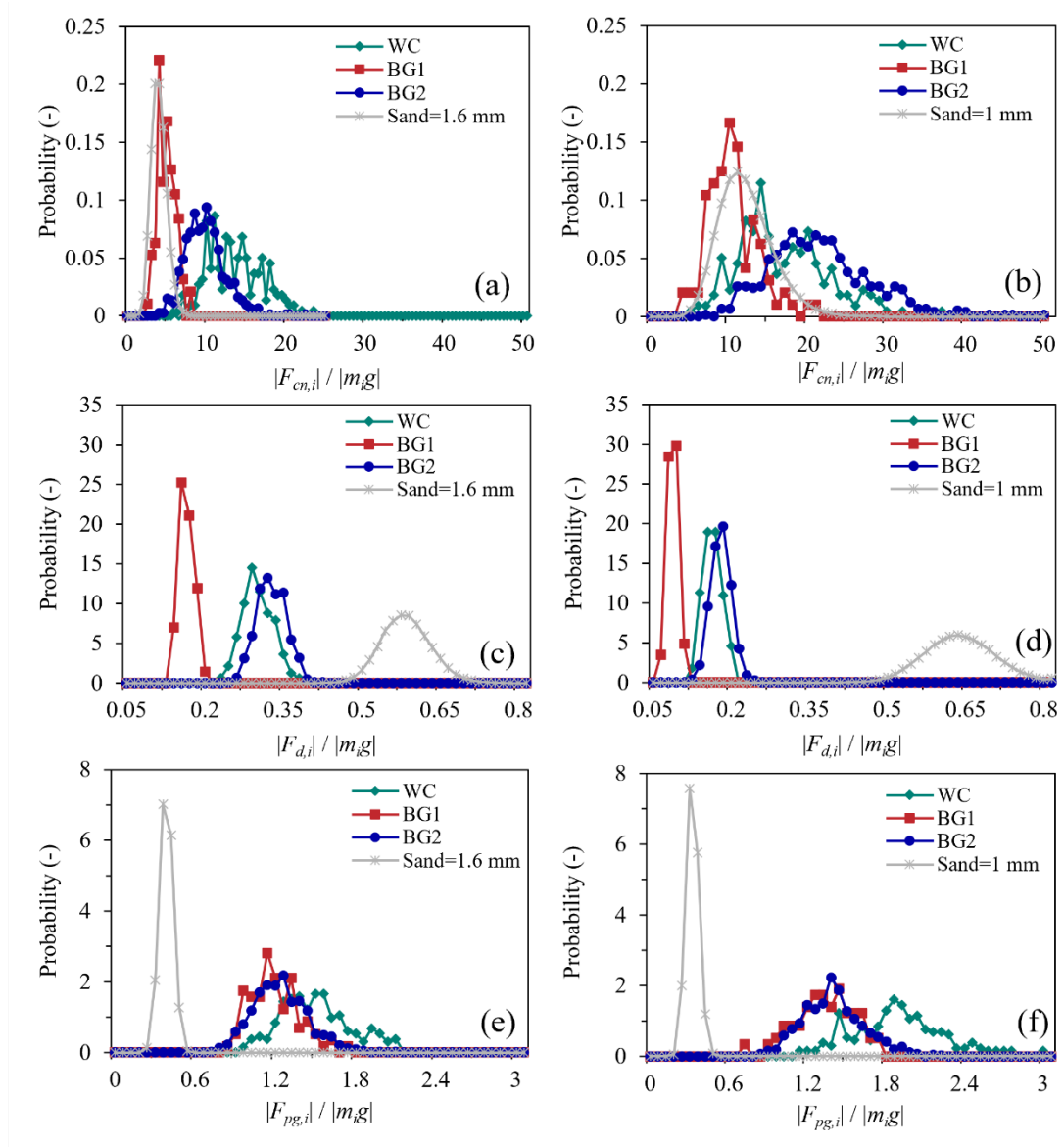


Figure 4.14 Probability distribution of (a), (b) normalized normal contact forces (c), (d) normalized drag forces and (e), (f) normalized pressure gradient forces on individual particles in case of mixed biomass (WC1:BG3) with 5% loading and different silica sand sizes.

4.3.6. Limitations related to actual operation

When biomass is used as fuel, it is crucial to ensure that the particle size is suitable for efficient combustion and fluidization within the system. Even though the optimal operating condition for choosing the appropriate condition for the biomass mixture is successfully established in this study, using biomass with a specific particle size may still require additional energy consumption for processes such as crushing or size reduction. In certain cases, biomass feedstocks must undergo size reduction through mechanical crushing or grinding to attain the desired particle size. The energy required for size reduction depends on factors such as initial biomass size, desired final particle size, and the specific equipment and methods employed. Energy consumption for biomass size reduction can impact the overall energy efficiency of the system. It is important to weigh the energy consumed for size reduction against the potential benefits of using biomass with the desired particle size, such as improved combustion efficiency and reduced emissions. Additionally, factors such as biomass availability, handling and storage requirements, and the specific needs of the combustion system should be considered when choosing the particle size of biomass. These considerations contribute to optimizing the overall energy consumption and performance of the biomass combustion process.

Furthermore, if combustion is included in the developed model in this study, it is important to determine the maximum air velocity for the combustion system while considering the appropriate air-to-fuel ratio. Several factors need to be taken into account when considering combustion. Although the study has obtained the appropriate biomass condition, there are other properties of the fuel, such as composition and moisture content, which were not considered in this study, that could

affect the combustion process. These properties have an impact on the required air velocity for proper fuel-air mixing and combustion. The ideal air-to-fuel ratio for efficient combustion varies depending on the type of fuel being used, and it is crucial to maintain a balanced ratio to ensure complete combustion and minimize emissions. Additionally, the design of the combustion chamber influences the maximum air velocity. Factors such as the size, shape, and configuration of the chamber affect the flow dynamics and determine the sustainable maximum air velocity without causing turbulence, inefficient mixing, or flame instability. It is also important to consider any constraints or limitations of the system, such as equipment capabilities, pressure drop limitations, and safety factors related to construction. These constraints can impact the maximum air velocity that can be utilized in the system. By considering these factors and conducting thorough analysis or experimental studies, it is possible to determine the maximum air velocity that can be used in the combustion system while maintaining the appropriate air-to-fuel ratio for efficient combustion.

4.4. Conclusion

This chapter uses a CFD-DEM approach to examine the hydrodynamics and heat transfer behavior in a bubbling fluidized bed containing mixed biomass particles (cylindrical wood chip and bagasse) and spherical silica sand. The investigation focuses on understanding the impact of different biomass types, loadings, and blending ratios on mixing behavior, and solid temperature distribution. The key findings of this study can be summarized as follows:

(1) Coarse bagasse biomass provides efficient mixing behavior and achieves the highest mixing index compared to other biomass types in single biomass mixtures.

The difference in aspect ratio and equivalent diameter of certain biomass particles contributes to their effective mixing behavior. Therefore, a blending ratio of 1:3 of wood chip to coarse bagasse, along with a 5% biomass loading, is identified as the appropriate condition for the mixed biomass mixture, indicating the importance of particle size distribution. Furthermore, the study reveals that varying biomass loadings do not significantly affect the mixing behavior.

(2) Using smaller silica sand particles of 1 mm changes the fluidization intensity and enhances the mixing efficiency in all case studied. As a result, the blending ratio of 1:3 of wood chip to coarse bagasse, along with a 5% biomass loading and the use of 1 mm silica sand, is the suitable condition for the mixed biomass mixture. Furthermore, the difference in equivalent particle diameters is identified as the primary determining factor when selecting the appropriate biomass size for fluidized bed systems. In addition, the appropriate condition for the biomass mixture in a general case would be a blending ratio of 1:3 of wood chip to coarse bagasse with a 5% biomass loading using a ratio of the average equivalent diameter of the biomasses to the equivalent diameter of silica sand of 4.44.

(3) The average particle temperature shows a slightly increase over time, with little variation observed in wood chip and silica sand when different sizes of silica sand are used. However, the use of different silica sand sizes has a significant impact on the expanded bed height and fluidization intensity, leading to variations in the distribution of particles within the fluidized bed. These variations in silica sand sizes also result in different particle convective heat transfer rates, thereby influencing the temperature distribution within individual particles. Consequently, if the mixing behavior of

biomass and silica sand is enhanced by using smaller silica sand particles, it can potentially lead to improved heat transfer behavior in the mixed biomass mixture.

(4) The enhanced mixing behavior and heat transfer can be attributed to the interaction forces between particles and between particles and the fluid. The use of smaller silica sand particles increases the chance of contact forces, which is closely related to the observed higher fluidization intensity. Moreover, the cross-sectional area, which is influenced by the orientation of cylindrical biomass particles, plays a significant role in determining the impact of different aspect ratios on drag force. Furthermore, biomass particles have a wider range of pressure gradient forces compared to spherical silica sand particles, whereas there is no significant difference in pressure gradient forces when smaller silica sand particles are used in the system.

It is important to acknowledge that the aforementioned conclusions are specific to the conditions examined in this study. Different outcomes or trends may arise when the conditions are modified. Therefore, to deepen our understanding of the intrinsic relationship between gas-solid mixing, the combustion process, and combustion efficiency, it would be advantageous to incorporate a chemical reaction model into the developed CFD-DEM model. Furthermore, when selecting a mixed biomass according to the appropriate conditions, it is crucial to consider other factors, such as the availability of biomass feedstocks, handling and storage requirements, and specific requirements of the combustion system. These considerations can help optimize the overall energy consumption and performance of the biomass combustion process. Nevertheless, the current model provides valuable insights for recommending efficient biomass conditions in a fluidized bed combustor, thus contributing to the realization of industrial boilers and their optimal operation.

CHAPTER 5

EFFECT OF DESIGN PARAMETERS ON THE HYDRODYNAMICS AND HEAT TRANSFER IN A BUBBLING FLUIDIZED BED COMBUSTOR WITH IMMERSED TUBES

A fluidized bed, known for its high efficiency in gas-solid contact and excellent heat and mass transfer performance, has found widespread use in various chemical processes. To regulate operating temperatures, facilitate heat exchange, and improve particle mixing, immersed tubes are introduced into the system. The presence of immersed tubes in the fluidized bed restricts the size of bubbles, facilitating increased contact between the gas and solid phases and enhancing mixing efficiency [115, 116]. However, when dealing with biomass particles, which have non-spherical shapes and a wide size distribution, the incorporation of immersed tubes in a fluidized bed system becomes challenging, especially when using a mixture of biomass and silica sand. Thus, there is a need for a comprehensive exploration of the influence of immersed tubes on hydrodynamics and heat transfer in such systems.

Design of experiments (DoE) has been used in combination with computational studies [117, 118]. Utilizing DoE not only reduces the number of required runs but also allows for the development of a second-order model based on the results. This enables the creation of a response surface that reveals potential optimal points.

Although various studies in the literature have investigated the effects of different design parameters on hydrodynamics and heat transfer in fluidized beds with immersed tubes, the relative importance of these effects has not been fully established. This chapter aims to extend on previous chapter by examining the effects

of design parameters on a mixed biomass bubbling fluidized bed combustor with immersed tubes. The investigation includes an analysis of hydrodynamics, heat transfer, and the local instantaneous heat transfer coefficient (HTC) around the immersed tubes in the system. To achieve this, a combination of the CFD-DEM approach and a 2^k factorial design using DoE is employed to assess the influence of design parameters such as the angle between tubes, tube diameter, and distance between tubes on mixing behavior and heat transfer in the bubbling fluidized bed combustor with immersed tubes.

5.1. Statistical Design of Experiment

The 2^k factorial design of experiments is a suitable statistical approach for investigating the effects of considered parameters, including main effects and interaction effects, on observed responses. This method has been employed in studying complex gas-solid systems like the fluidized bed system. Therefore, in this study, a 2^k factorial experimental design was used, where 2 represented the levels of the considered parameters, and k denoted the number of parameters under investigation.

The main objective is to explore the impact of these design parameters related to the immersed tubes on the hydrodynamics and heat transfer, which potentially affect chemical reaction characteristics within the fluidized bed. The investigated design parameters are examined using a 2^3 factorial design of experiments, incorporating the angle between tubes (A), tube diameter (B), and distance between tubes (C). Each parameter is varied at two levels: a low level (-1) and a high level (+1). The levels for each factor in the 2^3 DoE are presented in Table 5.1, with the

chosen parameter values derived from literature and real operational data. The angle between tubes are 0 and 45 degrees, corresponding to the in-line and staggered tube configurations, respectively, as previously studied in the literature [119, 120]. In addition, two tube diameters are considered: 10.3 mm and 17.1 mm, representing the actual sizes of schedule 40 stainless steel pipes. Furthermore, the distance between tubes are 36.05 mm and 41.2 mm, enabling an investigation of the impact of pitch length. It is important to note that the chosen treatment is reasonable, as the present study indicated that the interaction between neighboring tubes is negligible when the pitch length exceeds at least 1.5 times the tube diameter [73]. Moreover, the significance of the response is evaluated using a p-value of less than or equal to 0.05 at a confidence interval of 95%. The process responses are the average radial solid volume fraction, the average radial solid temperature at different heights: 0.065 m, 0.1 m, and 0.14 m and the average mixing index. These heights correspond to the position of the lower immersed tubes, the interval between row 1 and row 2 of tubes, and the interval between row 2 and row 3 of tubes, respectively.

Table 5.1 2^k Factorial experimental design for designing parameters of bubbling fluidized bed combustor with immersed tubes.

Case	Angle between tubes (A)	Tube diameter (B)	Distance between tubes (C)	Angle between tubes (deg)	Tube diameter (mm)	Distance between tubes (mm)
1	-1	-1	-1	0	10.3	36.05
2	-1	-1	1	0	10.3	41.2
3	-1	1	-1	0	17.1	36.05
4	-1	1	1	0	17.1	41.2
5	1	-1	-1	45	10.3	36.05
6	1	-1	1	45	10.3	41.2
7	1	1	-1	45	17.1	36.05
8	1	1	1	45	17.1	41.2

5.2. Geometry, initial and boundary conditions

This chapter uses the bubbling fluidized bed combustor, employing the same dimensions and grid sizes as described in chapter 4, as shown in Figure 5.1. Based on the findings from the previous chapter, the following conditions are adopted for this chapter: a suitable mixture of biomass with a blending ratio of 1:3 of wood chip to coarse bagasse, a 5% biomass loading, and 1 mm silica sand particles. During the initial packing stage, these particles are allowed to freely fall and pack, resulting in a predetermined initial bed height. The total mass of the particles used for packing is 400 g, and their initial temperature is 30 °C. The silica sand particles are randomly generated at the bottom, utilizing the remaining mass after the biomass loading. Subsequently, biomass particles are introduced by falling from a specific height due to gravity. Notably, the wood chip particles are positioned on top of all the particles,

followed by the coarse bagasse particles (BG1 and BG2) and silica sand. The initial packing process continues until the velocities of all particles approach zero. Air is introduced into the bed through a bottom inlet with a uniform velocity of 1.8 m/s, which is consistent with the inlet boundary condition used in Chapter 4. This ensures that the same conditions are maintained to accurately compare the effects of various parameters, including operational and design parameters. The outlet pressure is set at 101,325 Pa, while the system walls are considered adiabatic and assigned a no-slip boundary condition. Furthermore, the temperature of each immersed tube remains constant at 340 °C, which corresponds to the average temperature of the cooling water flowing through the tubes during the actual operation of fluidized bed boilers by Integrated Research Center Company Limited (IRC) in Thailand. Moreover, the other models and parameters utilized in this chapter are consistent with those presented in Table 4.1 in Chapter 4.

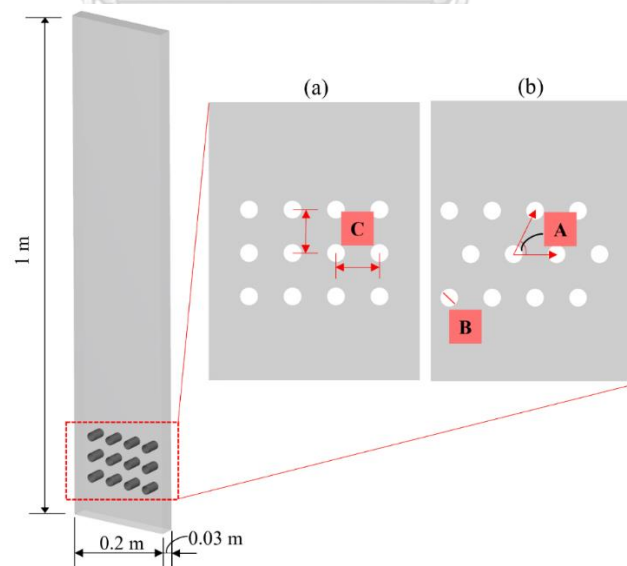


Figure 5.1 Schematic drawing of the bubbling fluidized bed combustor with a
 (a) in-line and (b) staggered immersed tubes configurations.

5.3. Numerical model

The same numerical models as those used in Chapter 4 are employed in this chapter. The CFD simulation calculates the fluid flow field and provides relevant information at each time step. This information is then utilized by the DEM simulation to determine forces, positions, velocities, and heat transfer rates of individual particles. This enables the evaluation of porosity, volumetric particle-fluid forces, and energies within a computational cell. Additionally, the forces and heat transfer rates between immersed tubes and particles are also assessed within the DEM simulation. For the CFD simulation, the time step is set to 1×10^{-4} s, while for the DEM simulation, it is set to 2×10^{-5} s. The total simulation time for each case is 30 s. To measure the mixing quality of the mixture, the Lacey mixing index is utilized. It is observed that the mixing index reaches a relatively steady state after 5 s, and the time-averaged results are obtained based on the average data between 5 and 30 s.

5.4. Results and discussions

5.4.1. Parameter study

Table 5.2 provides a summary of the statistical experimental design conditions and the results for each process response, as shown in Figures 5.2 to 5.4. It should be noted that Case 0 corresponds to the results of Case 11 in Chapter 4, which represents the optimal operational condition based on the findings of the previous chapter. The main expected outcome was an improved mixing behavior of the mixed biomass and silica sand, resulting in a higher solid concentration within the combustion zone of the combustor. Therefore, the presented process responses include the average values of the mixing index, radial solid volume fraction, and temperature at various heights. In

addition, the trends for different parameters are illustrated in Figures 5.5 to 5.11. These figures display the averaged values of each response at both high and low levels of the considered input parameters.

Table 5.2 Results for the responses of fluidized bed with immersed tubes simulation.

Case	Responses						
	AVG Mixing Index	AVG SVF H=0.065 m	AVG SVF H=0.1 m	AVG SVF H=0.14 m	AVG Temp H=0.065 m	AVG Temp H=0.1 m	AVG Temp H=0.14 m
0	0.7312	0.2206	0.1637	0.0838	284.10	284.21	286.85
1	0.7713	0.2291	0.1950	0.0980	294.93	295.41	297.98
2	0.7761	0.2322	0.1832	0.0885	298.85	298.74	302.98
3	0.7529	0.2143	0.2015	0.1010	300.41	299.63	299.94
4	0.7584	0.2126	0.2010	0.1028	296.90	296.60	298.78
5	0.7769	0.2310	0.1973	0.0919	295.12	295.71	299.85
6	0.7659	0.2244	0.1983	0.0908	297.52	297.17	297.55
7	0.7602	0.2011	0.1929	0.1165	297.03	298.64	298.60
8	0.7604	0.1997	0.2188	0.1137	301.41	299.26	300.05

Table 5.3 ANOVA results for the responses.

Source of variation	SS	DF	MS	F ₀	P-value
(a) Mixing index					
A	2.80E-06	1	2.80E-06	125.25	0.0567
B	0.0004	1	0.0004	19001.6	0.0046
AB	0	1	0	1096.89	0.0192
AC	0.0001	1	0.0001	2477.75	0.0128
BC	0	1	0	786.11	0.0227
ABC	0	1	0	608.49	0.0258
Residual	2.23E-08	1	2.23E-08		
Total	0.0005	7			
(b) Average solid volume fraction at height of 0.065 m					
A	0.0001	1	0.0001	17.51	0.0139
B	0.001	1	0.001	134.22	0.0003
AB	0.0001	1	0.0001	6.91	0.0583
Residual	0	4	7.38E-06		
Total	0.0012	7			

Table 5.3 Continue

Source of variation	SS	DF	MS	F ₀	P-value
(c) Average solid volume fraction at height of 0.1 m					
A	0.0001	1	0.0001	4.57	0.122
B	0.0002	1	0.0002	10.48	0.0479
AC	0.0002	1	0.0002	9.98	0.0509
BC	0.0002	1	0.0002	8.46	0.0621
Residual	0.0001	3	0		
Total	0.0007	7			
(d) Average solid volume fraction at height of 0.14 m					
A	0.0001	1	0.0001	6.5	0.084
B	0.0005	1	0.0005	53.2	0.0053
AB	0.0001	1	0.0001	11.55	0.0425
ABC	0	1	0	2.15	0.2391
Residual	0	3	9.88E-06		
Total	0.0008	7			
(e) Average solid temperature at height of 0.065 m					
B	10.86	1	10.86	33.17	0.0288
C	6.47	1	6.47	19.75	0.0471
AC	5.08	1	5.08	15.5	0.0589
BC	3.7	1	3.7	11.3	0.0783
ABC	11.08	1	11.08	33.82	0.0283
Residual	0.655	2	0.3275		
Total	37.84	7			
(f) Average solid temperature at height of 0.1 m					
B	6.29	1	6.29	16.58	0.0267
AB	1.09	1	1.09	2.87	0.1888
BC	6.47	1	6.47	17.05	0.0258
ABC	3.81	1	3.81	10.03	0.0506
Residual	1.14	3	0.3795		
Total	18.8	7			
(g) Average solid temperature at height of 0.14 m					
A	1.65	1	1.65	2.52	0.2105
AB	1.53	1	1.53	2.34	0.2237
AC	2.74	1	2.74	4.19	0.1333
ABC	12.27	1	12.27	18.75	0.0227
Residual	1.96	3	0.6545		
Total	20.16	7			

Figure 5.2 shows the average mixing index based on the simulation results. It is observed that case 5, which used the angle between tubes of 45 degree, the tube diameter of 10.3 mm and the distance between tubes of 36.05 mm, achieved the highest mixing index value. Furthermore, the case with a smaller tube diameter of 10.3 mm exhibited a greater mixing index compared to the case with a larger tube diameter of 17.1 mm. To analyze the obtained simulation results, the average mixing index was subjected to ANOVA, as presented in Table 5.3a. The tube diameter (B), the interaction between the angle between tubes and tube diameter (AB), the interaction between the angle between tubes and distance between tubes (AC), the interaction between tube diameter and distance between tubes (ABC), and the interaction between the angle between tubes, tube diameter, and distance between tubes were found to significantly influence the average mixing index. The variation in tube diameter has a notable impact on flow dynamics and particle interactions, resulting in distinct mixing characteristics. When different tube diameters are employed, local flow velocities and turbulence levels near the tubes are altered. In addition, the interaction between tube diameter and other parameters, such as the angle between tubes and distance between tubes, affects the trend of the mixing index value. Hence, the trend of the mixing index is not solely determined by the variations in immersed tube size alone. Overall, the introduction of the tube bundle into the fluidized bed enhances the mixing index when compared to the fluidized bed without immersed tubes.

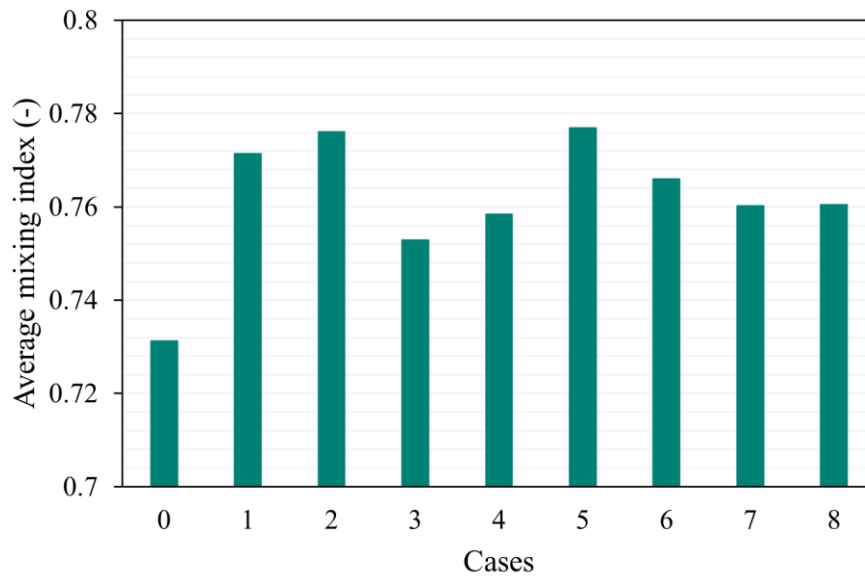


Figure 5.2 Results of the response of average mixing index for each experimental design case.

Figure 5.3 illustrates the obtained results for the average solid volume fraction in the radial direction at different heights. The insertion of tubes aims to enhance particle concentration in the combustion zone, particularly at the height corresponding to the interval between rows of tubes. Hence, at a height of 0.065 m, the solid volume fraction may be lower compared to the case where no tubes are inserted into the fluidized bed. In contrast, at heights of 0.1 and 0.14 m, the solid volume fraction could be higher when compared to using the fluidized bed without immersed tubes. The results obtained at a height of 0.065 m indicate that using a tube diameter of 17.1 mm leads to a lower solid volume fraction compared to using the fluidized bed without immersed tubes. The ANOVA presented in Table 5.3b reveals that the angle between tubes (A) and tube diameter (B) significantly influence the average solid volume fraction at this height of 0.065 m. Both the in-line and staggered tube

configurations have an impact on the flow patterns and interactions between particles, as well as between particles and tubes. This may prevent the accumulation of particles at the bottom of the bed. The choice of tube configuration plays a crucial role in promoting better dispersion and mixing of particles, thus reducing the solid volume fraction at the specified height. In addition, tubes with larger diameters offer increased space for particles to move and interact with one another. The expanded cross-sectional area encourages greater dispersion of particles and also provides additional pathways for the particles to flow through. This facilitates the redistribution of particles and helps prevent them from clustering or forming agglomerates at the bottom of the bed. Furthermore, at the heights of 0.1 m and 0.14 m, the average solid volume fraction in all cases is higher compared to the case without inserted tubes in the fluidized bed. This indicates that adding tubes to the system is beneficial for enhancing the mixing behavior of the mixed biomass. In Table 5.3c, it is observed that the tube diameter (B) significantly influences the average solid volume fraction at a height of 0.1 m. Similarly, at a height of 0.14 m, the tube diameter (B) and the interaction between the angle between tubes and tube diameter (AB) significantly affect the average solid volume fraction, as indicated in Table 5.3d. These results emphasize the importance of carefully selecting the tube size for the design and operation of the fluidized bed with immersed tubes.

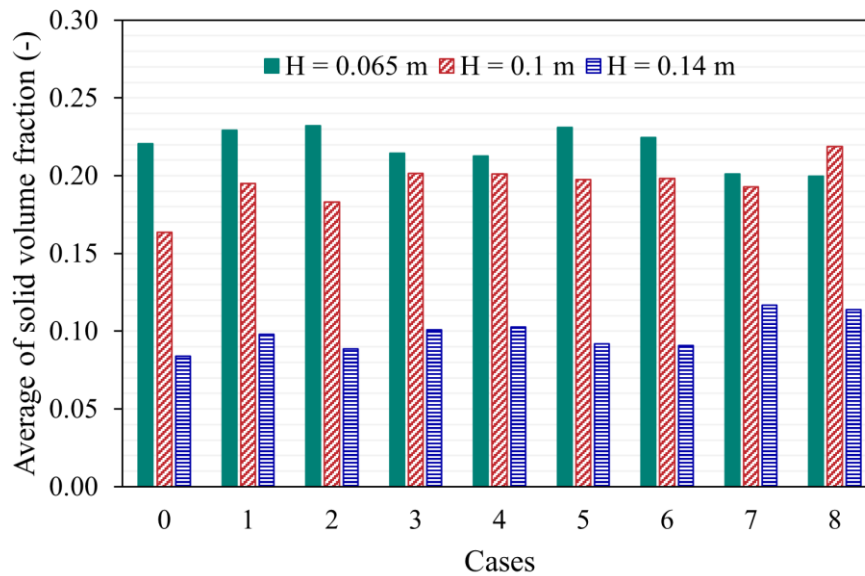


Figure 5.3 Results of the response of average solid volume fraction at different heights for each experimental design case.

Figure 5.4 displays the average particle temperature in the radial direction at various heights. It is evident that all cases of fluidized beds with immersed tubes exhibit higher particle temperatures at all heights compared to the fluidized bed without immersed tubes. This is attributed to the addition of heat sources that transfer heat to the particles through contact via heat conduction. Furthermore, the presence of immersed tubes may elevate the air temperature surrounding the tubes, leading to increased heat convection and consequently higher particle temperatures. The ANOVA analysis in Table 5.3e, Table 5.3f, and Table 5.3g reveals the significant influence of various parameters on the average particle temperature at different heights. At the height of 0.065 m, the tube diameter (B), the distance between tubes (C), and the interaction between the angle between tubes, tube diameter, and distance between tubes (ABC) significantly affect the particle temperature. Similarly, at the

height of 0.1 m, the tube diameter (B) and the interaction between tube diameter and distance between tubes (BC) have notable effects. Finally, at the height of 0.14 m, the interaction between the angle between tubes, tube diameter, and distance between tubes (ABC) significantly influences the particle temperature. From these analyses, it can be summarized that the main parameters influencing particle temperature are the tube diameter and the distance between tubes, also known as the pitch length. The tube diameter affects the contact area between the tubes and particles, allowing for increased heat transfer efficiency due to a larger surface area. Additionally, the pitch length could promote greater interaction and heat exchange between particles and tubes, leading to improved heat transfer efficiency through enhanced mixing and extended contact time. Overall, the tube diameter and pitch length play crucial roles in determining the particle temperature and optimizing heat transfer in the fluidized bed with immersed tubes.

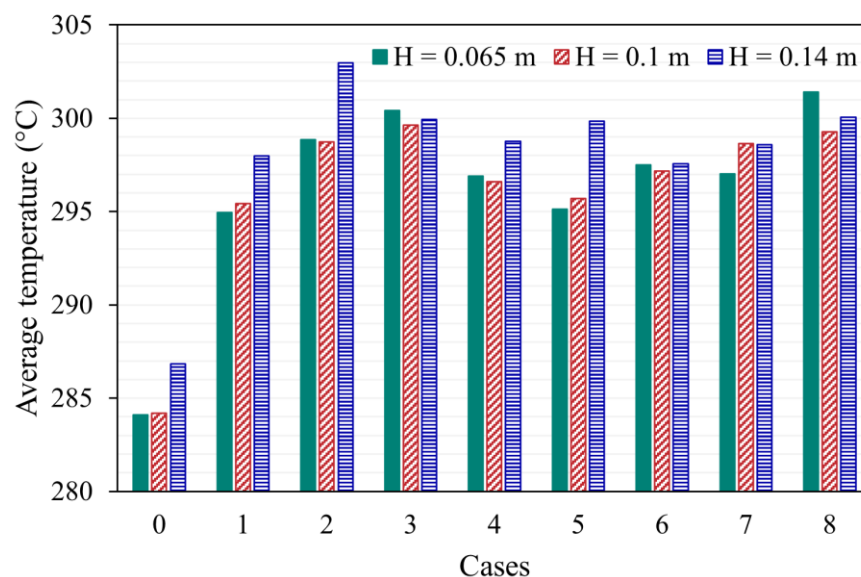


Figure 5.4 Results of the response of average solid temperature at different heights for each experimental design case.

Figure 5.5 shows the plot of the average mixing index. As previously mentioned, the tube diameter is a significant parameter that has a negative impact on the average mixing index. When the tube diameter is increased, it disrupts the flow dynamics and particle dispersion within the fluidized bed, leading to a decrease in mixing behavior and a lower mixing index. The larger tube diameters create additional space within the bed, which limits the interaction and collision between particles. Consequently, the mixing process is hindered as the particles can flow without coming into contact with each other. Moreover, the use of larger tubes can result in lower flow velocities near their vicinity, reducing the momentum and turbulence within the surrounding fluid. This diminished turbulence negatively affects the mixing of particles. In addition, the larger tubes may allow particles to pass through, leading to reducing the residence time and contact opportunities between particles. The decreased interaction time limits the chances for thorough mixing to take place. All these factors contribute to a lower mixing index and decreased mixing performance when using larger tube diameters in the fluidized bed.

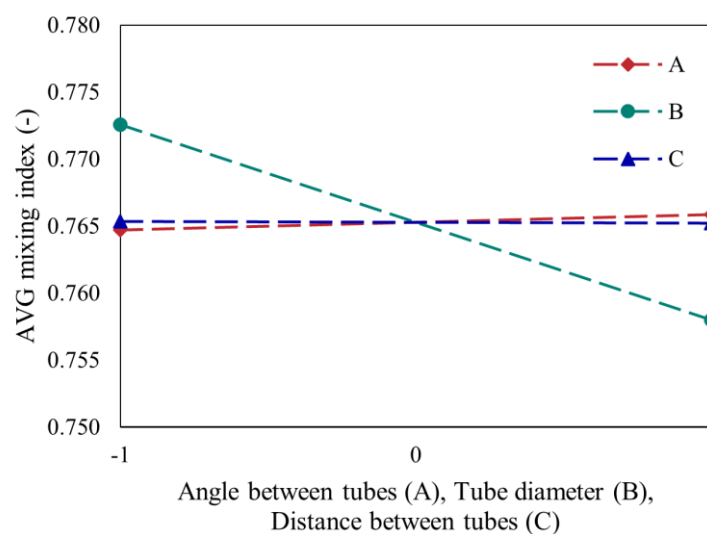


Figure 5.5 Main effect plot of the average mixing index.

Figure 5.6 depicts the average solid volume fraction in the radial direction at a height of 0.065 m. The angle between tubes and tube diameter are significant parameters that negatively affect the average solid volume fraction at this height. A decrease in the angle between tubes or a change from an in-line to a staggered tube configuration disrupts flow patterns, enhances particle dispersion, and increases particle-tube interactions. The staggered tube configuration alters the flow patterns within the bed, potentially changing the direction of particle flow and causing disruptions in the flow behavior. Consequently, particles tend to bypass or flow around the tubes, resulting in a reduced accumulation at the bottom of the bed. Additionally, the staggered tube configuration promotes better particle dispersion throughout the bed by creating additional pathways for particle movement and increasing the likelihood of particle-particle interactions. This improved dispersion prevents particles from accumulating in specific regions, including the bottom of the bed. Furthermore, the staggered tube configuration increases the number of particle-tube interactions. With more frequent contact between particles and immersed tubes, these interactions disrupt particle clustering or agglomeration at the bottom of the bed. When considering the influence of increasing the tube diameter to a larger size, it has a more significant impact on the average solid volume fraction at this height compared to changing the tube configuration. The reduction in the solid volume fraction is primarily attributed to two factors: reduced particle-particle interactions and altered flow dynamics. As mentioned earlier, larger tubes hinder the opportunities for particle-particle interactions that are crucial for promoting aggregation and cluster formation. Consequently, there is a decrease in particle clustering and accumulation at the bottom of the bed, leading to a lower solid volume fraction. Additionally, the

presence of larger tubes can result in lower flow velocities near the tubes, thereby reducing the momentum and turbulence in the surrounding fluid. This diminished fluid motion makes it more challenging for particles to accumulate at the bottom of the bed, contributing to a lower solid volume fraction.

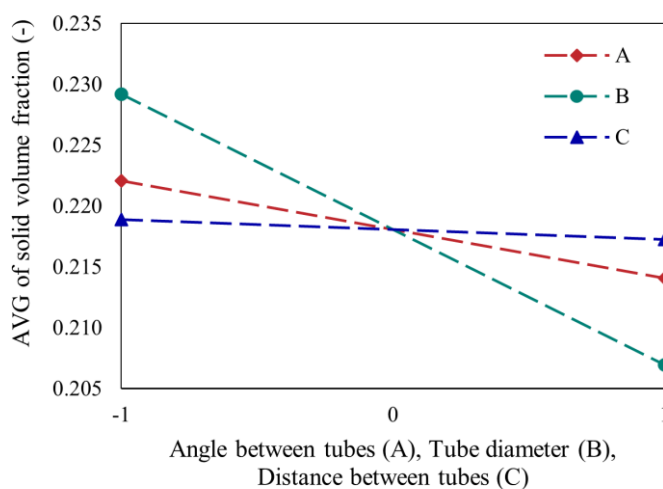


Figure 5.6 Main effect plot of the average solid volume fraction at the height of 0.065 m.

Figure 5.7 shows the plot of average solid volume fraction in the radial direction at a height of 0.1 m. All of the main parameters have a positive impact on the solid volume fraction at this height. Changing the immersed tube configuration from an in-line to a staggered configuration enhances particle dispersion and promotes better particle-tube interactions. The staggered tube configuration alters the flow patterns within the bed, changing the direction of particle flow and creating disturbances in the flow behavior. As a result, particles disperse more evenly throughout the bed, leading to better mixing and dispersion. Additionally, the staggered configuration increases the likelihood of particle-particle interactions. With

particles coming into contact with the immersed tubes more frequently, better mixing and dispersion of solid particles occur. When the tube diameter is increased, particle bypassing is reduced, and the flow dynamics are altered. The larger tube diameters result in decreased flow velocities near the tubes, reducing the tendency of particles to bypass or flow around them. This increase in particle-tube interactions and deposition leads to a higher solid volume fraction at this height. Furthermore, the presence of larger tubes can disrupt flow patterns and create disturbances that promote particle flow around the tubes, contributing to a higher solid volume fraction. Moreover, increasing the pitch length also plays a role in increasing the solid volume fraction. The larger pitch length allows particles to spend more time in the regions between the rows of tubes. This prolonged residence time enhances the chances of particle-particle interactions and particle deposition, resulting in an increased solid volume fraction at this height.

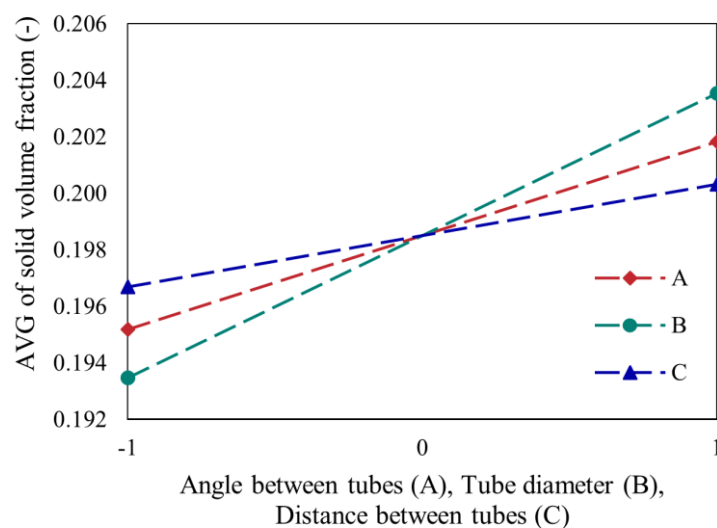


Figure 5.7 Main effect plot of the average solid volume fraction at the height of 0.1 m.

Figure 5.8 illustrates the plot of the average solid volume fraction in the radial direction at a height of 0.14 m. The angle between tubes and tube diameter have a positive effect, while the distance between tubes has a negative effect on the average solid volume fraction at this height. The reasons for the influence of the angle between tubes and tube diameter on the solid volume fraction have been previously described. However, regarding the influence of the distance between tubes, the increased spacing between tube rows 2 and 3 results in a decrease in particle-particle and particle-tube interactions. With more space between the tubes, particles have less tendency to flow around in that specific area, leading to a decrease in the solid volume fraction.

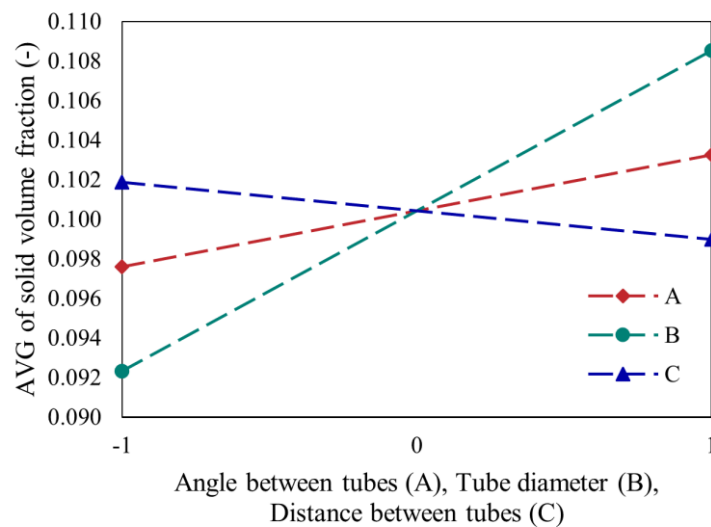


Figure 5.8 Main effect plot of the average solid volume fraction at the height of 0.14 m.

Figure 5.9 displays the plot of the average particle temperature at a height of 0.065 m. The tube diameter and the distance between tubes have a positive impact on the temperature at this height. Larger tube diameters provide a greater surface area for heat transfer between the tubes and the solid particles. The increased surface area facilitates enhanced contact and exchange of thermal energy, resulting in higher temperatures of the solid particles. In addition, a larger pitch length, which corresponds to an increased distance between adjacent tubes, plays a role in influencing the particle temperature in positive effect. This increased spacing between the tubes reduces the likelihood of particles bypassing or flowing around the tubes. Instead, particles are more likely to interact with the tubes as they pass through the gaps. This increased interaction promotes efficient heat transfer between the particles and the tubes, leading to an elevation in the solid temperature at the bottom of the bed.

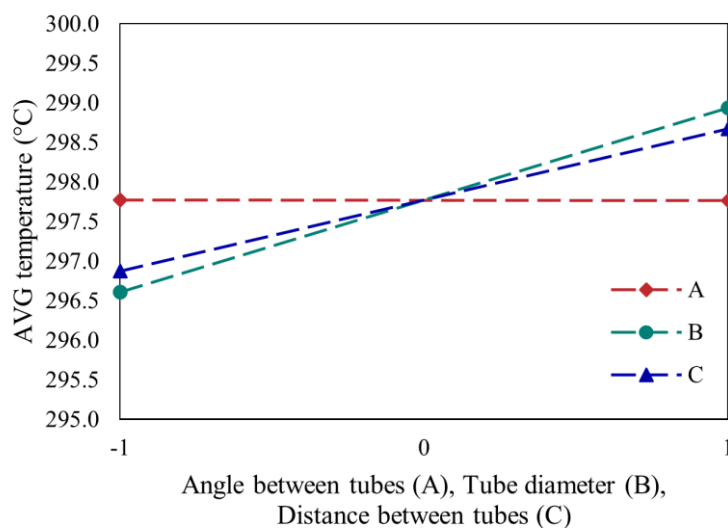


Figure 5.9 Main effect plot of the average solid temperature at the height of 0.065 m.

Figure 5.10 displays the plot of the average particle temperature at a height of 0.1 m. Both the tube diameter and the distance between tubes have a positive impact on the temperature at this height. The reasons for the influence of these parameters on the temperature increase have been previously described. Increasing the tube diameter leads to higher solid temperatures at this height due to several factors. The larger tube diameter provides more surface area for heat transfer, resulting in improved heat conduction and higher temperatures of the solid particles. In addition, the increased tube diameter enhances mixing and dispersion of the particles, facilitating better contact between the particles and the tubes, and promoting more efficient heat transfer. Similarly, larger pitch lengths also contribute to higher solid temperatures at this height. The increased residence time allows for prolonged contact between the particles and the tubes, promoting enhanced heat exchange. The larger pitch length also improves mixing and dispersion of the particles, ensuring better interaction with the tubes and facilitating effective heat transfer.

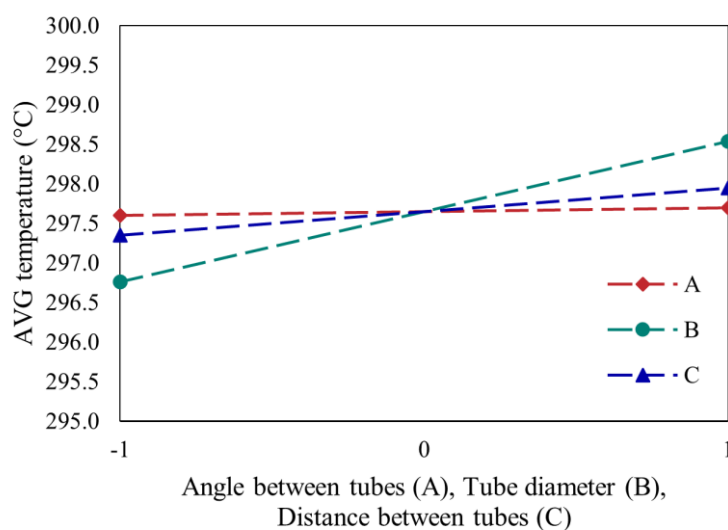


Figure 5.10 Main effect plot of the average solid temperature at the height of 0.1 m.

Figure 5.11 illustrates the average particle temperature at a height of 0.14 m. The angle between the tubes negatively affects the temperature, while the distance between the tubes positively influences the temperature change. When the arrangement is changed from an in-line to a staggered configuration, the particle flow patterns are altered, resulting in disturbances in the flow behavior. Consequently, particles tend to bypass or flow around the tubes, reducing their contact and interaction with the tubes. This decreased contact impedes the transfer of thermal energy, resulting in lower solid temperatures at the height between the immersed tubes. Moreover, the staggered tube configuration enhances particle dispersion throughout the bed. However, this dispersion can also lead to decreased particle-particle contacts in specific regions, including the space between the immersed tubes. Consequently, the opportunity for heat transfer between particles and tubes is diminished, resulting in lower solid temperatures at this height. In contrast, when the pitch length is larger, it provides more space for efficient heat exchange between the solid particles and the immersed tubes. The larger distance between tubes provides a larger surface area available for heat transfer. This increased surface area facilitates more effective heat exchange, leading to elevated solid temperatures.

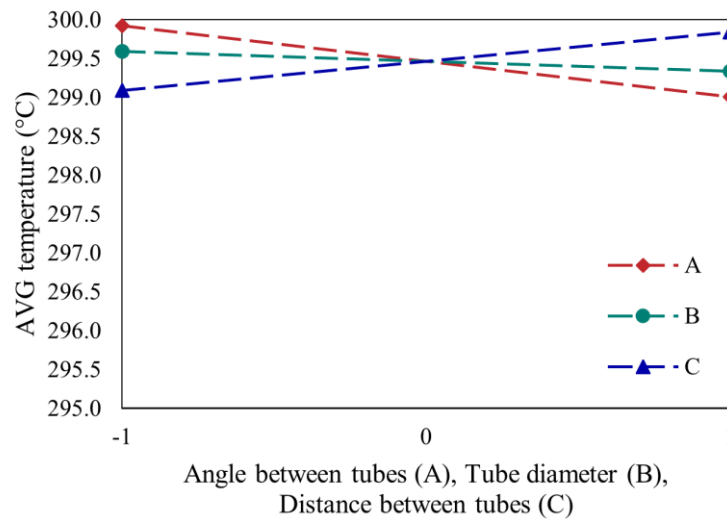


Figure 5.11 Main effect plot of the average solid temperature at the height of 0.14 m.

Based on the analysis, the adding of immersed tubes in the system leads to improved mixing behavior and heat transfer compared to the system without immersed tubes. The ANOVA analysis indicates that all cases result in better average solid volume fraction and particle temperature. However, when considering the mixing index, it is observed that Case 5, which involves an angle between tubes (A) of 45 degrees or staggered tube configuration, a tube diameter (B) of 10.3 mm, and a distance between tubes (C) or pitch length of 36.05 mm, gives a higher average mixing index compared to the other cases. Therefore, the optimal condition for this study would be Case 5.

To generalize the findings and apply them to other systems, it is beneficial to express the appropriate design parameters in terms of dimensionless quantities. In this regard, the tube diameter is divided by the width of the studied fluidized bed combustor, which is 200 mm. Similarly, the distance between the tubes is divided by the height of the potential combustion zone, which is 0.3 m. The angle between the tubes remains unchanged in dimensionless terms or determination of staggered

configuration. Therefore, an optimal condition is identified using a staggered configuration with a dimensionless tube diameter per column width of 51.5 and a dimensionless distance between tubes per height of the tube zone of 120. By expressing these parameters in dimensionless units, the findings can be applied and compared across different systems, providing valuable insights for designing similar fluidized bed combustors.

5.4.2. Effect of angle between tubes

In Figure 5.12a, the bed without an immersed tube bundle in the system is depicted. The observation reveals the generation of small bubbles randomly at the bottom of the bed, followed by their upward movement. During this rising process, interactions occur between neighboring bubbles. The instability of the bubble boundary leads to frequent coalescence of bubbles, both vertically and laterally, resulting in larger bubbles in the upper region of the system. In addition, some particles are entrained into the wake of the formed bubble at the bed bottom and also rise upward. The solid particles exhibit vigorous upward motion primarily in the central region of the bed, particularly in the dome and wake of the bubble phase. Once the bubble phase erupts at the top region, the particles disperse into the free domain of the bed, causing intense downward flow near the bed wall [121].

The hydrodynamics and heat transfer in the fluidized bed with immersed tubes for mixed biomass and silica sand are significantly influenced by different tube configurations, as depicted in Figure 5.12b and c. One notable effect is the splitting of bubbles into smaller ones when immersed tubes are present. The tube bundle restricts the growth of bubbles, resulting in smaller bubble sizes throughout the bed compared

to the system without tubes. The presence of small bubbles is more uniform in the system. It is evident that the immersed tubes are consistently surrounded by particles. Occasionally, a stagnant cap forms at the top region of each tube, but it is quickly swept away by rising bubbles. Moreover, particles in the leading edge of the bubble change direction upon colliding with the tube surface and then descend through the bubble, leading to intense collisions between the falling particles and the upward-moving particles in the wake of the bubble. The difference between using in-line and staggered configurations lies in the level of turbulence and complexity in the flow. The staggered configuration results in a more turbulent and intricate flow, leading to enhanced dispersion of particles throughout the bed. This configuration introduces disturbances in the flow pattern, altering the direction and distribution of particle flow. On the other hand, the flow of particles between the tubes in the in-line configuration is relatively smoother, causing less disruption to the overall fluidization behavior [122, 123].

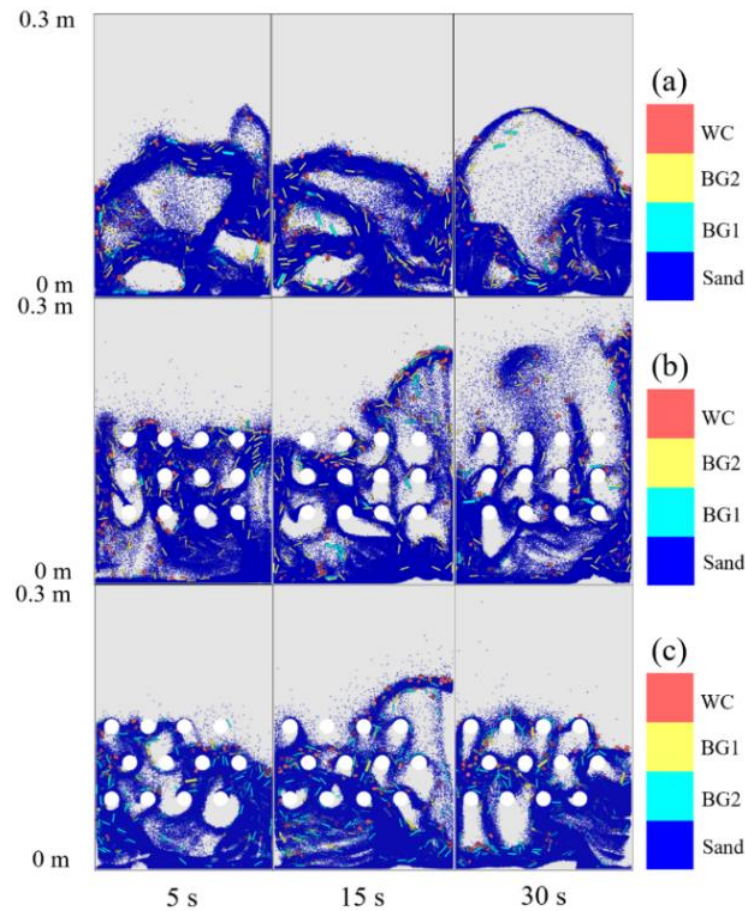


Figure 5.12 Qualitative comparison of the flow patterns in the system with different tube configurations, including (a) no-tube, (b) in-line, and (c) staggered.

When examining the solid volume fraction at different heights in Figure 5.13, it is observed that the case with a tube bundle exhibits higher solid volume fractions at the heights of 0.1 m and 0.14 m. However, at the heights below and above the tube bundle, specifically at 0.065 m and 0.175 m, the case without a tube bundle shows higher solid volume fractions. This indicates that the presence of the tube bundle assists in enhancing the concentration of particles in the combustion zone, particularly at the height corresponding to the interval between rows of tubes. Nonetheless, upon analyzing Figure 5.14, it is evident that the mixing indexes with respect to time for all cases do not differ significantly. Once dynamic mixing equilibrium is established, the

mixing index fluctuates around a constant value, representing the micro-mixing process. Nevertheless, the influence of tube configuration on the mixing intensity is not prominent in the present study, primarily due to the limited size of the investigated domain.

Furthermore, the addition of immersed tubes in the fluidized bed system also improves heat transfer by facilitating increased contact and interaction between the particles and the tubes. The in-line configuration, with its straight arrangement, provides a larger contact area between the tubes and the particles. This enhances heat conduction and transfer, enabling efficient heating or cooling of the particles in direct contact with the tubes. On the other hand, the staggered configuration, with its disrupted flow pattern, promotes better heat transfer throughout the bed. The altered flow direction and increased turbulence improve particle-fluid and particle-particle contact, leading to enhanced heat exchange. The staggered arrangement increases the chances of particles coming into contact with the immersed tubes, facilitating efficient heat transfer. However, when examining the particle temperature in Figure 5.15, it can be observed that the particle temperature for these tube configurations does not differ significantly. This can be attributed to the efficient mixing behavior indicated by the mixing index. When the mixing behavior is efficient, it has the potential to lead to good heat transfer behavior, resulting in similar particle temperatures regardless of the specific tube configuration.

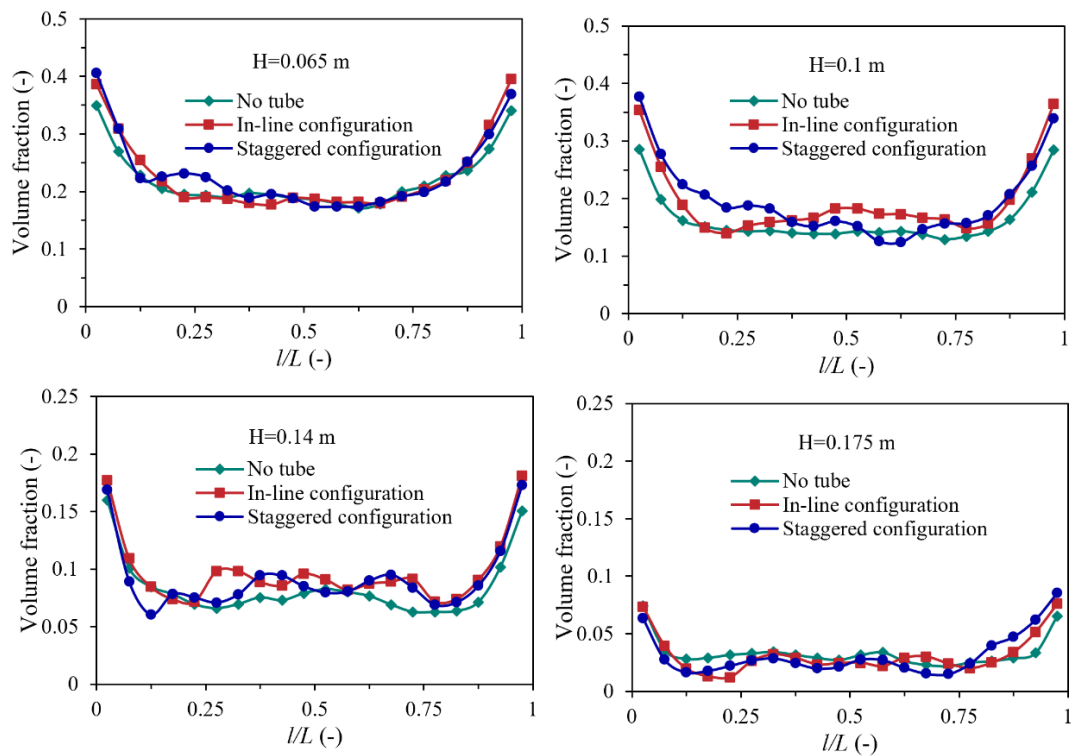


Figure 5.13 Profile comparison of the time-averaged solid volume fraction in the systems with different tube configurations.

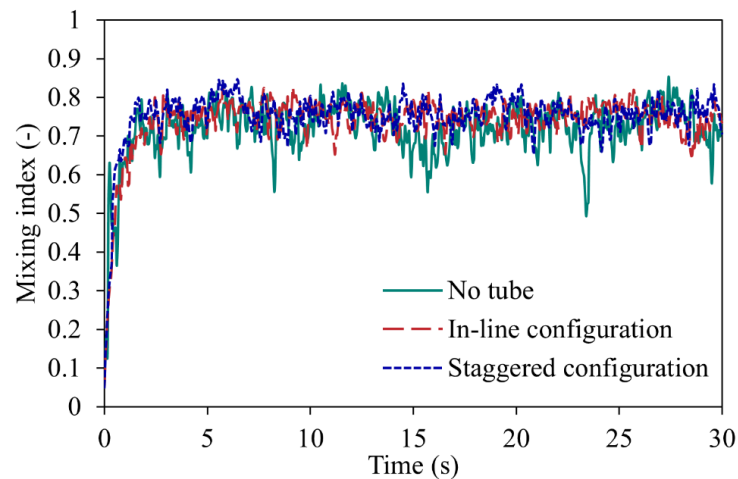


Figure 5.14 Time evolutionary profiles of the mixing index in the systems with different tube configurations.

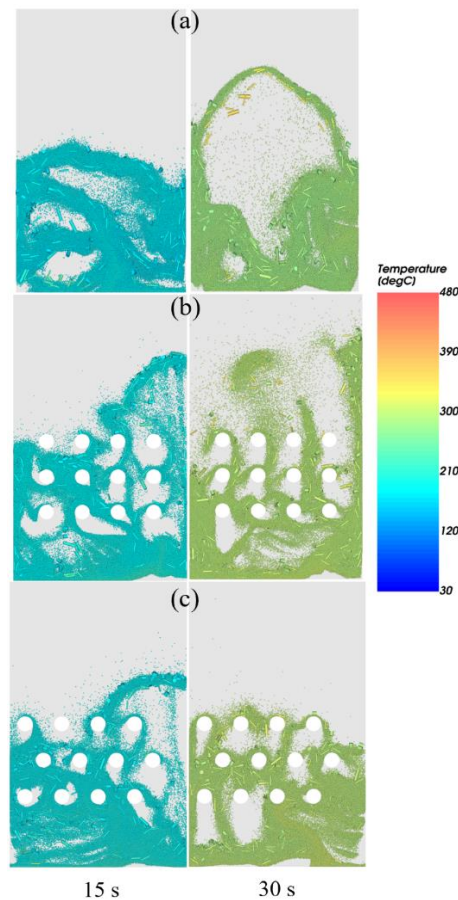


Figure 5.15 Contour plot of solid temperature at different times in the system with different tube configurations, including (a) no-tube, (b) in-line, and (c) staggered.

5.4.3. Effect of tube diameter

As mentioned earlier in the previous section regarding the impact on mixing behavior and heat transfer in the system, the effect of different tube diameters on the solid volume fraction at various heights is examined in Figure 5.16. The results reveal that using a larger tube diameter of 17.1 mm results in a denser concentration of particles compared to a diameter of 10.3 mm, except at the height of 0.065 m, which is the lower region of the tube bundle. The larger tube diameters bring about changes in the distribution of gas and solid particles, affecting bubble formation, movement,

and interaction. However, in Figure 5.17, it is shown that the mixing indexes over time for all tube diameters exhibit no significant differences. The impact of tube diameter on the mixing intensity is not prominently observed in the current study, primarily due to the limited size of the investigated domain. Nevertheless, when examining the average mixing index, it is observed that smaller tube diameters tend to enhance the mixing and dispersion of solid particles in the bed. The increased space between the tubes promotes particle-particle interactions and collisions, leading to improved mixing of the particles.

When examining the particle temperature in Figure 5.18, it can be observed that the particle temperature does not vary significantly for the different tube diameters. This can be attributed to the efficient mixing behavior indicated by the mixing index. When mixing is efficient, it has the potential to facilitate good heat transfer behavior, resulting in similar particle temperatures regardless of the specific tube diameter. Although larger tube diameters may provide a larger surface area for heat transfer, allowing for more efficient exchange of thermal energy between the tubes and particles, it does not necessarily guarantee higher solid temperatures. In some cases, larger tube diameters can reduce the contact area and impede heat transfer, resulting in lower energy transfer. Overall, while tube diameter can have an impact on heat transfer rates and solid temperatures, the observed results suggest that the efficient mixing behavior plays a more significant role in determining the particle temperatures in the system.

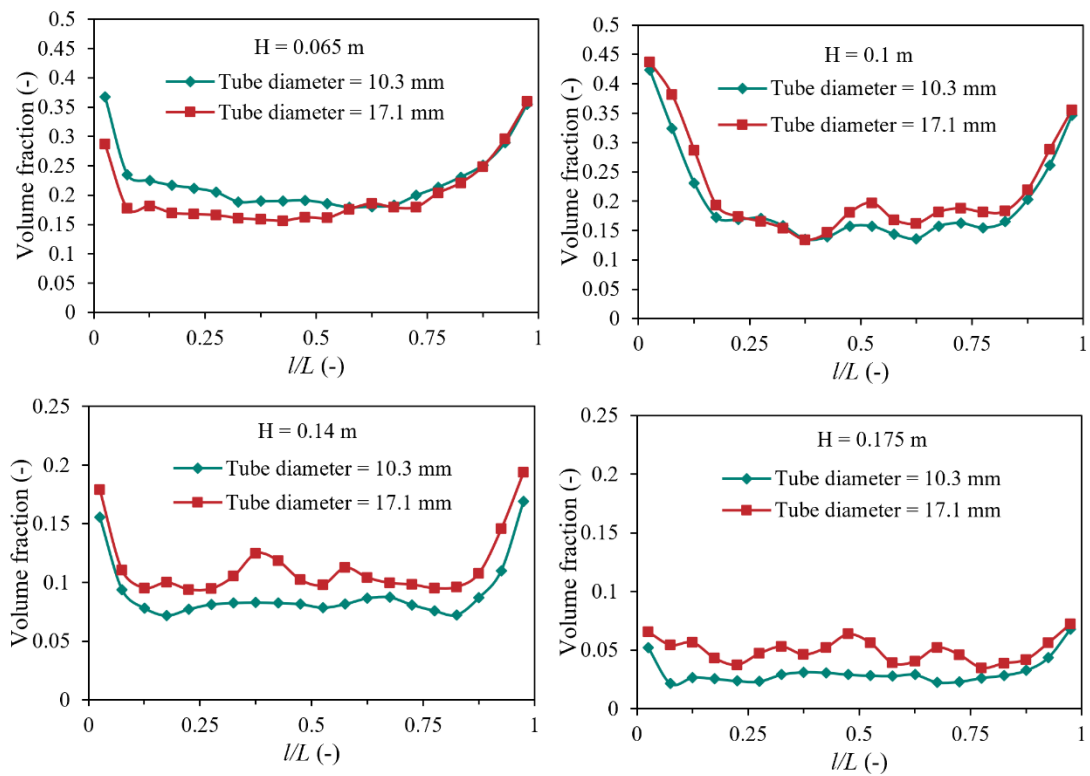


Figure 5.16 Profile comparison of the time-averaged solid volume fraction in the systems with different tube diameters.

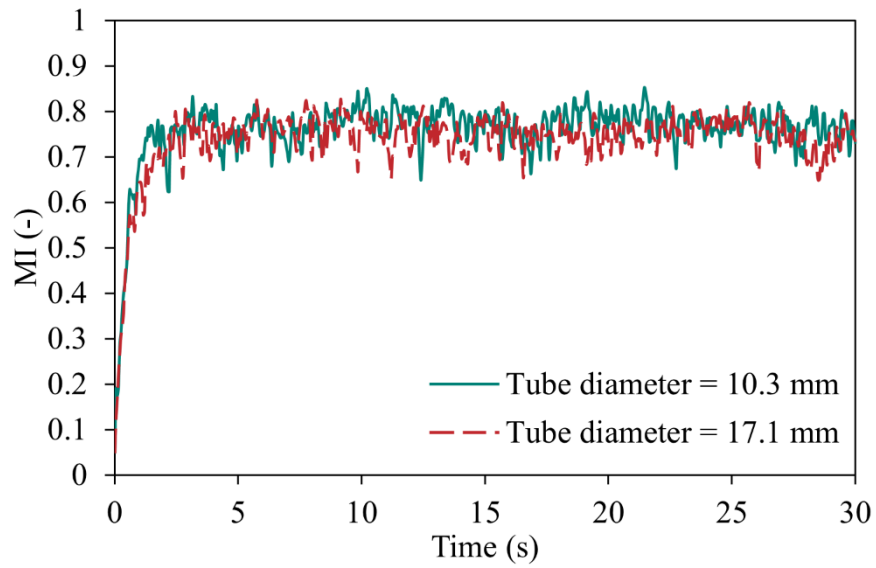


Figure 5.17 Time evolutionary profiles of the mixing index in the systems with different tube diameters.

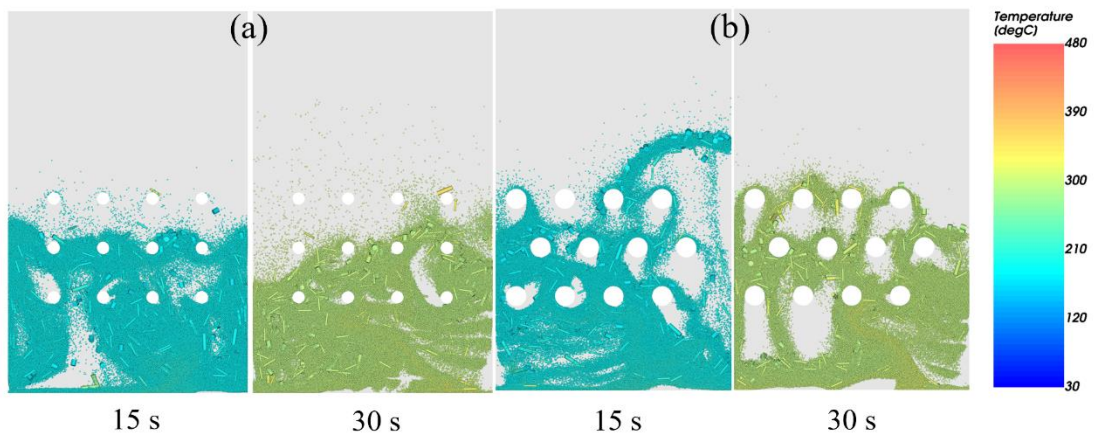


Figure 5.18 Contour plot of solid temperature at different times in the system with different tube diameters of (a) 10.3 and (b) 17.1 mm.

5.4.4. Effect of distance between tubes

Figure 5.19 illustrates the investigation of the impact of different distances between tubes, or pitch lengths, on the solid volume fraction at various heights. The results indicate that the solid volume fraction does not exhibit significant variations for the two pitch lengths at all heights. In fact, increasing the spacing between tubes reduces interactions between particles and between particles and tubes. With a greater distance between tube rows, particles have a lower tendency to flow around that specific area, resulting in a decrease in the solid volume fraction. However, it is important to note that the specific effects may differ depending on other system parameters, such as the angle between tubes or tube diameter. Additionally, the mixing behavior, as indicated by the mixing index, is also influenced by the pitch length. Figure 5.20 demonstrates that the mixing indexes remain relatively consistent over time for different pitch lengths. This suggests that the mixing intensity is not significantly affected by the pitch length within the investigated domain.

In the analysis of heat transfer, the average particle temperature at different heights shows some influence from the pitch length, as depicted in Figure 5.21. However, the particle temperature does not exhibit significant variations for different pitch lengths. This can be attributed to the efficient mixing behavior indicated by the mixing index. When mixing is efficient, it has the potential to facilitate effective heat transfer, resulting in similar particle temperatures regardless of the specific pitch length. Furthermore, it should be noted that the investigation of pitch length effects may have been conducted within a relatively small domain. In such cases, the changes in hydrodynamics, mixing behavior, and heat transfer caused by variations in pitch length may not be pronounced. The impact of pitch length is more likely to be

noticeable in larger-scale systems, where differences in flow patterns and particle interactions become more prominent.

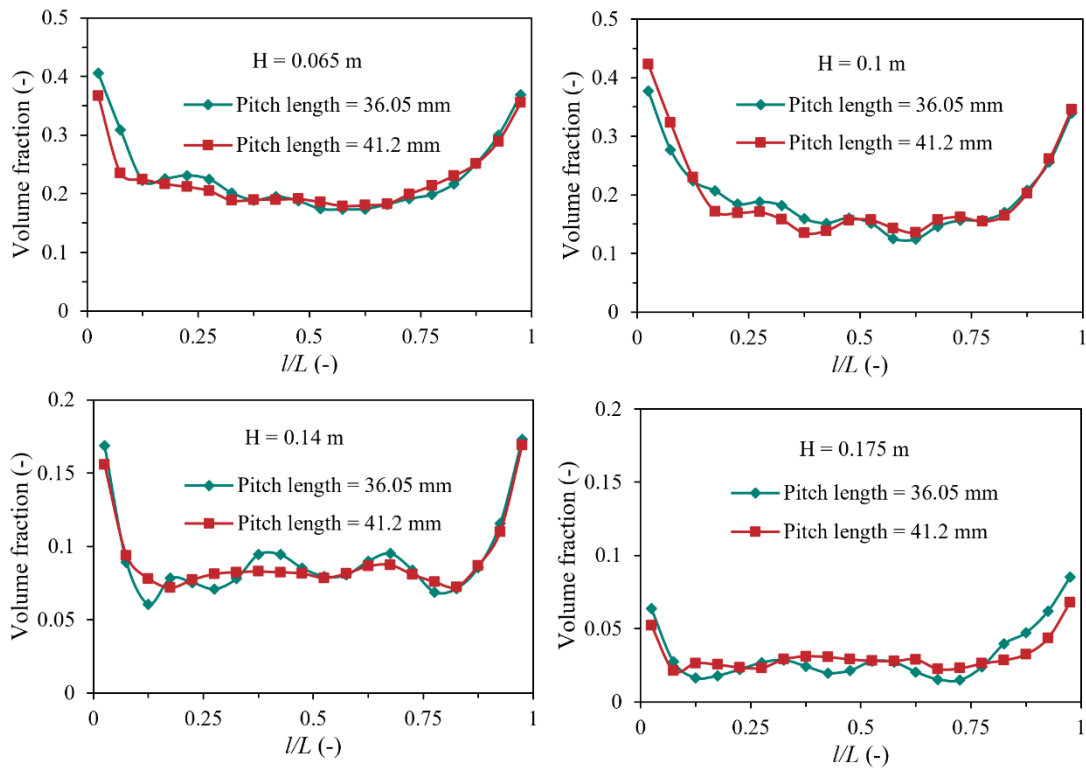


Figure 5.19 Profile comparison of the time-averaged solid volume fraction in the systems with different distance between tubes.

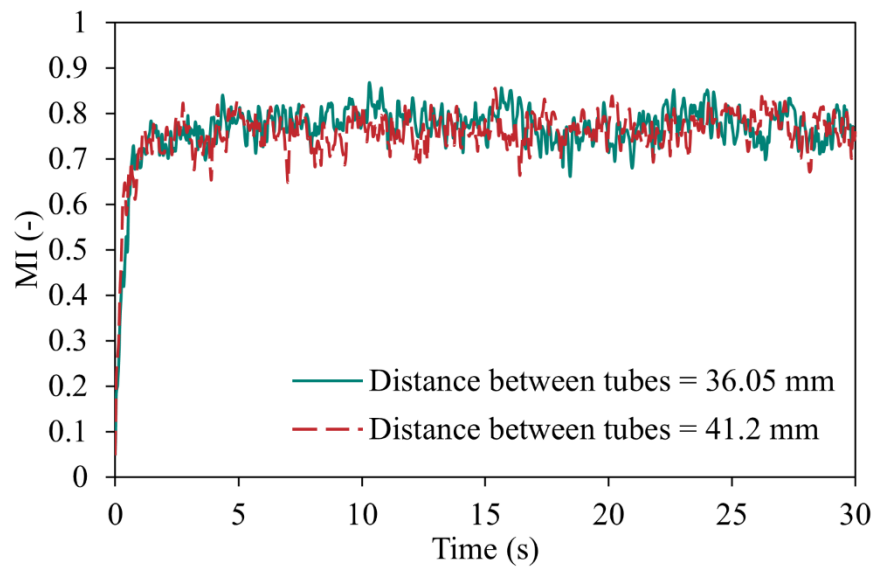


Figure 5.20 Time evolutionary profiles of the mixing index in the systems with different distance between tubes.

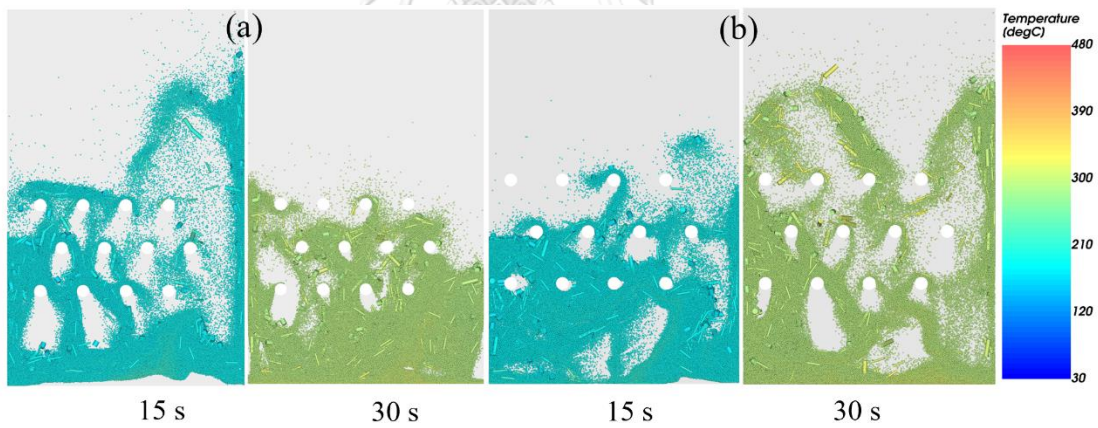


Figure 5.21 Contour plot of solid temperature at different times in the system with different distance between tubes of (a) 36.05 and (b) 41.2 mm.

5.4.5. Heat transfer coefficient analysis

The analysis of the heat transfer coefficient provides valuable insights into the heat transfer characteristics and performance of a system. It involves evaluating the rate at which heat is transferred between the fluid and solid phases, typically expressed in terms of a coefficient. Figure 5.22 illustrates the spatial distribution of the time-averaged surface-to-bed heat transfer coefficient, specifically focusing on convective heat transfer mechanisms around the immersed tube at a height of 0.1 m. Different tube diameters are considered in this analysis. The figure shows that the heat transfer coefficient around the tube is influenced by the tube diameter. It can be observed that in cases where a larger tube diameter is used, the majority of the heat transfer coefficient values around the tube are lower compared to the cases with smaller tube diameters. A higher heat transfer coefficient indicates a greater rate of heat transfer between the fluid and solid phases. This implies that heat is being transferred more efficiently, leading to a faster exchange of thermal energy. However, it is important to note that the relationship between tube diameter and heat transfer coefficient may not be straightforward. The findings from Figure 5.10 indicate that increasing the tube diameter can result in higher solid temperatures. This can be attributed to the dominance of heat conduction in the thermal boundary layer, in addition to convective heat transfer from the fluid. The contact heat transfer between the particles and the tube wall is directly related to the solid volume fraction. Generally, a higher particle concentration corresponds to a higher heat transfer coefficient, as more heat is exchanged between the particles and the wall per unit time and unit wall area. This aligns with the results from Figure 5.7, which show an increase in solid volume fraction when larger tube diameters are used. Nonetheless,

the heat transfer coefficient analysis focuses on the convective heat transfer rate specifically around the tubes, which tends to be lower in the case of using smaller tube compared to the overall heat transfer rate within the system. It is worth noting that the heat transfer coefficient is inversely proportional to the tube diameter. Therefore, when considering the system as a whole, the heat transfer rate may actually be higher in the case of using a larger tube diameter, resulting in higher particle temperatures as observed in Figure 5.10. Overall, the analysis of the heat transfer coefficient plays a vital role in understanding heat transfer performance. It emphasizes that evaluating the average particle temperature alone is insufficient for assessing heat transfer efficiency. By considering the heat transfer coefficient, researchers can gain a deeper understanding of the complex interactions between the fluid, particles, and tube wall, enabling them to optimize heat transfer performance in the system.

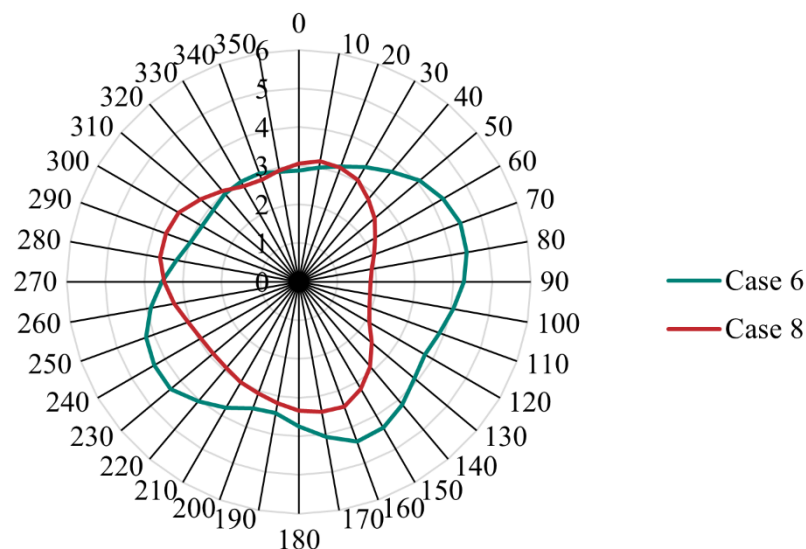


Figure 5.22 the spatial distribution of the time-averaged (26-30 s) surface-to-bed heat transfer coefficient, specifically focusing on convective heat transfer mechanisms around the immersed tube at a height of 0.1 m.

5.4.6. Advantages and limitations related to actual operation

According to the study findings, the addition of immersed tubes in the bubbling fluidized bed combustor significantly affects the hydrodynamics and heat transfer in the mixed biomass and silica sand mixture. The presence of immersed tubes influences the flow pattern, turbulence, and particle dispersion within the bed. The tube configuration, whether in-line or staggered, impacts the flow behavior between the tubes, with the in-line configuration providing a smoother flow and the staggered configuration promoting better particle dispersion throughout the bed. This enhances mixing behavior and improves overall fluidization. In terms of heat transfer, immersed tubes provide an increased surface area for thermal energy exchange between the tubes and particles. This facilitates more efficient heat transfer, allowing for the exchange of thermal energy from the particles to the surrounding fluid. The enhanced heat transfer rates lead to higher solid temperatures and improved overall heat transfer performance within the system. Moreover, the flow behavior and heat transfer in the presence of immersed tubes can influence bubble breakage or coalescence and the heat transfer coefficient. The tube configuration and spacing affect the path and interaction of bubbles with the tubes. Changes in flow behavior can result in altered bubble dynamics, with the tubes acting as obstacles or barriers that can cause more frequent bubble breakage or coalescence upon contact. This, in turn, impacts heat transfer within the bed. In addition, the heat transfer coefficient, which quantifies the rate of heat transfer between the fluid and solid phases, is influenced by flow behavior, bubble dynamics, and particle distribution. The spacing and arrangement of immersed tubes influence flow dynamics and particle dispersion, ultimately impacting the heat transfer performance. Changes in bubble behavior affect

the contact time and surface area available for heat transfer, thus influencing the heat transfer coefficient. Therefore, the presence of immersed tubes alters flow behavior, bubble dynamics, bubble breakage or coalescence, and the heat transfer coefficient in a bubbling fluidized bed system. Furthermore, the enhanced mixing and heat transfer contribute to improved combustion efficiency in systems that include a reaction model. The thorough mixing of the biomass and silica sand mixture ensures uniform contact between the fuel and oxygen, promoting complete combustion and reducing the formation of undesirable by-products. This results in higher energy conversion and reduced emissions.

However, there are limitations to consider regarding the addition of immersed tubes into the system, especially when it comes to actual operation. These limitations include design and operational constraints that need to be taken into account. The placement and arrangement of the tubes must be carefully considered to ensure optimal flow dynamics and particle dispersion within the bed. It is also important to control operational conditions such as fluidization velocity and temperature within specific ranges to maintain stable and efficient operation. Additionally, changes in flow behavior can result in increased pressure losses, which should be considered during system design to ensure proper operation and efficiency. Another limitation is the possibility of tube fouling and blockage over time. The particles flowing through the system can deposit on the tube surfaces, leading to fouling and reduced heat transfer efficiency. Regular cleaning and maintenance procedures are necessary to prevent or mitigate this issue. Moreover, the integration of immersed tubes may require additional considerations and specialized equipment, which can increase the overall system cost and complexity. Proper engineering practices and maintenance

strategies are essential to ensure reliable and cost-effective operation. In summary, while the addition of immersed tubes offers benefits in terms of improved hydrodynamics and heat transfer, these advantages must be carefully weighed against the associated limitations and considerations in actual operation. Proper planning, design, and maintenance strategies are crucial to optimize the performance and reliability of the system, addressing the design and operational challenges to achieve efficient and reliable performance.

On the other hand, If the system incorporates a combustion or reaction model, several important factors need to be considered. Thorough mixing of the fuel and oxidizer within the bed is crucial for promoting complete combustion and minimizing the formation of undesirable by-products. Efficient fuel-oxidizer mixing should be a focus during the design phase to maximize combustion efficiency. Additionally, controlling the bed temperature is essential to ensure stable combustion and prevent issues such as thermal runaway or incomplete combustion. The heat transfer processes, including convective heat transfer between the fluidized particles and immersed tubes, should be accurately modeled in the reaction model. Monitoring and controlling the temperature distribution and gradients within the bed are necessary for optimal combustion conditions. For industrial or environmental applications, the combustion or reaction model should address the formation and control of emissions and particulate matter. The reaction model should incorporate mechanisms to predict and mitigate the formation of pollutants, either through optimizing operational parameters or implementing additional control measures. These considerations enable accurate prediction and control of combustion behavior, leading to efficient and environmentally friendly system operation.

5.5. Conclusion

This chapter primarily investigated the influence of design parameters related to immersed tubes, specifically the angle between tubes, tube diameter, and distance between tubes, in a mixed biomass fluidized bed combustor. The 2^k factorial design was employed to analyze the main effects and interactions of these parameters on the mixing behavior, solid volume fraction, and particle temperature. The main conclusions drawn from this chapter are as follows:

(1) Based on the analysis using the 2^k factorial design, the angle between tubes and tube diameter are identified as the primary influential factors across all studied variables. Furthermore, when considering the interaction between these parameters, it is determined that Case 5, which consists of an angle between tubes of 45 degrees, a tube diameter of 10.3 mm, and a distance between tubes of 36.05 mm, represents the optimal condition for this study based on the average mixing index. In addition, for a general case, an optimal condition has been identified using a staggered configuration with a dimensionless tube diameter per column width of 51.5 and a dimensionless distance between tubes per height of the tube zone of 120.

(2) The inserting of immersed tubes in the system is observed to improve both mixing behavior and heat transfer in comparison to the system without immersed tubes. The choice of a staggered tube configuration has a notable impact on the flow pattern, turbulence, and particle dispersion within the bed, leading to improved particle dispersion throughout the bed. On the other hand, the in-line configuration results in a smoother flow between the tubes. The presence of immersed tubes can also alter bubble dynamics and subsequently impact the occurrence of bubble breakage or coalescence, which in turn affects the heat transfer coefficient in the system.

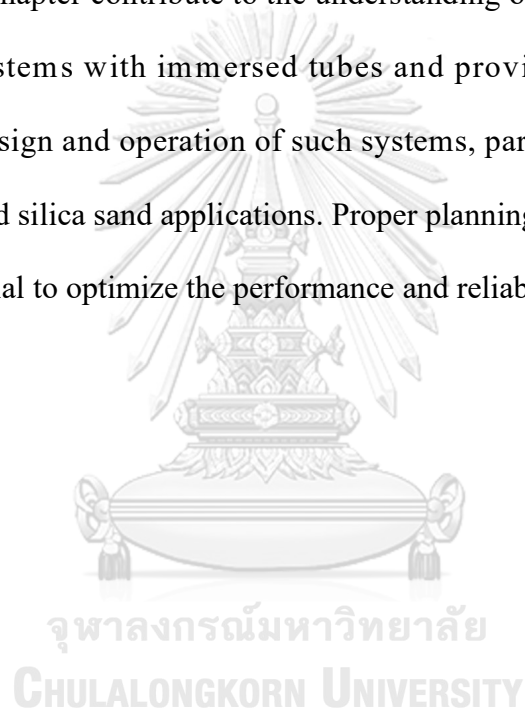
(3) The tube diameter is found to be a significant factor in the system. Larger tube diameters offer a larger surface area, facilitating more efficient heat transfer by allowing for increased contact between the tubes and the particles. However, despite the potential for improved heat transfer, the particle temperature does not vary significantly for different tube diameters. This can be attributed to the efficient mixing behavior, as indicated by the mixing index, which results in similar particle temperatures regardless of the specific tube diameter.

(4) Regarding the distance between tubes, it is observed that it does not exert a significant influence on the hydrodynamics, mixing behavior, and heat transfer within the investigated domain. Although changes in pitch length affect particle-particle and particle-tube interactions, the overall impact on the solid volume fraction, mixing index, and particle temperature is not substantial.

(5) The heat transfer coefficient around the tube tends to be higher when using a smaller tube diameter. However, the relationship between tube diameter and heat transfer coefficient is influenced by factors such as the solid volume fraction around the tube, which is associated with the dominance of heat conduction. To comprehensively assess the heat transfer performance, it is crucial to consider both convective and conductive heat transfer mechanisms within the system. By taking into account these factors, a more accurate evaluation of the system's heat transfer characteristics can be achieved.

It is important to acknowledge that the effects of these factors may vary depending on other system parameters. Additionally, the investigations conducted in this study were limited to a relatively small domain, which may have constrained the observable changes in hydrodynamics and heat transfer. Further research conducted

on larger-scale systems would offer more comprehensive insights into the influence of these factors. However, while the addition of immersed tubes can offer benefits in terms of improved hydrodynamics and heat transfer, these benefits need to be balanced against the associated limitations and considerations in actual operation. Design and operational constraints, potential tube fouling, and additional equipment and complexity with cost are important aspects to consider. Overall, the findings presented in this chapter contribute to the understanding of the intricate dynamics in fluidized bed systems with immersed tubes and provide valuable insights for optimizing the design and operation of such systems, particularly in the context of mixed biomass and silica sand applications. Proper planning, design, and maintenance strategies are crucial to optimize the performance and reliability of the system.



CHAPTER 6

DATA-DRIVEN MODEL FOR PREDICTING MIXING BEHAVIOR AND TEMPERATURE IN A BUBBLING FLUIDIZED BED COMBUSTOR WITH IMMERSED TUBES

The bubbling fluidized bed combustor is extensively utilized in various industries due to its numerous benefits, including effective mixing, high rates of heat transfer, and the ability to handle a wide range of materials. The operational conditions and design parameters of a bubbling fluidized bed can be adjusted to meet specific process or application requirements. By incorporating immersed tubes into the system, efficient heat transfer and combustion can be achieved within a compact setup. This design feature provides a larger surface area for heat exchange, contributing to improved combustion efficiency and reduced emissions. Such a configuration is commonly employed in applications that demand high thermal efficiency and fuel flexibility, such as coal-fired power plants and biomass combustion systems. However, practical operations in industries often involve particles with varying sizes and densities, leading to complex mixing and heat transfer phenomena among different components. Additionally, the timely prediction of process behavior is crucial for industry applications. Therefore, it is essential to comprehend and predict fluidization behaviors to effectively control and optimize mixing and combustion efficiency in a timely manner [124].

In order to study the mixing behavior and heat transfer in a bubbling fluidized bed combustor with immersed tubes, coupled CFD-DEM simulation techniques can be used. However, these simulations are computationally expensive and time-consuming. To address this issue, this chapter proposes a hybrid model framework

that achieves faster results with significantly lower computational costs. Machine learning techniques provide a better understanding of various physical phenomena. Data-driven machine learning methods, in particular, serve as black-box models that do not rely on governing equations to describe the phenomena. These methods can play a crucial role in achieving faster predictions with minimal computational resources. This is possible because machine learning models have an inherent capability to establish relationships between variables using available datasets. In recent times, machine learning tools have garnered increasing attention due to their high prediction accuracy and their ability to reduce the need for extensive experimental and computational efforts [125]. In addition to utilizing regression models, researchers have widely employed artificial neural network (ANN) models, among various machine learning techniques, to predict the hydrodynamic characteristics, mixing behavior, and heat transfer in fluidized bed reactors [61, 126-132]. However, only a limited number of studies have focused on predicting the mixing behavior and temperature of a mixture consisting of mixed biomass and silica sand in the bubbling fluidized bed with immersed tubes.

In this chapter, a data-driven model based on CFD-DEM simulations is developed. The improved model uses data obtained from the CFD-DEM simulations conducted in Chapter 5. The specific objective of this study is to utilize the high-fidelity data from the CFD-DEM model to predict the mixing behavior and temperature of in the mixed biomass bubbling fluidized bed with immersed tubes, while significantly reducing the computational expenses associated with conducting CFD-DEM simulations.

6.1. Dataset buildup from CFD-DEM simulations for model development

This chapter uses a dataset derived from a series of CFD-DEM simulations conducted in Chapter 5. The simulations focus on studying the behavior of mixed biomass and silica sand in a bubbling fluidized bed combustor with immersed tubes, using a 2^k factorial design approach. The previous chapter provided detailed information about the model employed. The model development process is divided into two parts: the Response Surface Methodology (RSM) model and the Artificial Neural Network (ANN) model. To capture particle information in different spatial dimensions for the ANN model development, geometry is considered up to the height of 0.4 m. It is then divided into 40 layers along the height, with each layer having a thickness of 0.03 m. The particle information, including solid volume fraction and solid temperature, is averaged within each layer, and used as input data for the machine learning model. For the solid volume fraction and solid temperature, data from the time interval of 20-30 seconds are used, considering that the total simulation time for each case was 30 seconds, with data output occurring at a time step of 0.05 seconds. On the other hand, the prediction of the mixing index is evaluated throughout the entire simulation time.

Table 6.1 presents the input variables for the neural networks, which include the angle between tubes (α), the tube diameter per column depth (d_i/y), the distance between tubes per column width (l/x), the height per column height (h/z), and the sampling time per total time (t_s/t). The output variables for prediction, as shown in Table 6.1, consist of the mixing index, solid volume fraction, and solid temperature. The first three input variables are specifically related to the design parameters of the immersed tubes, as examined in Chapter 5. Furthermore, the behavior of the system

may vary based on different heights and time, hence the selection of the last two variables. In addition, all input variables, except for the angle between tubes, are expressed in dimensionless terms to facilitate application in future work. Furthermore, based on the recommendations from previous studies, it is suggested that scaling (normalization) of both independent and dependent variables could facilitate the training process and lead to improved outcomes. Consequently, in the present study, both the independent and dependent variables are normalized within the range of [0, 1].

Table 6.1 Input and output variables of neural networks.

Variable to ANN model	Value range
<i>Input variable</i>	
Angle between tube (α , °)	0, 45
Tube diameter/Column depth (d/y , -)	0.3433, 0.855
Pitch length/Column width (l/x , -)	0.1803, 0.206
Height/Column height (h/z , -)	0-0.4
Sampling time/Total time (-)	0-1
<i>Output variable</i>	
Mixing index (MI, -)	0.0461-0.8666
Solid volume fraction (SVF, -)	0-0.5606
Solid temperature (T_p , °C)	220.78-360.98

6.2. Response Surface Methodology model

Response Surface Methodology (RSM) is a statistical and mathematical technique used to identify the optimal conditions for achieving desired outcomes. It is commonly applied in experimental design and analysis to understand the relationship between input variables and output responses, often through regression analysis. The models can be linear, quadratic, or higher order, depending on the complexity of the system. RSM enables the exploration and optimization of multiple factors simultaneously, considering both linear and non-linear effects. It provides valuable insights into the interactions and influences of different variables in a system [133].

Based on the CFD-DEM results and the statistical analysis conducted in Chapter 5, regression models are constructed to represent the relationship between the input variables and the output responses. These models are subsequently analyzed to determine significant factors, evaluate their individual and combined effects, and identify the optimal conditions for achieving the desired responses. The analysis is carried out using ANOVA, as described in the previous chapter. In this chapter, the regression models are employed to predict the output responses, including the average mixing index, average solid volume fraction at different heights, and average solid temperature at different heights. The input variables considered in the models are the same variables used in ANOVA, namely the angle between tubes, tube diameter, and distance between tubes. The predictions generated by the regression models are then compared to the CFD-DEM results obtained in Chapter 5.

6.3. Artificial Neural Network model

ANNs are machine learning algorithms that are particularly well-suited for addressing multi-variable nonlinear problems. The use of ANNs extends across a wide range of fields, including pattern recognition, process simulations, and function approximations. ANNs employ an interconnected network of nodes, resembling the behavior and learning methods of neurons in the human brain, to map input and output data. These networks serve as universal approximators and make predictions based on available historical working data. In comparison to other data-based methods, ANNs are capable of handling the intricate nature of nonlinear data by training multi-layer neural networks. The procedure is versatile and not restricted by the number of input and output parameters or the type of datasets. Among the types of networks, feed-forward ANNs are the most commonly reported and widely used approach in the field of fluidization [134].

This study employs the construction of three separate neural network models for prediction purposes. The architecture of the ANN is shown in Figure 6.1, comprising three layers: input, hidden, and output layers. The dataset is divided in a ratio of 70:15:15, where 70% of the data are allocated for training, 15% for validation, and the remaining 15% for testing. During the data training process, the weights and biases of the network are optimized to minimize the network error between the predicted and target outputs [135]. The Levenberg-Marquardt training algorithm is employed to adjust the parameters, weights, and biases during the training stage. The adjustments of the weights and biases in this algorithm allow it to have a fast convergence rate, enabling it to reach the desired level of accuracy in a shorter time compared to other training methods. Moreover, this algorithm often leads to more

accurate predictions by effectively fitting complex patterns in the data and capturing non-linear relationships between input and output variables [136, 137]. The hidden layer consists of neurons, with each neuron employing a mathematical model to determine its output based on the input. The aim of the algorithm is to estimate the optimal values of weights and bias terms, aiming to minimize the error function. To avoid excessive complexity in calculations, each architecture utilizes a single hidden layer.

The output layer is responsible for generating the prediction data. Different types of activation functions, such as tan-sigmoid, log-sigmoid, and radial-basis, are experimented with in the hidden and output layers to achieve improved prediction accuracy. The trained machine learning model is comprehensively evaluated by assessing the training results and comparing performance using quantitative indices, including the correlation coefficient and three statistical indicators (R^2 , MSE, and AARD%). Furthermore, the prediction results of the trained models are compared against the CFD-DEM results to verify the accuracy of the model predictions. It should be noted that the R^2 value represents the proportion of variation in the dependent variable that can be explained by the independent variables. Higher R^2 values indicate better prediction performance. On the other hand, the MSE (Mean Squared Error) quantifies the average magnitude of the errors. Meanwhile, the AARD% (Absolute Average Relative Deviation) measures the percentage of the average magnitude of errors in the predictions, irrespective of their direction. Both MSE and AARD% are scores that should be minimized; lower values indicate better prediction accuracy.

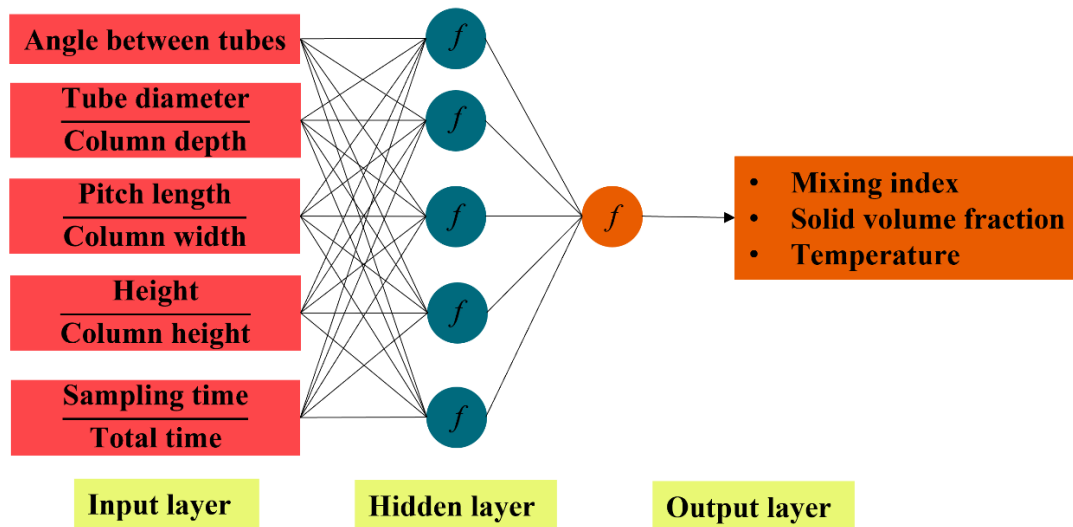


Figure 6.1 Architecture of the developed neural network.

6.4. Results and discussions

6.4.1. RSM model performance

The performance and prediction results of the RSM model are being evaluated. Regression models are developed for each response variable provided below.

$$0.7731 + 0.005A - 0.0034B + 0.0007C - 0.0002AB - 0.0001AC + 0.00002BC + (6 \times 10^{-6})ABC \quad (36)$$

$$0.2567 + 0.0003A - 0.0025B - (3 \times 10^{-5})AB \quad (37)$$

$$0.4943 - 0.0031A - 0.0185B - 0.00827C + 0.00009AC + 0.0005BC \quad (38)$$

$$0.2791 - 0.0052A - 0.0112B - 0.0052C + 0.0004AB + 0.0001AC + 0.0003BC - (8 \times 10^{-6})ABC \quad (39)$$

$$180.47 + 2.58A + 8.45B + 2.95C - 0.227AB - 0.068AC - 0.2121BC + 0.006ABC \quad (40)$$

$$198.34 + 1.64A + 7.16B + 2.52C - 0.1304AB - 0.0441AC - 0.1815BC + 0.0035ABC \quad (41)$$

$$194.76 + 3.62A + 6.63B + 2.78C - 0.2371AB - 0.0962AC - 0.1758BC + 0.0063ABC \quad (42)$$

where A , B , and C are the angle between tubes, tube diameter, and distance between tubes, respectively. The equation (36) is used to predict the average mixing index, while equations (37)-(39) are used to predict the average solid volume fraction at the heights of 0.065, 0.1, and 0.14 m, respectively. Equations (40)-(42) are used to predict the average solid temperature at the heights of 0.065, 0.1, and 0.14 m, respectively. These models are used to generate predictions for the output responses across various points in the input variable space. The resulting predictions are then used to construct surface response plots, which visually depict the relationship between input variables and output responses. Figure 6.2 illustrates an example of a surface response plot, specifically showing the relationship between the angle between tubes and tube diameter with the average solid volume fraction at a height of 0.065 m. This plot helps in understanding how the output variable changes in response to variations in the input variables. It provides valuable insights into the nature of the relationship between the input and output variables.

The accuracy of the RSM model predictions is compared to the results obtained from CFD-DEM simulations, as presented in Table 5.2 in Chapter 5. The discrepancies between the predictions and simulation results are quantified and shown in Table 6.2, indicating an accuracy within a range of $\pm 2\%$ error. Although the RSM model demonstrates high prediction accuracy, it should be noted that these models are limited to predicting the specified responses. The models cannot be used to predict results at arbitrary positions within the fluidized bed, such as the solid temperature at a height of 0.09 m. This limitation arises from the regression models being based only on the input variables (angle between tubes, tube diameter, and distance between tubes) and their corresponding output responses. Therefore, while the RSM model can

provide accurate predictions for specific responses, it may not be suitable for real-time prediction of system parameters throughout the entire fluidized bed.

Table 6.2 Deviation prediction results for each response using RSM models.

Case	Deviation prediction for responses (%)						
	AVG Mixing Index	AVG SVF H=0.065 m	AVG SVF H=0.1 m	AVG SVF H=0.14 m	AVG Temp H=0.065 m	AVG Temp H=0.1 m	AVG Temp H=0.14 m
1	-0.0168	0.67515	1.391	-0.0935	-5.8E-05	-1.9E-05	2.5E-05
2	-0.0192	-0.6647	-0.3795	-0.1184	-6.7E-05	-2.0E-05	2.7E-05
3	-0.0278	-0.3932	-1.3592	-0.1429	-9.1E-05	-6.4E-05	2.5E-05
4	-0.0317	0.39912	0.33196	-0.1606	-0.0001	-7.0E-05	2.7E-05
5	-0.0235	-1.4542	-1.1207	-0.2112	-0.0016	0.0019	-0.0028
6	-0.025	1.47954	0.64023	-0.2707	-0.0019	0.0022	-0.0032
7	-0.0469	-0.3623	1.67736	-0.1293	-0.0028	0.0033	-0.0046
8	-0.0497	0.34514	-0.0448	-0.1847	-0.0032	0.0037	-0.0053

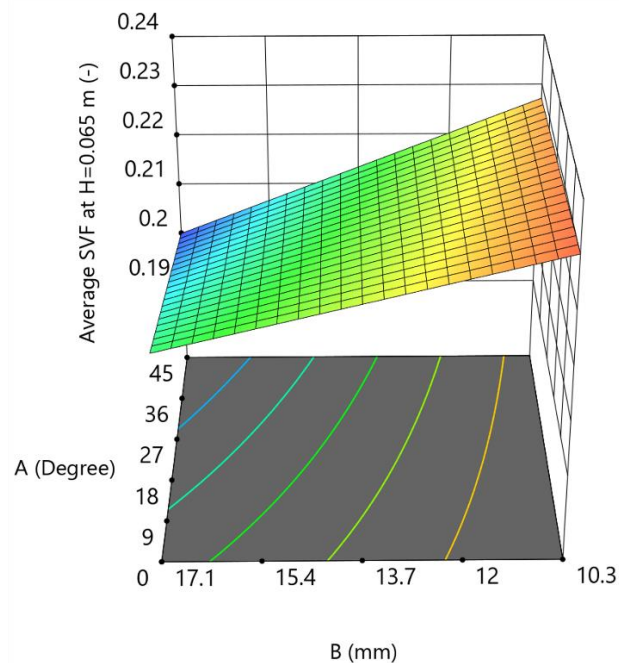


Figure 6.2 Example of the surface response plot for the relationship between the angle between tubes (A) and tube diameter (B) with the average solid volume fraction at a height of 0.065 m.

6.4.2. ANN model performance

This section demonstrates the training, validating, and testing outcomes of the models based on their respective outputs. During the process, the errors on each dataset are quantified by the train, validation, and test loss, which are calculated using a loss function. The loss function serves as a measure to assess the accuracy of the algorithm in modeling the dataset. A smaller output value of the loss function indicates a more precise algorithm in modeling the dataset. In machine learning, there are various types of loss functions, such as mean squared error (MSE), likelihood function, and mean absolute error (MAE). In this study, MSE is employed as the loss function. Consequently, the train loss, validation loss, and test loss can be monitored throughout each epoch. The number of epochs refers to the number of times the networks have undergone training [138].

Figure 6.3 shows the evaluation of training, validation, and test MSEs with respect to the number of epochs. It is evident that all models exhibit a gradual decrease in loss during each process, indicating an improvement in accuracy across the training, validation, and test periods. In the case of the mixing index prediction model, the testing MSE is higher compared to the other models. On the other hand, for the solid volume fraction and solid temperature predictions, the validation MSE is relatively higher. However, the optimal performance of each process is achieved when the models reach the epoch with the lowest MSE, signifying a stable network and the avoidance of overfitting to the CFD-DEM data [139]. Nonetheless, the testing process will be used to evaluate the performance of each model.

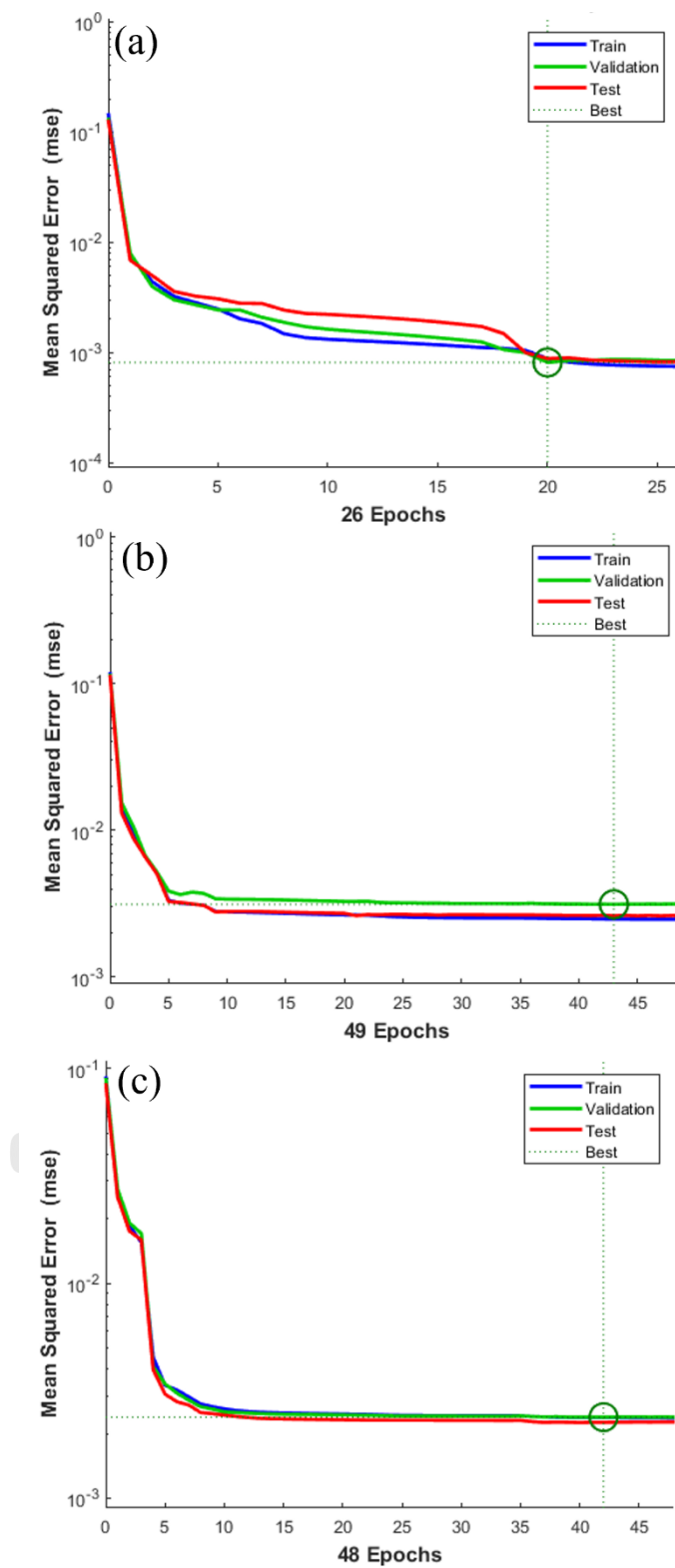


Figure 6.3 Evolution of training, validation, and test MSEs where output is
 (a) mixing index, (b) solid volume fraction, and (c) solid temperature.

Identifying the key input variables that have a significant impact on the output parameters is crucial for the development of any modeling study. The correlation coefficient, ranging from -1 to +1, indicates the degree of linear association between each pair of input and output variables. Positive and negative values indicate positive and negative correlations, respectively. The analysis provides a quantitative measure of the strength of the linear relationship. Additionally, a correlation coefficient of zero indicates no linear relationship between the variables under consideration. Figure 6.4 illustrates the correlation coefficients between the input and output variables in each model. In Figure 6.4a, it is shown that the sampling time per total time (t_s/t) has a positive correlation with the mixing index. This indicates that the mixing behavior between the mixed biomass and silica sand tends to improve with increasing time. On the other hand, the height per column height (h/z) has a negative effect on the mixing index. This can be attributed to the fact that particles predominantly distribute at the lower part of the fluidized bed, resulting in poorer mixing behavior when investigating the middle of the bed. However, the other variables related to the design of the immersed tubes in the fluidized bed combustor exhibit minimal effects on the mixing index. This finding aligns with the results of the investigation in Chapter 5, where the mixing indexes were found to be insignificantly different in the study cases. In Figure 6.4b, it demonstrates a strong negative correlation between the h/z and the solid volume fraction. This observation is consistent with the typical axial solid volume fraction profile observed in the operation of a bubbling fluidized bed, as investigated in the previous chapter. Additionally, the other variables related to the design of the immersed tubes show minimal effects on the axial solid volume fraction. However, these design variables do influence the radial solid volume fraction at

different heights, as examined in Chapter 5. In Figure 6.4c, it can be seen that the t_s/t exhibits a strong positive correlation with the solid temperature. This can be attributed to the system not having reached a steady state, resulting in an increase in solid temperature over time. Furthermore, the h/z has a positive effect on the solid temperature, as the particles improved heat transfer from the immersed tubes in the system, leading to an overall increase in temperature. Similar to the previous case, the other design variables have an impact on the radial solid temperature at different heights, as investigated in Chapter 5.

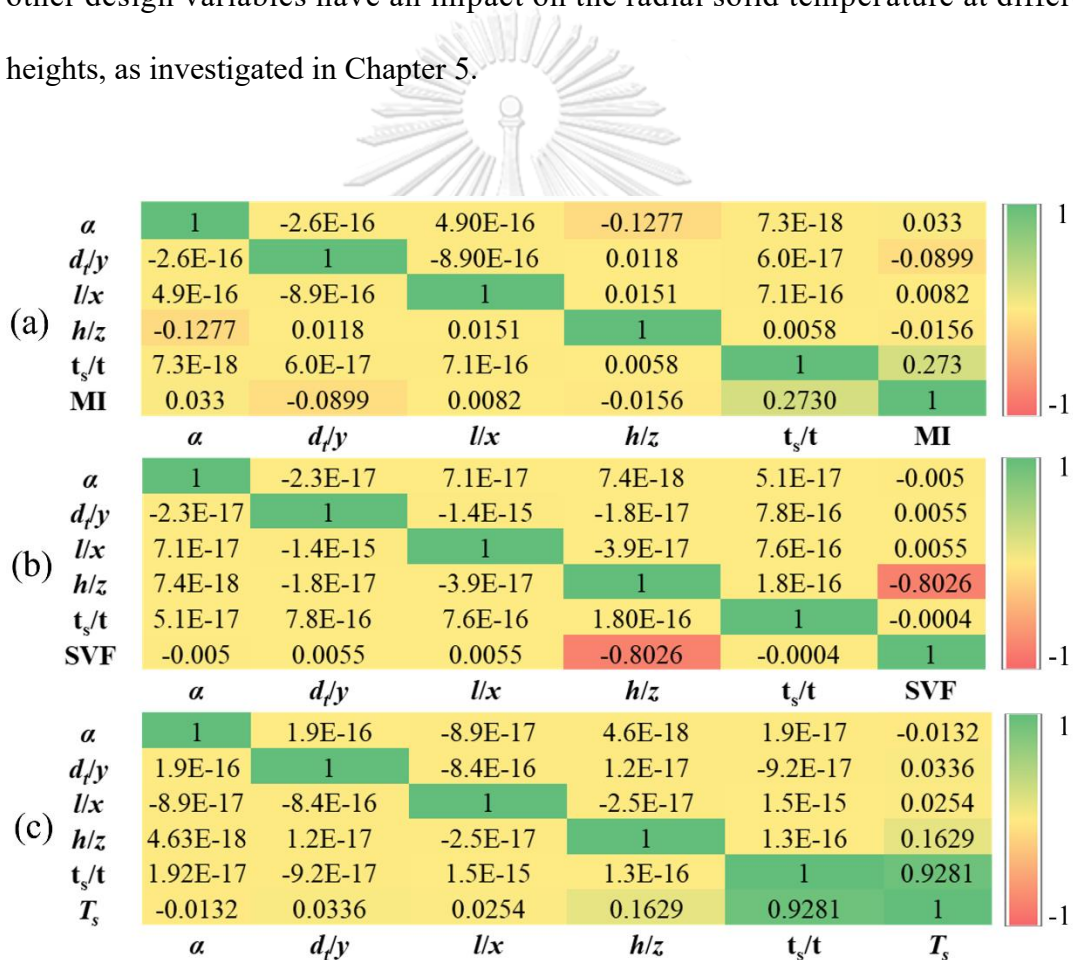


Figure 6.4 Correlation coefficients of the input variables and output is

(a) mixing index, (b) solid volume fraction, and (c) solid temperature.

In order to construct an appropriate ANN model, the number of hidden layers and the optimal number of neurons in each hidden layer were determined. Based on Cybenko's study, it was found that a single hidden layer can provide a relatively accurate estimation of the target variable in a multi-variable system, achieving an accuracy above 95% [140]. Consequently, an ANN model with one hidden layer was utilized to predict the mixing index, solid volume fraction, and solid temperature. Furthermore, the optimal number of neurons in the hidden layer was determined to ensure predictive performance within an acceptable error range. The performance of the ANN model was evaluated using statistical indices, including R^2 , MSE, and AARD%, to assess its predictive capabilities.

The ANN topologies were trained multiple times using different datasets to mitigate the impact of initial weight and bias values on the results. Only the best-performing topology was selected and reported in Table 6.3, which provides a summary of the optimal network configurations for each prediction. Moreover, appropriate activation functions were identified for the hidden and output layers, along with the optimal number of neurons for each output. The R^2 scores in Table 6.3 indicate a good level of prediction performance for the ANN models, with values exceeding 0.8. However, it should be noted that the MSE value for solid temperature prediction is noticeably higher compared to the other models, mainly due to the differing value range of this parameter in comparison to the mixing index and solid volume fraction. Similarly, the AARD% value for the solid volume fraction prediction model is higher than the others, reflecting the prediction error at the decimal level. The optimal topologies for each prediction are also indicated in Table 6.3, with five input variables in the input layer, a hidden layer with eleven, ten, and eleven neurons

for mixing index, solid volume fraction, and solid temperature, respectively, and one output variable in the output layer. Consequently, the structure of the models can be simply represented by the notations 5–11–1, 5-9-1, and 5-11-1 for mixing index, solid volume fraction, and solid temperature predictions, respectively.

Table 6.3 Obtained results of neural networks prediction.

Output	Number of neurons	Activation functions	R ²	%AARD	MSE
Mixing index	11	Tansig-Tansig	0.8388	0.0732	0.001
Solid volume fraction	9	Radbas-Tansig	0.812	12.21	0.002
Solid temperature	11	Radbas-Tansig	0.9208	0.0634	46.01

6.4.3. Prediction of Mixing Index

In this section, the ANN model is employed to predict the mixing degree of mixed biomass and silica sand under different case settings. The Lacey mixing index is used as the measure of mixing degree, which is commonly used in statistical analysis [103]. Each cell in the system has a uniform height and equal to $H_{max,t}$, which represents the maximum bed height at a given time instant t [130].

Figure 6.5 presents a comparison between the mixing index obtained from CFD-DEM simulation and the predicted values from the ANN model using the testing data. It is important to note that the testing data has not been used for training the model, and it serves as an independent evaluation of the model's prediction accuracy. Both the CFD-DEM simulation and the ANN model demonstrate a good prediction of the mixing index.

Figure 6.6 shows a comparison between the CFD-DEM simulation data and the predicted results of the mixing index using the optimal ANN model for the testing data. The 45-degree line represents the exact estimates where the prediction values exactly coincide with the simulation data. It can be observed that a considerable number of data points are closely clustered around this line, with slight deviations of around $\pm 15\%$. This confirms that the optimal ANN model is capable of accurately predicting the mixing index over time with acceptable accuracy.

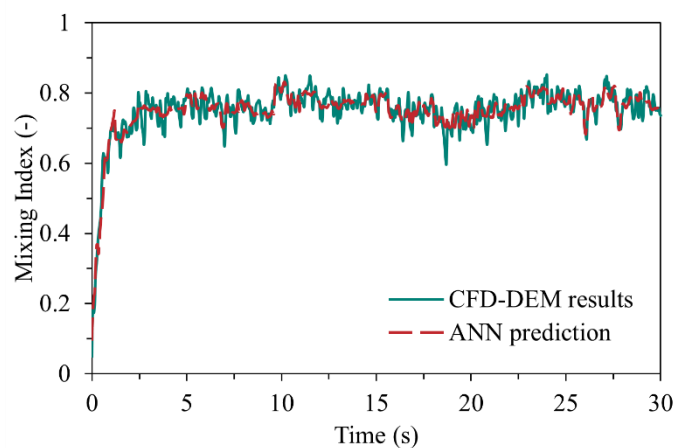


Figure 6.5 Comparisons of the mixing index between the obtained CFD-DEM results and ANN model prediction.

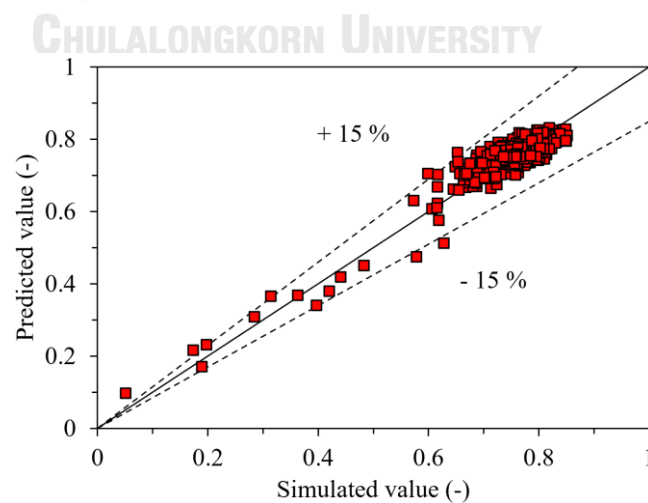


Figure 6.6 Comparison of the CFD-DEM results with those calculated prediction by neural network for the mixing index.

6.4.4. Prediction of solid volume fraction

Figure 6.7 illustrates the comparison between the solid volume fraction obtained from CFD-DEM simulation and the predicted values generated by the ANN model using the testing data. The figure is divided into two sections: Figure 6.7a represents the prediction for the fluidized bed with immersed tubes in an in-line configuration, while Figure 6.7b represents the staggered configuration. The results demonstrate that both predictions provide accurate estimations of the solid volume fraction, with only minor deviations observed at the bottom of the bed, where the particle distribution is most concentrated.

Figure 6.8 shows the comparison between the CFD-DEM simulation data and the predicted results of the axial solid volume fraction using the optimal ANN model with the testing data. The majority of data points are closely clustered around a line located at the upper part of the bed, indicating a high level of agreement between the predicted and simulated values. However, slight deviations can be observed at the bottom of the bed. The optimal ANN model demonstrates its capability to accurately predict the axial solid volume fraction within a range of approximately $\pm 25\%$.

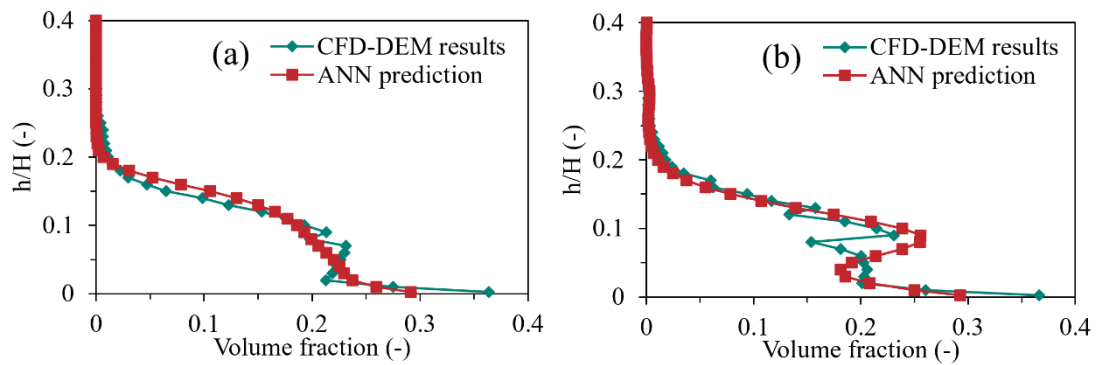


Figure 6.7 Comparisons of the axial solid volume fraction between the obtained CFD-DEM results and ANN model prediction for (a) in-line and (b) staggered immersed tubes configurations.

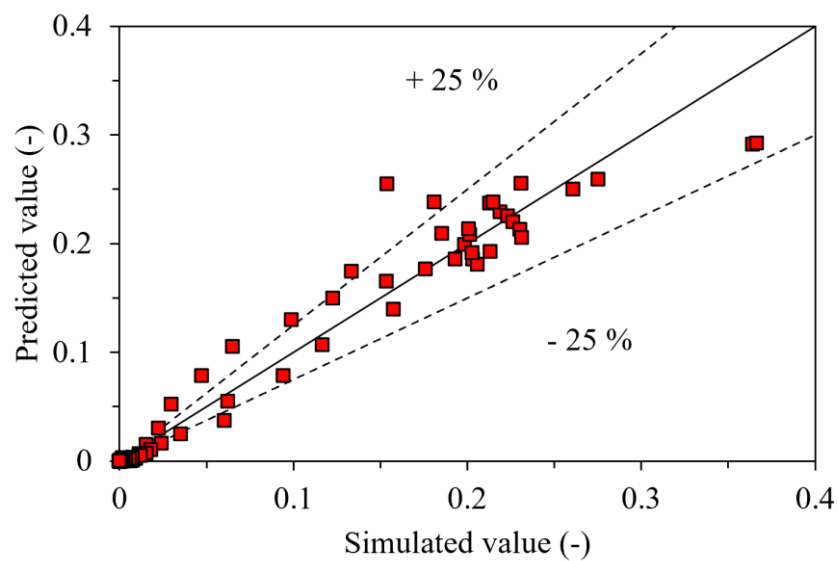


Figure 6.8 Comparison of the CFD-DEM results with those calculated prediction by neural network for the axial solid volume fraction.

6.4.5. Prediction of solid temperature

Figure 6.9 presents a comparison between the solid temperature obtained from CFD-DEM simulation and the predicted values generated by the ANN model using the testing data. The figure is divided into two sections: Figure 6.9a corresponds to the prediction for the fluidized bed with immersed tubes in an in-line configuration, while Figure 6.9b represents the staggered configuration. The results indicate that the predicted values provide accurate estimation of the solid temperature for the staggered configuration. However, in the case of the in-line configuration, there is a slight deviation between the predicted and simulated results. Nevertheless, this deviation is relatively small, with a difference of less than 2 °C when compared to the actual value.

Figure 6.10 shows the comparison between the axial solid temperature obtained from CFD-DEM simulation and the predicted results using the optimal ANN model with the testing data. The majority of data points cluster closely around a line situated at the upper region of the bed, indicating a high level of agreement between the predicted and simulated values. However, slight deviations can be observed at the bottom of the bed. Nonetheless, these deviations are relatively small, with an error range of ± 2.5 . Therefore, the optimal ANN model demonstrates the capability to accurately predict the axial solid temperature within an acceptable range of error.

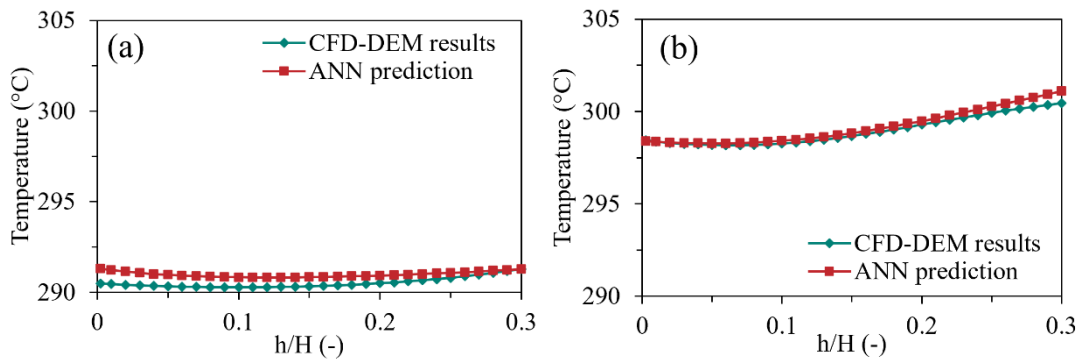


Figure 6.9 Comparisons of the axial solid temperature between the obtained CFD-DEM results and ANN model prediction for (a) in-line and (b) staggered immersed tubes configurations.

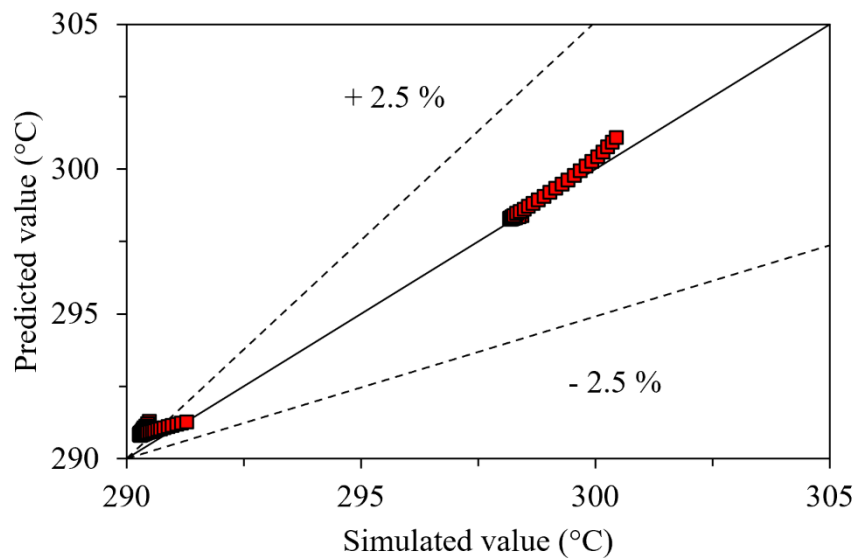


Figure 6.10 Comparison of the CFD-DEM results with those calculated prediction by neural network for the axial solid temperature.

6.5. Conclusion

This chapter focuses on the development of data-driven models using RSM and ANN techniques to predict the mixing index, axial solid volume fraction, and axial solid temperature in a fluidized bed combustor with immersed tubes. The models are constructed and trained using a dataset that includes input variables related to the design parameters of the fluidized bed with immersed tubes. The RSM models, based on regression analysis, successfully represented the relationship between the input variables and the output, providing accurate predictions within an acceptable range compared to CFD-DEM results. However, the limitation of RSM models lies in their inability to predict system parameters in real-time due to their reliance solely on input variables and corresponding output responses. On the other hand, the comparison between the CFD-DEM simulation data and the predicted results demonstrates the reliability of the ANN models, with R^2 values exceeding 0.812. This confirms the effectiveness of the models in accurately predicting the system's behavior. Some deviations are observed in the lower region of the bed, but the errors remain within an acceptable range as evaluated by MSE and AARD%. Overall, the developed ANN models show their capability to provide accurate predictions of the mixing behavior and key parameters including solid volume fraction and solid temperature in the fluidized bed system with immersed tubes. These models have potential for practical engineering applications, as the ANNs can predict system parameters in real-time without requiring the CFD-DEM simulation. Furthermore, with the same methodology, the model can also be applied to predict system parameters by incorporating input variables related to operational parameters of the fluidized bed with immersed tubes, such as biomass loading and biomass blending ratio.

CHAPTER 7

CONCLUSION

This research study focuses on the numerical investigation of hydrodynamics and heat transfer in the biomass bubbling fluidized bed combustor with immersed tubes. The CFD-DEM technique was used to simulate and analyze the mixing behavior and heat transfer within the system, considering the mixture of biomass and silica sand. The simulation data obtained from this study will be employed to develop the data-driven model using the ANN technique, aiming to predict the system parameters. This chapter provides a comprehensive summary of the study's innovative findings across all aspects and offers recommendations for future research in this field.

In Chapter 3, the CFD-DEM model was developed for cylindrical biomass and spherical silica sand particles. The drag force model was improved by parameterizing the Syamlal & O'Brien drag force model and incorporating it into the developed model. A 2^k factorial experimental design was employed to examine the influence of biomass and silica sand sizes, as well as biomass loading, on the average mixing index. The results highlighted that the diameter of the biomass particles was the main factor affecting the average mixing index. The biomass loading and the interaction between parameters had only a slight impact on the average mixing index. Furthermore, using smaller silica sand and biomass particle diameters resulted in higher average mixing indices, even with increased biomass loading. Thus, it is recommended to consider smaller biomass sizes and smaller silica sand particles for fluidization in binary mixture systems.

In Chapter 4, the study employed the developed CFD-DEM model, along with the heat transfer model, to investigate the effects of various biomass types, loadings, and blending ratios on mixing behavior and heat transfer in a bubbling fluidized bed. The focus was on mixed biomass consisting of cylindrical wood chip and bagasse, considering their size distribution. Coarse bagasse particles exhibited the most efficient mixing behavior in single biomass mixtures. A blending ratio of 1:3 of wood chip to coarse bagasse with a 5% biomass loading using a ratio of the average equivalent diameter of the biomasses to the equivalent diameter of silica sand of 4.44, was identified as suitable conditions in a general case. The primary factor influencing mixing behavior was the difference in equivalent particle diameter, while different biomass loadings had less impact. In addition, smaller silica sand particle sizes led to variations in particle convective heat transfer rates, affecting the temperature distribution within individual particles. Improving mixing behavior through the use of smaller silica sand sizes could consequently enhance heat transfer behavior in mixed biomass mixtures. These findings highlight the importance of biomass size distribution, blending ratios, and silica sand particle size in achieving efficient mixing behavior and improved heat transfer in biomass-silica sand mixtures.

In Chapter 5, the study aimed to investigate the impact of design parameters related to immersed tubes in a mixed biomass fluidized bed combustor. Using a 2^k factorial design analysis, it was determined that the optimal condition for a general case was identified as a staggered configuration with a dimensionless tube diameter per column width of 51.5 and a dimensionless distance between tubes per height of the tube zone of 120, based on the average mixing index. The introduction of immersed tubes in the system was found to improve both mixing behavior and heat

transfer compared to the system without immersed tubes. The presence of immersed tubes can also affect bubble dynamics, leading to changes in bubble breakage or coalescence and subsequently influencing the heat transfer coefficient in the system. The choice of staggered tube configuration and larger tube diameters had a significant impact on the flow pattern, while the particle temperature showed minimal variation due to the efficient mixing behavior indicated by the mixing index. The distance between tubes did not significantly affect hydrodynamics, mixing behavior, or heat transfer within the investigated range. Using a smaller tube diameter tends to result in a higher heat transfer coefficient around the tube, but the solid volume fraction around the tube is influenced by heat conduction dominance. However, the analysis of heat transfer coefficient specifically focuses on convective heat transfer around the tubes, which tends to be lower when using smaller tubes compared to the overall heat transfer rate in the system. Therefore, considering the system as a whole, using a larger tube diameter may result in a higher heat transfer rate and increased particle temperature. Overall, these findings enhance the understanding of hydrodynamics in such systems and provide valuable insights for optimizing the design and operation of applications involving mixed biomass and silica sand.

In Chapter 6, the study focused on the development of data-driven models using RSM and ANN techniques to predict the mixing index, axial solid volume fraction, and axial solid temperature in a fluidized bed combustor with immersed tubes. The models were trained using a dataset containing design parameter inputs specific to the system. The RSM models provided accurate predictions with deviations of $\pm 2\%$ compared to the CFD-DEM results. However, these models lacked real-time prediction capability due to their reliance on input variables and

corresponding output responses. In addition, the ANN models showed reliable predictions with R^2 values exceeding 0.812, accurately capturing system behavior. While some deviations were observed in the lower region of the bed, the errors remained within an acceptable range as evaluated by MSE and AARD%. Overall, the developed ANN models demonstrated their ability to provide accurate predictions of mixing behavior, solid volume fraction, and solid temperature in fluidized bed systems with immersed tubes. These models have potential for practical engineering applications, offering real-time prediction without the need for CFD-DEM simulation.

Research outcomes

- The CFD-DEM model, implemented with the novel parameterized drag force model, was proposed for use with cylindrical biomass and spherical silica sand in a binary mixture within a bubbling fluidized bed.
- The study proposed the suitable conditions for using mixed biomass, considering biomass type, loading, and blending ratio. The primary determining factor, the difference in equivalent particle diameters, was identified as a criterion for selecting biomass for bubbling fluidized bed.
- The study proposed an understanding of the influence of design parameters related to the addition of immersed tubes in a fluidized bed on mixing behavior and heat transfer. These findings serve as guidelines for designing bubbling fluidized bed applications with immersed tubes.
- Data-driven models using the ANN approach were proposed for predicting system parameters, offering the potential for real-time operation.

Recommendations for future studies

- The fluidized bed with immersed should be studied in the large scale in order to compare the actual operation results.
- Considering the energy required for biomass size reduction, biomass availability, handling and storage requirements, and the specific needs of the combustion system when choosing biomass for use in the system contributes to optimizing the overall energy consumption and performance of the biomass combustion process.
- The inclusion of immersed tubes in the system requires careful consideration of flow dynamics and temperature control, with regular cleaning and maintenance procedures necessary to prevent fouling and blockage, while also considering the additional cost and complexity associated with specialized equipment and the need for proper engineering practices and maintenance strategies to ensure reliable and cost-effective operation.
- The model should incorporate combustion and chemical reactions to accurately represent real-world phenomena, considering efficient fuel-oxidizer mixing for maximizing combustion efficiency and controlling the bed temperature to ensure stable combustion and avoid issues like thermal runaway or incomplete combustion, enabling accurate prediction and control of combustion behavior for efficient and environmentally friendly system operation.
- The other operation and design parameter should be studied to expand the dataset for developed the prediction model to further enhance the accuracy of the models.

APPENDIX

Table A.1 The weight and bias coefficients of the optimum neural network model for mixing index prediction.

Neurons (n)	$IW(I,n)_1$	$IW(I,n)_2$	$IW(I,n)_3$	$IW(I,n)_4$	$IW(I,n)_5$	$b(I,n)$	$LW(I,n)$
1	5.5602	-0.4464	-5.1712	-0.3677	-4.3204	-5.1228	-5.3499
2	-0.0503	1.2753	-0.3176	1.5433	-1.4455	2.3510	-0.5508
3	2.2484	0.2996	-0.4537	1.8510	0.3370	-1.5152	0.3461
4	1.3773	1.1020	2.1286	-0.3546	-0.3976	-1.5210	-0.4880
5	0.5648	-0.9000	1.7770	-0.9367	-0.1523	0.6977	0.8953
6	-0.9395	-1.9294	0.9719	1.2464	-0.6535	0.3232	0.1965
7	-0.6955	-1.1399	-1.4751	-0.1621	-0.9055	-0.0917	0.7023
8	1.1759	-1.5679	0.2522	-0.0685	-2.0069	-2.0217	0.8052
9	1.4610	0.8364	2.0699	0.1482	0.9929	1.3055	-0.9947
10	0.5890	0.8311	0.1558	1.8189	-0.7174	1.6929	0.5524
11	1.6199	-0.5936	0.1588	1.8231	-0.2536	2.4515	0.4890

$$b(2,n) = 0.608$$

Table A.2 The weight and bias coefficients of the optimum neural network model for solid volume fraction prediction.

Neurons (n)	$IW(I,n)_1$	$IW(I,n)_2$	$IW(I,n)_3$	$IW(I,n)_4$	$IW(I,n)_5$	$b(I,n)$	$LW(I,n)$
1	0.2604	2.1424	3.6019	1.8004	0.2150	-1.9948	1.1678
2	0.6819	-0.9147	-0.6423	-2.5967	1.5005	1.1407	-0.2332
3	0.0244	0.0024	0.0151	-8.9837	-0.0028	-10.5256	5.5164
4	-1.1873	-2.9634	4.1118	5.2320	-4.1879	-0.5458	0.2173
5	-0.3671	1.5358	1.5779	6.3241	-2.3877	3.1859	-0.1762
6	-0.4605	-2.7446	0.1492	-2.0553	-0.3787	-2.1930	-1.0364
7	-1.8952	-0.5030	-0.5025	-1.2457	0.6758	-2.1002	0.1817
8	0.0344	0.0853	0.0195	-1.7447	-0.0621	0.9697	-5.1779
9	-0.4155	1.9317	0.9753	-2.9666	-0.5096	2.4246	0.9014

$$b(2,n) = -0.2369$$

Table A.3 The weight and bias coefficients of the optimum neural network model for solid temperature prediction.

Neurons (n)	$IW(1,n)_1$	$IW(1,n)_2$	$IW(1,n)_3$	$IW(1,n)_4$	$IW(1,n)_5$	$b(1,n)$	$LW(1,n)$
1	-2.0948	2.1179	-0.2414	1.7013	0.0340	2.8833	0.1737
2	1.4588	1.3155	1.3414	0.9166	1.4900	-1.6793	0.1633
3	0.0797	-0.4178	0.2728	-0.2659	-0.4216	-1.6428	-2.2245
4	-1.4775	0.1684	0.3269	0.9391	-0.7268	1.3171	-0.1624
5	-1.5203	0.3023	-1.6692	-0.4176	-0.1287	-1.8410	1.4879
6	-0.0466	0.0936	0.0413	-0.2786	-1.2271	-0.7929	0.4205
7	0.9800	0.0550	3.7924	0.4143	-0.9172	0.7893	-1.3678
8	-0.0920	-1.5333	-0.3067	0.5165	0.2504	0.5161	1.6416
9	0.6592	-0.1064	-2.5609	0.8521	-1.6466	0.4957	-0.2148
10	0.0976	-0.2096	0.1915	-0.0867	0.1839	-0.6777	3.5875
11	-1.5996	-0.2276	-1.7640	0.5462	-0.1594	-1.8543	1.7024

$b(2,n) = -3.1033$

REFERENCES

- [1] R. Birner, Bioeconomy concepts, Bioeconomy: Shaping the transition to a sustainable, biobased economy (2018) 17-38.
- [2] M.T. Aung, Bioeconomy in Thailand: at a glance, Stockholm Environment Institute Discussion Brief 2021.
- [3] A. Khan, W. de Jong, P. Jansens, H. Spliethoff, Biomass combustion in fluidized bed boilers: Potential problems and remedies, Fuel processing technology 90(1) (2009) 21-50.
- [4] J. Chen, X. Shi, S. Wang, J. Li, T. Hu, F. Lin, M. Liu, Investigation into fluctuating anisotropy for biomass gasification in bubbling fluidized bed gasifier, Applied Thermal Engineering 138 (2018) 774-782.
- [5] F. Fotovat, J. Chaouki, J. Bergthorson, The effect of biomass particles on the gas distribution and dilute phase characteristics of sand–biomass mixtures fluidized in the bubbling regime, Chemical Engineering Science 102 (2013) 129-138.
- [6] S. Suakrasang, C. Treepob, Design of biomass mixture for electricity generation. Case study: Biomass power plant Prachuap Khiri Khan province Industry Technology Lampang Rajabhat University Journal 12(2) (2019) 73-83.
- [7] B. Leckner, Fluidized bed combustion: mixing and pollutant limitation, Progress in Energy and Combustion Science 24(1) (1998) 31-61.
- [8] Y. Zhao, M. Jiang, Y. Liu, J. Zheng, Particle-scale simulation of the flow and heat transfer behaviors in fluidized bed with immersed tube, AIChE Journal 55(12) (2009) 3109-3124.
- [9] H. Vogtenhuber, D. Pernsteiner, R. Hofmann, Experimental and numerical

investigations on heat transfer of bare tubes in a bubbling fluidized bed with respect to better heat integration in temperature swing adsorption systems, *Energies* 12(14) (2019) 2646.

[10] A.J. Ragauskas, *Materials for biofuels*, World Scientific 2014.

[11] A. Williams, J. Jones, L. Ma, M. Pourkashanian, Pollutants from the combustion of solid biomass fuels, *Progress in Energy and Combustion Science* 38(2) (2012) 113-137.

[12] H. Haykırı-Açma, Combustion characteristics of different biomass materials, *Energy Conversion and Management* 44(1) (2003) 155-162.

[13] T. Bridgeman, L. Darvell, J. Jones, P. Williams, R. Fahmi, A. Bridgwater, T. Barraclough, I. Shield, N. Yates, S. Thain, Influence of particle size on the analytical and chemical properties of two energy crops, *Fuel* 86(1-2) (2007) 60-72.

[14] A. Demirbaş, Biomass resource facilities and biomass conversion processing for fuels and chemicals, *Energy conversion and Management* 42(11) (2001) 1357-1378.

[15] M. Erol, H. Haykiri-Acma, S. Küçükbayrak, Calorific value estimation of biomass from their proximate analyses data, *Renewable energy* 35(1) (2010) 170-173.

[16] R. Samuelsson, J. Burvall, R. Jirjis, Comparison of different methods for the determination of moisture content in biomass, *Biomass and Bioenergy* 30(11) (2006) 929-934.

[17] R. Saidur, E. Abdelaziz, A. Demirbas, M. Hossain, S. Mekhilef, A review on biomass as a fuel for boilers, *Renewable and sustainable energy reviews* 15(5) (2011) 2262-2289.

[18] A. Evans, V. Strezov, T.J. Evans, Sustainability considerations for electricity generation from biomass, *Renewable and sustainable energy reviews* 14(5) (2010) 1419-

1427.

- [19] A.R. Proto, A. Palma, E. Paris, S.F. Papandrea, B. Vincenti, M. Carnevale, E. Guerriero, R. Bonofiglio, F. Gallucci, Assessment of wood chip combustion and emission behavior of different agricultural biomasses, *Fuel* 289 (2021) 119758.
- [20] Y. Loh, D. Sujan, M.E. Rahman, C.A. Das, Sugarcane bagasse—The future composite material: A literature review, *Resources, Conservation and Recycling* 75 (2013) 14-22.
- [21] L. Morais, A. Maia, M. Guandique, A. Rosa, Pyrolysis and combustion of sugarcane bagasse, *Journal of Thermal Analysis and Calorimetry* 129 (2017) 1813-1822.
- [22] A.P. Faaij, Bio-energy in Europe: changing technology choices, *Energy policy* 34(3) (2006) 322-342.
- [23] A. Demirbas, Biorefineries: Current activities and future developments, *Energy conversion and management* 50(11) (2009) 2782-2801.
- [24] R. Overend, Biomass gasification: a growing business, *Renewable Energy World* 1 (1998).
- [25] T. Takeshita, K. Yamaji, Important roles of Fischer–Tropsch synfuels in the global energy future, *Energy Policy* 36(8) (2008) 2773-2784.
- [26] M. Harvey, S. Pilgrim, The new competition for land: Food, energy, and climate change, *Food policy* 36 (2011) S40-S51.
- [27] R. Cocco, S.R. Karri, T. Knowlton, Introduction to fluidization, *Chem. Eng. Prog* 110(11) (2014) 21-29.
- [28] H. Bi, J. Grace, Flow regime diagrams for gas-solid fluidization and upward transport, *International Journal of Multiphase Flow* 21(6) (1995) 1229-1236.

- [29] S. Ergun, A.A. Orning, Fluid flow through randomly packed columns and fluidized beds, *Industrial & Engineering Chemistry* 41(6) (1949) 1179-1184.
- [30] B. Chalermsoinsuwan, S. Boonprasop, P. Nimmanterdwong, P. Piumsomboon, Revised fluidization regime characterization in high solid particle concentration circulating fluidized bed reactor, *International journal of multiphase flow* 66 (2014) 26-37.
- [31] K. Smolders, J. Baeyens, Gas fluidized beds operating at high velocities: a critical review of occurring regimes, *Powder Technology* 119(2-3) (2001) 269-291.
- [32] B. Du, L.S. Fan, F. Wei, W. Warsito, Gas and solids mixing in a turbulent fluidized bed, *AIChE Journal* 48(9) (2002) 1896-1909.
- [33] D. Bai, E. Shibuya, Y. Masuda, N. Nakagawa, K. Kato, Flow structure in a fast fluidized bed, *Chemical Engineering Science* 51(6) (1996) 957-966.
- [34] D. Bai, E. Shibuya, N. Nakagawa, K. Kato, Characterization of gas fluidization regimes using pressure fluctuations, *Powder Technology* 87(2) (1996) 105-111.
- [35] W. Lin, A.D. Jensen, J.E. Johnsson, K. Dam-Johansen, Combustion of biomass in fluidized beds: Problems and some solutions based on Danish experiences, *International Conference on Fluidized Bed Combustion*, 2003, pp. 945-953.
- [36] A. Blaszczyk, M. Pogorzelec, T. Shimizu, Heat transfer characteristics in a large-scale bubbling fluidized bed with immersed horizontal tube bundles, *Energy* 162 (2018) 10-19.
- [37] L. Wang, H.-W. Li, C.-H. Du, W.-P. Hong, Gas flow influences on bubbling and flow characteristics of fluidized bed with immersed tube under electrostatic effects, *Advanced Powder Technology* 33(5) (2022) 103575.

- [38] B. Lan, P. Zhao, J. Xu, B. Zhao, M. Zhai, J. Wang, The critical role of scale resolution in CFD simulation of gas-solid flows: A heat transfer study using CFD-DEM-IBM method, *Chemical Engineering Science* 266 (2023) 118268.
- [39] Z. Zhou, S. Kuang, K. Chu, A. Yu, Discrete particle simulation of particle–fluid flow: model formulations and their applicability, *Journal of Fluid Mechanics* 661 (2010) 482-510.
- [40] B.E. Launder, D.B. Spalding, *The numerical computation of turbulent flows, Numerical prediction of flow, heat transfer, turbulence and combustion*, Elsevier, 1983, pp. 96-116.
- [41] E.A. Molaei, A. Yu, Z. Zhou, Particle scale modelling of mixing of ellipsoids and spheres in gas-fluidized beds by a modified drag correlation, *Powder Technology* 343 (2019) 619-628.
- [42] B. Xu, A. Yu, Numerical simulation of the gas-solid flow in a fluidized bed by combining discrete particle method with computational fluid dynamics, *Chemical Engineering Science* 52(16) (1997) 2785-2809.
- [43] P.A. Cundall, O.D. Strack, A discrete numerical model for granular assemblies, *geotechnique* 29(1) (1979) 47-65.
- [44] G. Dewicki, Bulk material handling and processing- numerical techniques and simulation of granular material, *Bulk solids handling* 23(2) (2003) 110-113.
- [45] H. Zhu, Z.Y. Zhou, R. Yang, A. Yu, Discrete particle simulation of particulate systems: theoretical developments, *Chemical Engineering Science* 62(13) (2007) 3378-3396.
- [46] J.M. Boac, R.K. Ambrose, M.E. Casada, R.G. Maghirang, D.E. Maier, Applications

of discrete element method in modeling of grain postharvest operations, *Food Engineering Reviews* 6 (2014) 128-149.

[47] R. Berger, C. Kloss, A. Kohlmeyer, S. Pirker, Hybrid parallelization of the LIGGGHTS open-source DEM code, *Powder technology* 278 (2015) 234-247.

[48] J. Theuerkauf, S. Dhodapkar, K. Jacob, Modeling granular flow: using discrete element method--from theory to practice: this emerging simulation technique is changing the face of solids processing, *Chemical Engineering* 114(4) (2007) 39-47.

[49] J.R. Williams, The theoretical basis of the discrete element method, *Proc. of the NUMETA'85 Conference*, 1985, pp. 897-906.

[50] M.A. El-Emam, L. Zhou, W. Shi, C. Han, L. Bai, R. Agarwal, Theories and applications of CFD-DEM coupling approach for granular flow: A review, *Archives of Computational Methods in Engineering* 28(7) (2021) 4979-5020.

[51] S. Akhshik, M. Behzad, M. Rajabi, CFD-DEM approach to investigate the effect of drill pipe rotation on cuttings transport behavior, *Journal of Petroleum Science and Engineering* 127 (2015) 229-244.

[52] ESSS-Rocky, DEM Technical Manual, Release 4.5.1, ESSS Rocky DEM, 2021.

[53] O.R. Walton, R.L. Braun, Viscosity, granular-temperature, and stress calculations for shearing assemblies of inelastic, frictional disks, *Journal of rheology* 30(5) (1986) 949-980.

[54] V. Vivacqua, A. López, R. Hammond, M. Ghadiri, DEM analysis of the effect of particle shape, cohesion and strain rate on powder rheometry, *Powder Technology* 342 (2019) 653-663.

[55] G.K. Batchelor, R. O'brien, Thermal or electrical conduction through a granular

material, Proceedings of the Royal Society of London. A. Mathematical and Physical Sciences 355(1682) (1977) 313-333.

[56] ESSS-Rocky, DEM-CFD Coupling Technical Manual, Release 4.5.1, ESSS Rocky DEM, 2021.

[57] D. Gunn, Transfer of heat or mass to particles in fixed and fluidised beds, International Journal of Heat and Mass Transfer 21(4) (1978) 467-476.

[58] M. Syamlal, T. O'Brien, The derivation of a drag coefficient formula from velocity-voidage correlations, Technical Note, US Department of energy, Office of Fossil Energy, NETL, Morgantown, WV (1987).

[59] ANSYS, ANSYS Fluent Theory Guide, Release 2020 R2, ANSYS Inc., 2020.

[60] O.I. Abiodun, A. Jantan, A.E. Omolara, K.V. Dada, A.M. Umar, O.U. Linus, H. Arshad, A.A. Kazaure, U. Gana, M.U. Kiru, Comprehensive review of artificial neural network applications to pattern recognition, IEEE Access 7 (2019) 158820-158846.

[61] K. Korkerd, C. Soanuch, D. Gidaspow, P. Piumsomboon, B. Chalermssinsuwan, Artificial neural network model for predicting minimum fluidization velocity and maximum pressure drop of gas fluidized bed with different particle size distributions, South African Journal of Chemical Engineering 37 (2021) 61-73.

[62] P. Dhruv, S. Naskar, Image classification using convolutional neural network (CNN) and recurrent neural network (RNN): a review, Machine Learning and Information Processing: Proceedings of ICMLIP 2019 (2020) 367-381.

[63] Y. Yu, X. Si, C. Hu, J. Zhang, A review of recurrent neural networks: LSTM cells and network architectures, Neural computation 31(7) (2019) 1235-1270.

[64] A. Aggarwal, M. Mittal, G. Battineni, Generative adversarial network: An overview

of theory and applications, *International Journal of Information Management Data Insights* 1(1) (2021) 100004.

[65] A. Apicella, F. Donnarumma, F. Isgrò, R. Prevete, A survey on modern trainable activation functions, *Neural Networks* 138 (2021) 14-32.

[66] H. Ma, L. Xu, Y. Zhao, CFD-DEM simulation of fluidization of rod-like particles in a fluidized bed, *Powder technology* 314 (2017) 355-366.

[67] H. Ma, Y. Zhao, CFD-DEM investigation of the fluidization of binary mixtures containing rod-like particles and spherical particles in a fluidized bed, *Powder Technology* 336 (2018) 533-545.

[68] I. Mema, J.T. Padding, Spherical versus elongated particles–Numerical investigation of mixing characteristics in a gas fluidized bed, *Chemical Engineering Science: X* 8 (2020) 100079.

[69] N.P. Pérez, D.T. Pedroso, E.B. Machin, J.S. Antunes, C.E. Tuna, J.L. Silveira, Geometrical characteristics of sugarcane bagasse for being used as fuel in fluidized bed technologies, *Renewable Energy* 143 (2019) 1210-1224.

[70] F.O. Centeno-González, E.E.S. Lora, H.F.V. Nova, L.J.M. Neto, A.M.M. Reyes, A. Ratner, M. Ghamari, CFD modeling of combustion of sugarcane bagasse in an industrial boiler, *Fuel* 193 (2017) 31-38.

[71] F. Oppong, Recent studies of heat transfer mechanisms in a fluidized bed, *J. South Afr. Inst. Mech. Eng.* 34 (2018) 72-82.

[72] Z. Hau, E.W.C. Lim, Heat transfer from an immersed tube in a bubbling fluidized bed, *Industrial & Engineering Chemistry Research* 55(33) (2016) 9040-9053.

[73] Q. Hou, Z. Zhou, A. Yu, Gas–solid flow and heat transfer in fluidized beds with

tubes: Effects of material properties and tube array settings, *Powder Technology* 296 (2016) 59-71.

[74] J. Xue, L. Xie, Y. Shao, W. Zhong, CFD-DEM study of the effects of solid properties and aeration conditions on heat transfer in fluidized bed, *Advanced Powder Technology* 31(9) (2020) 3974-3992.

[75] P.C. Bisognin, J.C.S.C. Bastos, H.F. Meier, N. Padoin, C. Soares, Influence of different parameters on the tube-to-bed heat transfer coefficient in a gas-solid fluidized bed heat exchanger, *Chemical Engineering and Processing-Process Intensification* 147 (2020) 107693.

[76] J.R. Grace, T. Knowlton, A. Avidan, *Circulating fluidized beds*, Springer Science & Business Media 2012.

[77] X. Ku, T. Li, T. Løvås, CFD-DEM simulation of biomass gasification with steam in a fluidized bed reactor, *Chemical Engineering Science* 122 (2015) 270-283.

[78] P. Chaiwang, C. Sakaunnapaporn, T. Sema, P. Piumsomboon, B. Chalermssinsuwan, Statistical experimental design for carbon dioxide capture in circulating fluidized bed using computational fluid dynamics simulation: effect of operating parameters, *Journal of Applied Science and Engineering* 23(2) (2020) 303-317.

[79] C. Soanuch, K. Korkerd, J. Phupanit, R. Piemjaiswang, P. Piumsomboon, B. Chalermssinsuwan, Computational fluid dynamics simulation of methanol to olefins in stage circulating fluidized bed riser: Effect of reactor stage parameters on product yields, *Korean Journal of Chemical Engineering* 38 (2021) 540-551.

[80] S.-H. Chou, Y.-L. Song, S.-S. Hsiau, A study of the mixing index in solid particles, *KONA Powder and Particle Journal* 34 (2017) 275-281.

- [81] H. Wang, Z. Zhong, A mixing behavior study of biomass particles and sands in fluidized bed based on CFD-DEM simulation, *Energies* 12(9) (2019) 1801.
- [82] X. Gao, J. Yu, C. Li, R. Panday, Y. Xu, T. Li, H. Ashfaq, B. Hughes, W.A. Rogers, Comprehensive experimental investigation on biomass-glass beads binary fluidization: A data set for CFD model validation, *AIChE Journal* 66(2) (2020) e16843.
- [83] N.P. Pérez, D.T. Pedroso, E.B. Machin, J.S. Antunes, R.A.V. Ramos, J.L. Silveira, Fluid dynamic study of mixtures of sugarcane bagasse and sand particles: Minimum fluidization velocity, *Biomass and bioenergy* 107 (2017) 135-149.
- [84] C. Soanuch, K. Korkerd, P. Piumsomboon, B. Chalermssinsuwan, Minimum fluidization velocities of binary and ternary biomass mixtures with silica sand, *Energy Reports* 6 (2020) 67-72.
- [85] B. Cluet, G. Mauviel, Y. Rogeau, O. Authier, A. Delebarre, Segregation of wood particles in a bubbling fluidized bed, *Fuel processing technology* 133 (2015) 80-88.
- [86] F. Fotovat, R. Ansart, M. Hemati, O. Simonin, J. Chaouki, Sand-assisted fluidization of large cylindrical and spherical biomass particles: Experiments and simulation, *Chemical Engineering Science* 126 (2015) 543-559.
- [87] A. Di Renzo, F.P. Di Maio, R. Girimonte, V. Vivacqua, Segregation direction reversal of gas-fluidized biomass/inert mixtures—Experiments based on Particle Segregation Model predictions, *Chemical Engineering Journal* 262 (2015) 727-736.
- [88] Y. Zhang, B. Jin, W. Zhong, B. Ren, R. Xiao, Characterization of fluidization and segregation of biomass particles by combining image processing and pressure fluctuations analysis, *International Journal of Chemical Reactor Engineering* 7(1) (2009).

- [89] K. Korkerd, C. Soanuch, Z. Zhou, P. Piumsomboon, B. Chalernsinsuwan, Effect of particle size and particle loading on the mixing behavior of rod-like particles and spherical particles in a fluidized bed, *Energy Reports* 8 (2022) 1-7.
- [90] D.A. Clarke, A.J. Sederman, L.F. Gladden, D.J. Holland, Investigation of void fraction schemes for use with CFD-DEM simulations of fluidized beds, *Industrial & Engineering Chemistry Research* 57(8) (2018) 3002-3013.
- [91] D. Kong, K. Luo, S. Wang, J. Yu, J. Fan, Particle behaviours of biomass gasification in a bubbling fluidized bed, *Chemical Engineering Journal* 428 (2022) 131847.
- [92] Z. Zhang, L. Liu, Y. Yuan, A. Yu, A simulation study of the effects of dynamic variables on the packing of spheres, *Powder technology* 116(1) (2001) 23-32.
- [93] S.A. El-Sayed, M.E. Mostafa, Combustion and emission characteristics of Egyptian sugarcane bagasse and cotton stalks powders in a bubbling fluidized bed combustor, *Waste and Biomass Valorization* 10 (2019) 2015-2035.
- [94] K. Korkerd, C. Soanuch, Z. Zhou, P. Piumsomboon, B. Chalernsinsuwan, Correlation for predicting minimum fluidization velocity with different size distributions and bed inventories at elevated temperature in gas-solid fluidized bed, *Advanced Powder Technology* 33(3) (2022) 103483.
- [95] L. Nunes, J. Matias, J. Catalão, Mixed biomass pellets for thermal energy production: A review of combustion models, *Applied Energy* 127 (2014) 135-140.
- [96] Y. Xia, F. Chen, J.L. Klinger, J.J. Kane, T. Bhattacharjee, R. Seifert, O.O. Ajayi, Q. Chen, Assessment of a tomography-informed polyhedral discrete element modelling approach for complex-shaped granular woody biomass in stress consolidation,

Biosystems Engineering 205 (2021) 187-211.

[97] N.E. Benti, G.S. Gurmesa, T. Argaw, A.B. Aneseyee, S. Gunta, G.B. Kassahun, G.S. Aga, A.A. Asfaw, The current status, challenges and prospects of using biomass energy in Ethiopia, *Biotechnology for Biofuels* 14(1) (2021) 1-24.

[98] M. Stasiak, M. Molenda, M. Bańda, E. Gondek, Mechanical properties of sawdust and woodchips, *Fuel* 159 (2015) 900-908.

[99] F.L. Brandao, G.L. Verissimo, M.A. Leite, A.J. Leiroz, M.E. Cruz, Computational study of sugarcane bagasse pyrolysis modeling in a bubbling fluidized bed reactor, *Energy & Fuels* 32(2) (2018) 1711-1723.

[100] G. Lian, W. Zhong, X. Liu, CFD–DEM investigation of fuel dispersion behaviors in a 3D fluidized bed, *Industrial & Engineering Chemistry Research* 60(36) (2021) 13272-13285.

[101] J. Xie, W. Zhong, Y. Shao, Study on the char combustion in a fluidized bed by CFD-DEM simulations: Influences of fuel properties, *Powder Technology* 394 (2021) 20-34.

[102] P. Bhalode, M. Ierapetritou, A review of existing mixing indices in solid-based continuous blending operations, *Powder technology* 373 (2020) 195-209.

[103] P.M.C. Lacey, Developments in the theory of particle mixing, *Journal of applied chemistry* 4(5) (1954) 257-268.

[104] Y. Wen, M. Liu, B. Liu, Y. Shao, Comparative study on the characterization method of particle mixing index using DEM method, *Procedia engineering* 102 (2015) 1630-1642.

[105] Y. Zhang, B. Jin, W. Zhong, Experimental investigation on mixing and segregation

- behavior of biomass particle in fluidized bed, *Chemical Engineering and Processing: Process Intensification* 48(3) (2009) 745-754.
- [106] X. Wang, S.R. Kersten, W. Prins, W.P. van Swaaij, Biomass pyrolysis in a fluidized bed reactor. Part 2: Experimental validation of model results, *Industrial & engineering chemistry research* 44(23) (2005) 8786-8795.
- [107] E. Biagini, P. Narducci, L. Tognotti, Size and structural characterization of lignin-cellulosic fuels after the rapid devolatilization, *Fuel* 87(2) (2008) 177-186.
- [108] J. Lin, K. Luo, S. Wang, L. Sun, J. Fan, Particle-scale simulation of solid mixing characteristics of binary particles in a bubbling fluidized bed, *Energies* 13(17) (2020) 4442.
- [109] C.E. Agu, L.-A. Tokheim, C. Pfeifer, B.M. Moldestad, Behaviour of biomass particles in a bubbling fluidized bed: A comparison between wood pellets and wood chips, *Chemical Engineering Journal* 363 (2019) 84-98.
- [110] H. Zhang, W. Qiao, X. An, X. Ye, J. Chen, CFD-DEM study on fluidization characteristics of gas-solid fluidized bed reactor containing ternary mixture, *Powder Technology* 401 (2022) 117354.
- [111] J. Ngoh, E.W.C. Lim, Effects of particle size and bubbling behavior on heat transfer in gas fluidized beds, *Applied Thermal Engineering* 105 (2016) 225-242.
- [112] J. Gan, Z. Zhou, A. Yu, Particle scale study of heat transfer in packed and fluidized beds of ellipsoidal particles, *Chemical engineering science* 144 (2016) 201-215.
- [113] S. Du, J. Wang, Y. Yu, Q. Zhou, Coarse-grained CFD-DEM simulation of coal and biomass co-gasification process in a fluidized bed reactor: Effects of particle size

- distribution and operating pressure, *Renewable Energy* 202 (2023) 483-498.
- [114] Z. Zhou, D. Pinson, R. Zou, A. Yu, Discrete particle simulation of gas fluidization of ellipsoidal particles, *Chemical Engineering Science* 66(23) (2011) 6128-6145.
- [115] H. Taofeeq, M. Al-Dahhan, M.R. Engineering, A. Laboratory, Investigation of the effect of vertical immersed tube diameter on heat transfer in a gas-solid fluidized bed, *International Journal of Thermal Sciences* 135 (2019) 546-558.
- [116] Z. Bao, L. Duan, K. Wu, C. Zhao, An investigation on the heat transfer model for immersed horizontal tube bundles in a pressurized fluidized bed, *Applied Thermal Engineering* 170 (2020) 115035.
- [117] T. Yurata, P. Piumsomboon, B. Chalermssinsuwan, Effect of contact force modeling parameters on the system hydrodynamics of spouted bed using CFD-DEM simulation and 2k factorial experimental design, *Chemical Engineering Research and Design* 153 (2020) 401-418.
- [118] R. Piemjaiswang, J. Charoenchaipet, T. Saelau, P. Piumsomboon, B. Chalermssinsuwan, Effect of design parameters on system mixing for a micro fluidized bed reactor using computational fluid dynamics simulation, *Brazilian Journal of Chemical Engineering* 38 (2021) 21-31.
- [119] M. Zhao, D. Liu, J. Ma, X. Chen, CFD-DEM simulation of gas-solid flow of wet particles in a fluidized bed with immersed tubes, *Chemical Engineering and Processing-Process Intensification* 156 (2020) 108098.
- [120] S.I. Ngo, Y.-I. Lim, D. Lee, M.W. Seo, Flow behavior and heat transfer in bubbling fluidized-bed with immersed heat exchange tubes for CO₂ methanation, *Powder Technology* 380 (2021) 462-474.

- [121] S. Yang, K. Luo, J. Fan, K. Cen, Particle-scale investigation of the hydrodynamics and tube erosion property in a three-dimensional (3-D) bubbling fluidized bed with immersed tubes, *Industrial & Engineering Chemistry Research* 53(17) (2014) 6896-6912.
- [122] T. Li, J.-F. Dietiker, Y. Zhang, M. Shahnam, Cartesian grid simulations of bubbling fluidized beds with a horizontal tube bundle, *Chemical Engineering Science* 66(23) (2011) 6220-6231.
- [123] A. Costa, F. Colman, P. Paraiso, L. Jorge, CFD modelling of fluidized bed with immersed tubes, *Advances in Chemical Engineering* 10 (2012) 31671.
- [124] J. Joshi, Solid-liquid fluidised beds: some design aspects, *Chemical Engineering Research and Design* 61 (1983) 143-161.
- [125] L. Auret, C. Aldrich, Interpretation of nonlinear relationships between process variables by use of random forests, *Minerals Engineering* 35 (2012) 27-42.
- [126] L. Kamble, D. Pangavhane, T. Singh, Artificial neural network based prediction of heat transfer from horizontal tube bundles immersed in gas–solid fluidized bed of large particles, *Journal of Heat Transfer* 137(1) (2015).
- [127] S. Kumar Bashapaka, V. Vinod Ananthula, Experimental and modeling studies on mixing behavior of binary mixtures in a spout-fluid bed, *Particulate Science and Technology* 37(4) (2019) 391-402.
- [128] J.W. Chew, R.A. Cocco, Application of machine learning methods to understand and predict circulating fluidized bed riser flow characteristics, *Chemical Engineering Science* 217 (2020) 115503.
- [129] Y. Fu, S. Wang, X. Xu, Y. Zhao, L. Dong, Z. Chen, Particle flow characteristics in

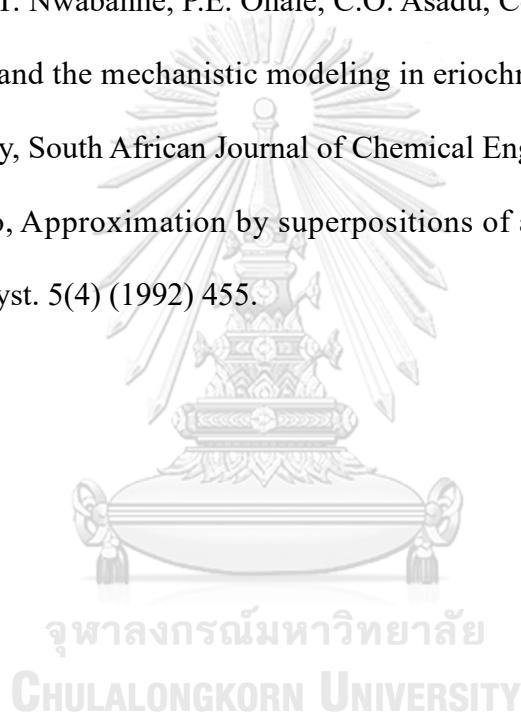
- a gas-solid separation fluidized bed based on machine learning, *Fuel* 314 (2022) 123039.
- [130] Z. Xie, X. Gu, Y. Shen, A machine learning study of predicting mixing and segregation behaviors in a bidisperse solid–liquid fluidized bed, *Industrial & Engineering Chemistry Research* 61(24) (2022) 8551-8565.
- [131] M. Upadhyay, V.M. Nagulapati, H. Lim, Hybrid CFD-neural networks technique to predict circulating fluidized bed reactor riser hydrodynamics, *Journal of Cleaner Production* 337 (2022) 130490.
- [132] Y. Cui, W. Zhong, Z. Zhou, A. Yu, X. Liu, J. Xiang, Coupled simulation and deep-learning prediction of combustion and heat transfer processes in supercritical CO₂ CFB boiler, *Advanced Powder Technology* 33(1) (2022) 103361.
- [133] A. Dean, D. Voss, D. Draguljić, A. Dean, D. Voss, D. Draguljić, Response surface methodology, *Design and analysis of experiments* (2017) 565-614.
- [134] M. Puig-Arnabat, J.A. Hernández, J.C. Bruno, A. Coronas, Artificial neural network models for biomass gasification in fluidized bed gasifiers, *Biomass and bioenergy* 49 (2013) 279-289.
- [135] M. Ariana, B. Vaferi, G. Karimi, Prediction of thermal conductivity of alumina water-based nanofluids by artificial neural networks, *Powder Technology* 278 (2015) 1-10.
- [136] D.W. Marquardt, An algorithm for least-squares estimation of nonlinear parameters, *Journal of the society for Industrial and Applied Mathematics* 11(2) (1963) 431-441.
- [137] B. Vaferi, M. Karimi, M. Azizi, H. Esmaeili, Comparison between the artificial

neural network, SAFT and PRSV approach in obtaining the solubility of solid aromatic compounds in supercritical carbon dioxide, *The Journal of Supercritical Fluids* 77 (2013) 44-51.

[138] H. Sabzian, E. Kamrani, S.M.S. Hashemi, A Neural Network Model for Determining the Success or Failure of High-tech Projects Development: A Case of Pharmaceutical industry, arXiv preprint arXiv:1809.00927 (2018).

[139] C.E. Onu, J.T. Nwabanne, P.E. Ohale, C.O. Asadu, Comparative analysis of RSM, ANN and ANFIS and the mechanistic modeling in eriochrome black-T dye adsorption using modified clay, *South African Journal of Chemical Engineering* 36 (2021) 24-42.

[140] G. Cybenko, Approximation by superpositions of a sigmoidal function, *Math. Control. Signals Syst.* 5(4) (1992) 455.





จุฬาลงกรณ์มหาวิทยาลัย
CHULALONGKORN UNIVERSITY

VITA

NAME	Krittin Korkerd
DATE OF BIRTH	28 July 1995
PLACE OF BIRTH	Bangkok, Thailand
INSTITUTIONS ATTENDED	M.Sc., Chemical Technology, Chulalongkorn University, Thailand B.Sc., Chemical Engineering (2nd Class Honors), Chulalongkorn University, Thailand
HOME ADDRESS	109/6, Sai Mai 16 Alley, Sai Mai Road, Sai Mai District, Bangkok, 10220
PUBLICATION	<ol style="list-style-type: none">1) Korkerd, K., Soanuch, C., Zongyan, Z., Piumsomboon, P., and Chalermssinsuwan, B. Effect of particle size and particle loading on the mixing behavior of rod-like particles and spherical particles in a fluidized bed. <i>Energy Reports</i> 8(9) (2022), 1-7.2) Soanuch, C., Korkerd, K., Pareek, V., Piumsomboon, P., and Chalermssinsuwan, B. Fast pyrolysis downer reactor: Effect of reactor geometry on the hydrodynamics. <i>Industrial & Engineering Chemistry Research</i> 61(11) (2022), 4153-4167.3) Korkerd, K., Soanuch, C., Zongyan, Z., Piumsomboon, P., and Chalermssinsuwan, B. Correlation for predicting minimum fluidization velocity with different size distributions and bed inventories at elevated temperature in gas-solid fluidized bed. <i>Advanced Powder Technology</i> 33(3) (2022), 103483.4) Khunphakdee, P., Korkerd, K., Soanuch, C., and Chalermssinsuwan, B. Data-driven correlations of higher heating value for biomass, waste and their combination based on their elemental compositions. <i>Energy Reports</i> 8(5) (2022), 36-42.5) Korkerd, K., Soanuch, C., Gidaspow, D., Piumsomboon, P., and Chalermssinsuwan, B. Artificial neural network model for predicting minimum fluidization velocity and maximum pressure drop of gas fluidized bed with different particle size distributions. <i>South African Journal of Chemical Engineering</i> 37 (2021) 61-73.6) Soanuch, C., Korkerd, K., Phupanit, J., Piemjaiswang, R., Piumsomboon, P., and Chalermssinsuwan, B. Computational fluid dynamics simulation of methanol to olefins in stage circulating fluidized bed riser: Effect of reactor stage parameters on product yields. <i>Korean Journal of Chemical Engineering</i> 38 (2021) 540-551.7) Soanuch, C., Korkerd, K., Piumsomboon, P., and Chalermssinsuwan, B. Minimum fluidization velocities of binary and ternary biomass mixtures with silica sand. <i>Energy Reports</i> 6(6) (2020), 67-72.8) Korkerd, K., Soanuch, C., Piumsomboon, P., and Chalermssinsuwan, B. Effect of particle size distributions on

minimum fluidization velocity with varying gas temperature. *International Journal of Environmental Science and Development* 11(11) (2020), 524-529.

9) Phupanit, J., Soanuch, C., Korkerd, K., Piumsomboon, P., and Chalermssinsuwan, B. Computational fluid dynamics simulation of system hydrodynamics in a riser of stage circulating fluidized bed reactor. *Asia-Pacific Journal of Chemical Engineering* 14(1) (2019), e2277.



จุฬาลงกรณ์มหาวิทยาลัย
CHULALONGKORN UNIVERSITY